Università degli Studi di Palermo

AREA RICERCA E INNOVAZIONE
SETTORE DOTTORATI E CONTRATTI PER LA RICERCA
U. O. DOTTORATI DI RICERCA

Mechanical, Manufacturing, Management and Aerospace Innovation
Dipartimento di Ingegneria
Settore Scientifico Disciplinare IMIS-01/A

NON-INVASIVE ASSESSMENT OF VASCULAR HEALTH USING PHOTOPLETHYSMOGRAPHIC SENSORS:
From In Vitro Arterial Stiffness to In Vivo Vascular Aging Characterization

IL DOTTORE
GIANLUCA DIANA

IL COORDINATORE
PROF.SSA GIADA LA SCALIA

IL TUTOR
PROF. FRANCESCO SCARDULLA

IL CO-TUTOR
PROF. LEONARDO D'ACQUISTO

CICLO XXXVIII
ANNO CONSEGUIMENTO TITOLO 2026

Abstract

Photoplethysmography (PPG) is a low-cost and non-invasive optical technique, already widely integrated into consumer wearable devices, that measures blood volume changes in the microvascular bed. Although its clinical potential extends well beyond heart rate and oxygen saturation monitoring, the morphological richness of the PPG signal remains largely underexploited. Arterial stiffness and vascular aging are among the earliest and most significant markers of cardiovascular risk, yet their assessment still relies on specialised clinical techniques unsuitable for continuous, large-scale screening. In this context, PPG offers a promising platform to bring vascular diagnostics closer to everyday health monitoring.

This thesis develops an integrated experimental framework for the non-invasive assessment of vascular health using PPG sensors, following a coherent progression from controlled in vitro conditions to clinically heterogeneous populations. The work is articulated in four interconnected studies. First, PPG sensors were employed to estimate arterial wall stiffness through pulse transit time and pulse wave velocity measurements on silicone phantom models, representing different physiological vascular conditions, within a mock circulatory loop. Second, the second derivative of the PPG signal, known as the acceleration plethysmogram (APG), was investigated as a route to vascular aging assessment: a dual in vitro–in vivo design revealed strong correlations between APG-derived morphological indices and both wall stiffness and chronological age, supporting their role as non-invasive surrogates of vascular health. Third, the APG analysis was systematically extended to multiple wavelengths and anatomical sites through a custom-built wearable prototype, identifying the optimal optical configuration and demonstrating compatibility with the dominant smart and wearable devices. Fourth, the discriminative power of APG-derived indices was evaluated on a clinically heterogeneous cohort including both healthy and pathological subjects, demonstrating that these indices capture a vascular aging component that is clinically informative beyond chronological age and can effectively distinguish between healthy and diseased vascular states.

Overall, this thesis establishes a unified methodological framework that progresses from physical interpretability to clinical utility, combining in vitro mechanical validation, morphological signal analysis, multi-wavelength optimisation and clinical-group discrimination. The proposed approach lays the groundwork for the integration of PPG-based vascular biomarkers into wearable devices, supporting the transition towards continuous, accessible and large-scale non-invasive cardiovascular monitoring.

Acknowledgments

I would first like to thank my supervisor, Professor Francesco Scardulla, for his constant guidance and support throughout this doctoral journey. His availability, his expertise, and his ability to steer my work with clarity and encouragement have been fundamental to my growth during these years.

My sincere gratitude goes also to my co-tutor, Prof. Leonardo D'Acquisto, for his invaluable mentorship and for the wisdom with which he has accompanied this work, sharing insights that only experience can provide.

I am grateful to all the doctoral colleagues and thesis students with whom I had the pleasure of exchanging ideas and working side by side during these years.

A special acknowledgement goes to the Biomedical and Mobile Health Technology Lab at the Balgrist Campus of ETH Zürich, where I had the privilege of spending one of the most formative and enriching experiences of my life, both professionally and personally.

I thank my parents for their unconditional support and for always believing in me.

Finally, a heartfelt thank you to my girlfriend, Alessandra, for her patience, her strength, and for standing by my side every step of the way.

Table of Contents

List of Figures

List of Tables

Nomenclature

AC	Alternating Current
ADC	Analog-to-Digital Converter
AGI	Aging Index
ANOVA	Analysis of Variance
APG	Acceleration Plethysmogram
AUC	Area Under the Curve
BMI	Body Mass Index
CAVI	Cardio-Ankle Vascular Index
cfPWV	Carotid–Femoral Pulse Wave Velocity
CVD	Cardiovascular Disease
DBP	Diastolic Blood Pressure
DC	Direct Current
E	Young's Modulus
FIR	Finite Impulse Response
HR	Heart Rate
IIR	Infinite Impulse Response
IR	Infrared
JPG	Jerk Plethysmogram
LED	Light-Emitting Diode
MAE	Mean Absolute Error
NTC	Negative Temperature Coefficient (thermistor)
PPG	Photoplethysmography / Photoplethysmogram
PTT	Pulse Transit Time
PWV	Pulse Wave Velocity
SBP	Systolic Blood Pressure
SD	Standard Deviation
SI	Stiffness Index
SNR	Signal-to-Noise Ratio
SpO_2	Peripheral Arterial Oxygen Saturation
SSQI	Skewness Signal Quality Index
THV	Transcatheter Heart Valve
VPG	Velocity Plethysmogram

Chapter 1 — Introduction

1.1 Context and Research Motivation

Cardiovascular diseases (CVDs) remain the leading cause of death worldwide. According to the World Health Organization, approximately 17.9 million deaths per year are attributable to CVDs, accounting for nearly one third of global mortality, and the burden affects both developed and developing countries with comparable severity. Beyond the toll on individual lives, the rising prevalence of cardiovascular and metabolic disorders has translated into one of the largest sources of healthcare expenditure in industrialised countries, and into a growing pressure on national health systems, which must respond to rising demand from progressively ageing populations.

Within this clinical landscape, the structural and functional remodelling of the arterial tree, conventionally referred to as vascular aging, plays a central role. Cardiovascular and cardiometabolic diseases, such as hypertension, atherosclerosis, type-2 diabetes mellitus and chronic kidney disease, despite their distinct aetiologies, converge on a common vascular alteration, namely the progressive stiffening of the arterial wall, the loss of compliance of the central elastic arteries and the alteration of the propagation properties of the pressure pulse. These mechanical changes are not only a consequence of established disease, but also one of its most informative early markers, since they precede the onset of overt clinical events by several years and, when properly characterised, constitute a quantitative target for primary prevention and risk stratification.

Conventional clinical techniques for arterial-stiffness assessment, such as carotid–femoral pulse wave velocity, have established themselves as reliable and prognostically informative biomarkers of cardiovascular risk. They are, however, intrinsically limited by their reliance on dedicated equipment, by the need for trained operators, by the discrete nature of the measurement and by their incompatibility with continuous, out-of-hospital monitoring. For these reasons, research has increasingly focused on the development of continuous, non-invasive and scalable monitoring solutions that can extend vascular health assessment beyond the clinical setting.

Photoplethysmography (PPG) provides a particularly promising answer to this need. As a non-invasive optical technique that probes the pulsatile blood-volume changes of the microvascular bed, PPG combines several features that match the requirements of large-scale vascular monitoring: its sensors are small, low-cost and easily integrable into contact

and wearable devices, and its signal carries both timing and morphological information that mirrors the underlying haemodynamic phenomena. The widespread availability of PPG sensors in consumer wearable devices is, in itself, a methodological resource of unprecedented scale: any analytical pipeline that can be implemented on the optical signals already acquired by these devices does not require the design or distribution of new hardware, and can therefore reach a population of users that no conventional clinical platform can match.

Building on this premise, the doctoral project presented in this thesis explored the use of photoplethysmography for the non-invasive assessment of vascular health. The research progressed from in vitro experimental investigations, aimed at demonstrating the potential of PPG sensors for arterial stiffness estimation under controlled conditions, to in vivo studies focused on the extraction and validation of morphological indices of vascular aging derived from the second derivative of the PPG signal, known as the acceleration plethysmogram (APG). Together, these two approaches provide a comprehensive view of the technique's potential, from the physical characterisation of arterial mechanics to the extraction of clinically informative digital biomarkers. The underlying translational ambition of the work is not to compete with the gold-standard reference techniques on their own terrain, but to extend the reach of vascular monitoring to the continuous, low-cost and ambulatory regime in which most preclinical alterations develop, and in which preventive action would have its highest impact.

1.2 Aim and Objectives of the Thesis

The general aim of this thesis is to develop, validate and translate a coherent methodological framework for the non-invasive assessment of vascular health based on PPG signals, by combining controlled in vitro experiments, custom-designed wearable prototypes and clinical investigations on heterogeneous human cohorts. Within this general aim, the doctoral work pursued four specific objectives, each addressed in a dedicated experimental chapter.

The first objective, addressed in Chapter 4, was to develop and validate, in a controlled in vitro setup, a method for estimating the Young's modulus of vessel-like phantom models using a pair of PPG sensors, by exploiting the relationship between pulse wave velocity and wall mechanical properties. This objective also reports a complementary application of the same methodology to the non-invasive monitoring of transcatheter heart valves.

The second objective, addressed in Chapter 5, was to investigate the acceleration plethysmogram as a route to the assessment of vascular aging, by quantifying the relationship between APG-derived morphological indices and the underlying mechanical and physiological vascular condition through a dual in vitro–in vivo experimental design.

The third objective was to identify the optimal optical configuration for APG-based vascular aging assessment in wearable devices, by systematically comparing four wavelengths and two anatomical measurement sites on a custom-built multi-wavelength PPG prototype. This objective is addressed in Chapter 6, which describes both the hardware development of the prototype and its experimental validation on a cohort of healthy volunteers.

The fourth objective was to evaluate the discriminative power of APG-derived indices in a clinically heterogeneous population, in order to assess whether these indices can serve as digital biomarkers of cardiometabolic health. This objective is addressed in Chapter 7 through a cross-sectional analysis of subjects stratified into healthy, hypertensive and diabetic groups.

From a metrological standpoint, these four objectives represent a progression through three levels of access to vascular stiffness, each progressively more indirect. The first level is the direct estimation of Young's modulus in vitro (Chapter 4), in which a mechanical quantity is derived from measured quantities using an explicit physical model. The second level consists of surrogate indices derived from the morphology of the APG (Chapters 5 and 6), which do not directly measure any mechanical quantity but track its evolution through dimensionless waveform descriptors. The third level consists of clinical digital biomarkers (Chapter 7), evaluated not against a mechanical reference but based on their ability to distinguish between clinical conditions. This distinction—from direct physical measurement to indirect clinical relevance—structures the entire thesis and defines its methodological coherence.

1.3 Thesis Outline

Chapter 2 — Theoretical and Technological Foundations introduces the cardiovascular system, the mechanical properties of the arterial wall, the concept of vascular aging and the photoplethysmographic technique, including the principles of light–tissue interaction, the morphological structure of the PPG waveform and the analytical role of its successive derivatives.

Chapter 3 — State of the Art reviews the non-invasive methods currently available for arterial-stiffness assessment, with a dedicated focus on PPG-based approaches and on the second derivative of the PPG signal as a surrogate of vascular aging, and provides a concise overview of other vascular and cardiovascular applications of PPG that are relevant to the present work.

Chapter 4 — In Vitro Study: Arterial Stiffness Estimation Using PPG Sensors presents the experimental campaign on silicone phantom models with different mechanical properties and inter-sensor configurations, the validation against uniaxial tensile testing, and the application extension of the same architecture to the non-invasive monitoring of transcatheter heart valves.

Chapter 5 — Analysis of the APG Signal as an Indicator of Vascular Aging introduces the second methodological line of the thesis, focused on the morphological indices of the second derivative of the PPG signal, and consolidates their physiological interpretation through a combined in vitro and in vivo experimental design.

Chapter 6 — Multi-Wavelength PPG Comparison for Vascular Aging Assessment extends the APG analysis to four wavelengths and two anatomical sites through a custom-built wearable prototype and identifies the optimal optical configuration for APG-based vascular aging assessment in wearable devices.

Chapter 7 — APG Indices as Digital Biomarkers of Cardiometabolic Health evaluates the discriminative power of the conventional APG indices on a clinically heterogeneous cohort of healthy, hypertensive and diabetic subjects, through a complementary statistical framework based on hypothesis testing, effect-size analysis and distribution-overlap metrics.

Chapter 8 — Conclusions and Future Developments summarises the key findings of the doctoral project, articulates its overall scientific contribution, and discusses possible directions for future research at the intersection of optical sensing, vascular biomechanics and clinical translation.

Chapter 2 — Theoretical and Technological Foundations

This chapter provides the theoretical background and the technological foundations underlying the research presented in this thesis. The first part introduces the cardiovascular system and the concept of arterial stiffness, including the key equations that will be used in subsequent chapters. The following sections will cover the photoplethysmographic technique, the derivatives of the PPG signal, and the main factors influencing signal quality.

2.1 The Cardiovascular System

2.1.1 Fundamentals of Anatomy and Physiology

The cardiovascular system is responsible for the transport of blood throughout the body, ensuring the delivery of oxygen and nutrients to tissues and the removal of metabolic waste products. It consists of three principal components: the heart, which serves as the central pump; the blood vessels, which form an extensive network of conduits; and the blood itself, the fluid medium carrying dissolved gases, nutrients, hormones, and cells [1].

The heart is a muscular organ divided into four chambers: two atria (right and left) and two ventricles (right and left). The right side of the heart receives deoxygenated blood from the systemic circulation through the venae cavae and pumps it to the lungs via the pulmonary arteries, where gas exchange takes place. The left side receives oxygenated blood from the pulmonary veins and ejects it into the systemic circulation through the aorta. The coordinated contraction and relaxation of the cardiac chambers give rise to the cardiac cycle, which consists of two main phases: systole (contraction) and diastole (relaxation). During systole, the left ventricle ejects blood into the aorta, generating a pressure wave that propagates along the arterial tree. This pressure wave, commonly referred to as the arterial pulse, travels from the central arteries towards the peripheral vasculature at a velocity that depends on the mechanical properties of the vessel walls. The resulting pressure waveform exhibits a characteristic morphology: a rapid systolic upstroke corresponding to ventricular ejection, followed by a descending phase during which the aortic valve closes, producing a small deflection known as the dicrotic notch, and a subsequent diastolic decline [2].

Under normal resting conditions in a healthy adult, the heart beats at approximately 60–100 beats per minute, producing a cardiac output of approximately 5 L/min. Systemic

arterial pressure typically ranges between 120 mmHg (systolic) and 80 mmHg (diastolic). These haemodynamic parameters are regulated by a complex interplay of neural, hormonal, and local mechanisms that adjust heart rate, stroke volume, and peripheral vascular resistance to meet the metabolic demands of the body [3].

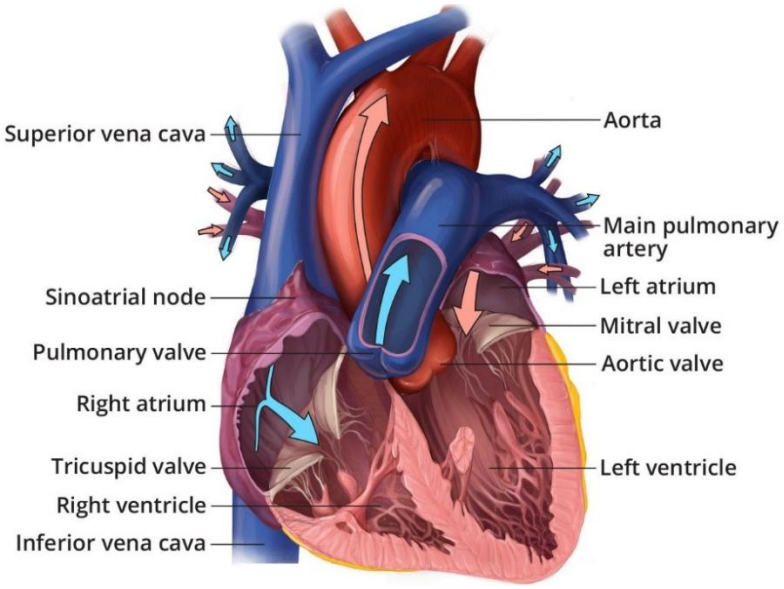

Figure 2.1 *Cross-sectional diagram of the heart showing its four chambers, cardiac valves, the sinoatrial node, and major connected vessels [4].*

2.1.2 Blood Vessel Structure and Mechanical Properties

Blood vessels are not rigid conduits but rather dynamic structures whose mechanical behaviour plays a critical role in cardiovascular function. The arterial wall is composed of three concentric layers, or tunics, each with distinct structural and functional characteristics [5].

The tunica intima is the innermost layer, in direct contact with the blood. It consists of a single layer of endothelial cells supported by a thin layer of connective tissue and an internal elastic lamina. The endothelium plays a key role in regulating vascular tone, coagulation, and inflammatory responses. The tunica media is the intermediate and thickest layer in arteries, primarily composed of smooth muscle cells arranged concentrically, interspersed with elastic fibres (elastin) and collagen. This layer is the main determinant of the mechanical properties of the vessel, including its ability to distend under pressure and recoil during diastole. The tunica adventitia is the outermost layer, composed mainly of collagen fibres and connective tissue, which anchors the vessel to the surrounding structures and provides structural support [6].

The relative proportion of elastin and collagen within the tunica media determines the mechanical behaviour of the vessel. Elastic arteries, such as the aorta and its major branches, contain a high proportion of elastin, which enables them to expand during systole and recoil during diastole, thereby damping the pulsatile flow generated by the heart into a more continuous peripheral flow. This property is known as the Windkessel effect. Muscular arteries, located more distally, have a higher proportion of smooth muscle relative to elastin, which allows them to regulate local blood flow through vasoconstriction and vasodilation [7].

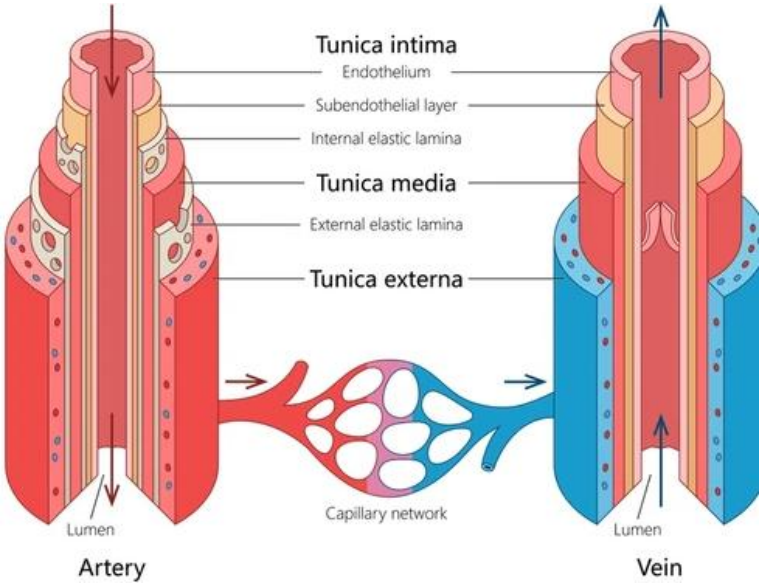

Figure 2.2 *Anatomical diagram showing structural differences between arteries, veins, tunica layers and blood flow direction through vessels.*

The mechanical properties of blood vessels are commonly described in terms of Young's modulus (E), which quantifies the intrinsic stiffness of the wall material. In healthy conditions, the aorta exhibits Young's modulus values in the range of 0.2–2 MPa, while peripheral arteries and veins show values between 0.6 and 3.5 MPa [8]. In pathological conditions, such as atherosclerosis, an increase in the elastic modulus of up to 60% can be observed, reflecting the structural remodelling of the arterial wall [9,10].

With advancing age, significant changes occur in the composition of the arterial wall. The elastin content progressively decreases, while collagen deposition increases, leading to a gradual stiffening of the vessel. Additionally, fragmentation of elastic lamellae and cross-linking of collagen fibres by advanced glycation end-products further contribute to the loss of arterial compliance [11]. These structural alterations are not uniform throughout the arterial tree: they are more pronounced in central elastic arteries (aorta and carotid) than in peripheral muscular arteries [12,13].

2.1.3 Arterial Stiffness and Vascular Aging

Arterial stiffness is defined as the reduced ability of an artery to expand and recoil in response to pressure changes during the cardiac cycle. It represents one of the earliest detectable manifestations of adverse structural and functional changes in the vessel wall and has been recognised as an independent predictor of cardiovascular morbidity and mortality [14,15]. Indeed, increased arterial stiffness is associated with hypertension, atherosclerosis, stroke, and myocardial infarction, independently of traditional cardiovascular risk factors such as age, cholesterol levels, and smoking status [16,17].

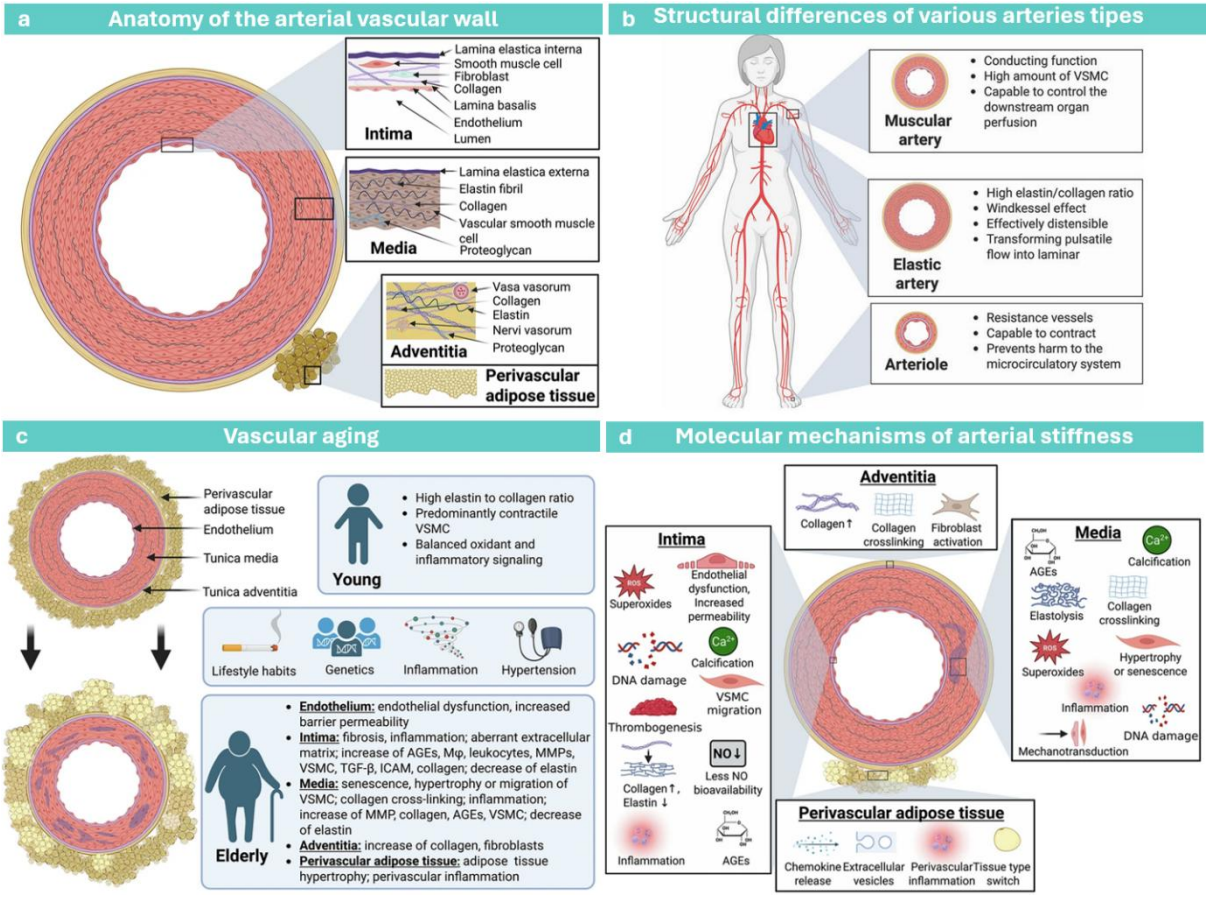

Figure 2.3 a *Anatomical structure of the vascular wall.* ***b*** *Structural and functional differences in muscular arteries, elastic arteries, and arterioles.* ***c*** *Age affects arterial structure.* ***d*** *Overview of the underlying cellular mechanisms of arterial stiffness in the different layers [14].*

From a haemodynamic perspective, the arterial stiffness has several significant consequences. First, it increases pulse wave velocity (PWV), causing the reflected pressure waves to return to the heart at an earlier stage of the cardiac cycle, increasing central systolic pressure and left ventricular afterload. Second, it reduces the Windkessel buffering capacity of the aorta, resulting in elevated pulse pressure and greater pulsatile stress on the microcirculation of target organs, such as the kidneys [18,19].

The concept of vascular aging refers to the progressive deterioration of arterial structure and function that occurs over time, often described by distinguishing between chronological age and vascular age. Vascular age reflects the actual condition of the arterial system, which may differ considerably from chronological age depending on genetic predisposition, lifestyle factors, and the presence of comorbidities such as diabetes mellitus and chronic kidney disease [20,21]. An individual may have arteries that are biologically older or younger than their chronological age, and this discrepancy has been shown to have prognostic significance [22].

The clinical gold standard for the non-invasive assessment of arterial stiffness is the measurement of PWV, defined as the speed at which the pressure pulse generated by the heart travels along the arterial tree [23,24]. PWV is typically measured over the carotid–femoral segment (cfPWV), a method considered the gold standard according to international guidelines [25–27]. PWV is calculated using space–time measurements, as the ratio between the distance Δs covered by the pulse wave and the pulse transit time (PTT), which is the time delay Δt of the pressure wave between two recording sites [28]:

$$PWV = \frac{\Delta s}{\Delta t} \tag{2.1}$$

The relationship between PWV and the mechanical and geometrical properties of the blood vessel is described by the Moens–Korteweg equation, formulated in 1878 and still widely accepted by the scientific community [29,30]:

$$PWV = \sqrt{\frac{E\,h}{2\,r\,\rho}} \tag{2.2}$$

where E is the circumferential Young's modulus of the vessel wall, h is the wall thickness, r is the internal radius, and ρ is the density of the fluid (blood). This equation establishes a direct link between the propagation velocity of the pressure wave and the elastic properties of the arterial wall: a stiffer vessel (higher E) results in a higher PWV. On the contrary, a more compliant vessel transmits the pulse wave more slowly [31]. It is important to note that the Moens–Korteweg equation is derived under several simplifying assumptions: (i) a thin-walled vessel ($h \ll r$); (ii) a homogeneous, isotropic, and linearly elastic wall material; (iii) an incompressible, non-viscous fluid; (iv) an infinitely long, straight, cylindrical tube with no branching or tapering; (v) no wave reflections; and (vi) small-amplitude wave perturbations [32,33]. In real arteries, many

of these assumptions are violated: arterial walls are anisotropic, viscoelastic, exhibit non-linearly behaviour and are tethered to surrounding tissue. The arterial tree includes bifurcations and progressive tapering that generate wave reflections and impedance mismatches [34]. Despite these limitations, the Moens–Korteweg equation remains widely used in clinical practice and research due to its simplicity and the strong proportional relationship it establishes between PWV and wall stiffness.

A complementary and more general formulation is provided by the Bramwell–Hill equation [35], derived in 1922 from the water-hammer equation and expressed as:

$$PWV = \sqrt{\frac{A\,\Delta P}{\rho\,\Delta A}} = \sqrt{\frac{1}{\rho\,D}} \tag{2.3}$$

where A is the mean area of the blood vessel, ΔP is the difference between the central systolic and diastolic pressures, ΔA is the difference between the maximum and minimum area of the blood vessel during a cardiac cycle, ρ is the blood density, and D is the arterial distensibility. This equation overcomes some limitations of the Moens–Korteweg formulation because it relates PWV directly to distensibility, a macroscopic and measurable quantity, without requiring assumptions about wall thickness or a single-valued elastic modulus [36].

In healthy young adults, aortic PWV values are typically in the range of 5–7 m/s, whereas values above 10 m/s are generally considered indicative of significant arterial stiffness and are associated with increased cardiovascular risk [37–39]. The 2024 ESC guidelines for the management of elevated blood pressure and hypertension confirm the threshold of 10 m/s as a marker of hypertension-mediated organ damage (HMOD) and additionally introduce brachial–ankle PWV > 14 m/s as an alternative criterion [40]. PWV increases progressively with age, and this increase is accelerated in the presence of cardiovascular diseases. For this reason, PWV has been proposed not only as a diagnostic marker but also as a tool for monitoring the efficacy of therapeutic interventions aimed at reducing arterial stiffness [41].

Although cfPWV remains the gold standard, its measurement requires dedicated equipment, specialised personnel, and cannot be performed continuously [42,43]. These limitations have led to the pursuit of alternative, simpler, and more accessible methods for assessing arterial stiffness [44], among which photoplethysmography has emerged as a particularly promising approach, as will be discussed in the following sections.

2.2 Photoplethysmography (PPG)

2.2.1 Historical Background and Development of PPG

Photoplethysmography (PPG) is a non-invasive optical technique used to detect blood volume changes in the microvascular bed of tissue. Although it is now ubiquitous in clinical devices and consumer wearables, its origins date back to the mid-1930s. The term *photoelectric plethysmography*, as it was originally known, was coined by Alrick B. Hertzman, who is widely regarded as the pioneer of this technique. In 1937, Hertzman published his first papers describing photoelectric measurements of blood volume pulsations in the fingers, toes, and nasal septum [45].

The early instrumentation was remarkably simple by modern standards. In the first reported setup, a beam of light from an ordinary automobile headlight bulb was directed onto the fingertip, which was placed above a shielded photoelectric cell of the photoemissive type. The resulting photoelectric oscillations, corresponding to variations in the blood content of the digit, were recorded by a string galvanometer after amplification. To minimise motion artefacts, the subject's arm was placed on a sling to promote muscle relaxation. Hertzman later refined the apparatus by using a pencil flashlight bulb mounted in a metal sleeve that could be brought into light contact with the skin, enabling reflectance-mode measurements from the hand surface [46,47].

Over the following three decades, Hertzman and colleagues made fundamental contributions to the understanding of the technique. In 1940, Hertzman and Dillon were the first to distinguish between the alternating current (AC) and direct current (DC) components of the PPG signal, measuring each with a separate amplifier [48]. Subsequent work focused on establishing the validity of photoelectric plethysmography for quantifying both blood volume changes and blood flow [49]. As semiconductor technology advanced, photodetectors have become smaller and more sensitive, enabling other researchers to apply this technique to a wider range of physiological studies.

One of the most transformative developments in the history of PPG was the invention of pulse oximetry. In 1974, the Japanese bioengineer Takuo Aoyagi [50], working at Nihon Kohden, observed that the pulsatile component of light transmission through tissue at two different wavelengths contained information about arterial blood oxygenation. By isolating the AC component, which originates primarily from arterial pulsations, from the DC component, which is influenced by venous blood and non-

pulsatile tissue, Aoyagi devised a method for estimating arterial oxygen saturation (SpO2) non-invasively and continuously. The first prototype pulse oximeter was produced in 1973, and the concept was subsequently commercialised by Minolta, Ohmeda, and Nellcor over the following decade [51]. Due to its enormous clinical impact, pulse oximetry became a mandated international standard for monitoring during anaesthesia [52].

Over the past three decades, the number of publications related to PPG has grown exponentially, particularly since 2013, driven by the integration of PPG sensors into wearable consumer devices such as smartwatches and fitness bands [53]. Today, PPG applications extend far beyond pulse oximetry and heart rate monitoring, encompassing blood pressure estimation, arterial stiffness assessment, respiratory rate extraction, stress evaluation, and peripheral vascular disease detection, as will be discussed in the subsequent sections of this chapter.

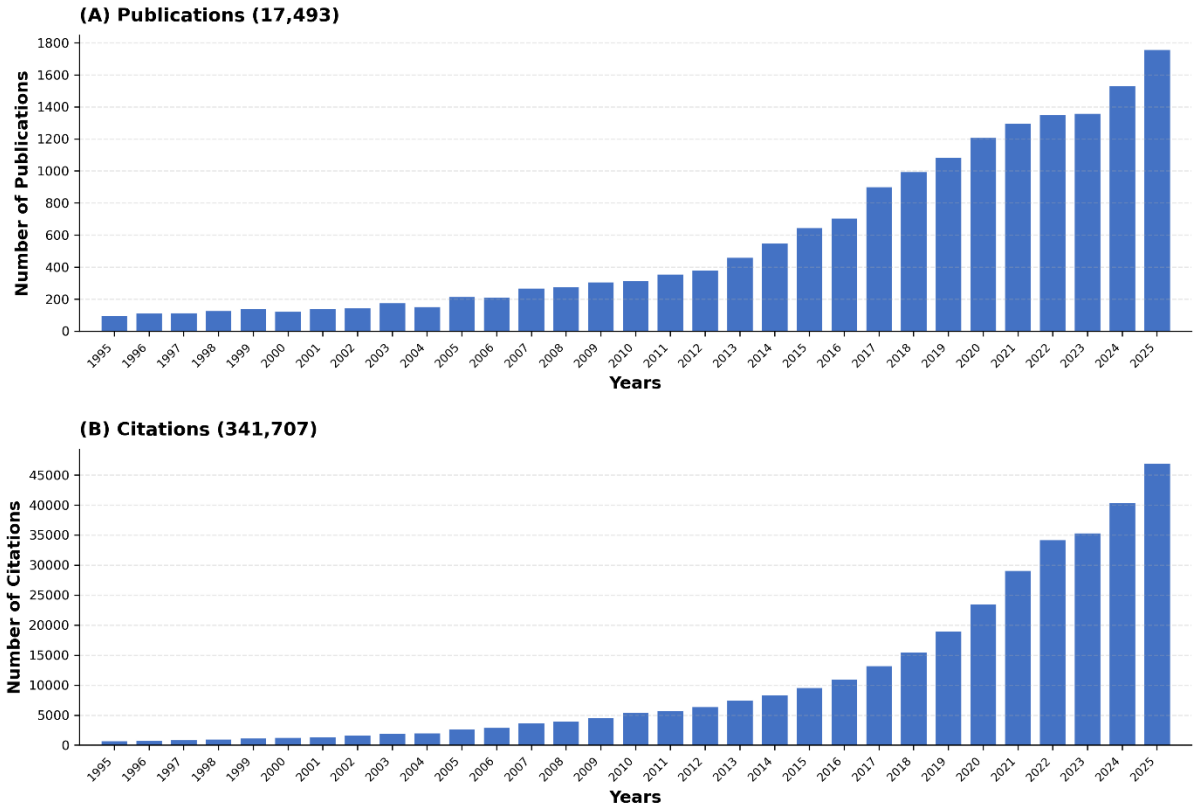

Figure 2.4 *(A) Publications (17,493) and (B) citations (341,707) of PPG studies over the past three decades (1995–2025). Data were obtained from Web of Science Core Collection using "Photoplethysmography" OR "Photoplethysmogram" OR "Photoelectric Plethysmography" OR "Photoplethysmographic" OR "Photoplethysmography PPG" OR "PPG" OR "Remote photoplethysmography" as topic (accessed April 16, 2026).*

2.2.2 PPG Sensors: Structure and Operating Principle

A PPG system comprises two essential functional blocks: an optical sensor and an electronic processing unit. The optical sensor consists of at least one light emitter and one photodetector, while the processing unit includes the analogue front-end circuitry for signal conditioning and an analogue-to-digital converter (ADC) for digitisation. In the simplest configuration, a single-wavelength PPG system illuminates a vascular tissue site with light at a specific wavelength, detects the transmitted or reflected photons, and converts the resulting photocurrent into a voltage signal that is filtered, amplified, and recorded as the photoplethysmogram [54].

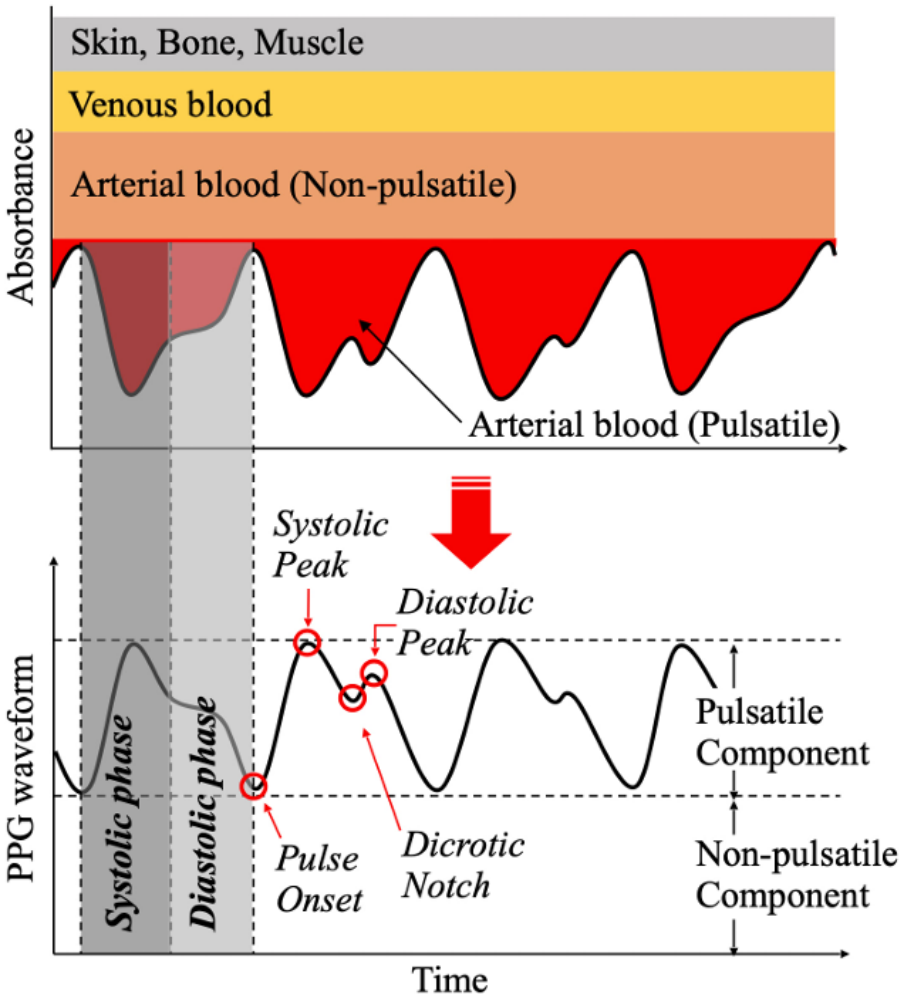

Figure 2.5 *Principle of photoplethysmogram generation and waveform features [54].*

The most commonly used light source in PPG sensors is the light-emitting diode (LED). LEDs are favoured due to their small footprint (typically 2 mm × 1.5 mm × 1 mm), low power consumption, widespread availability across the visible and near-infrared spectrum, and narrow emission bandwidth. When forward-biased, the p-n junction of the LED recombines electrons and holes, releasing energy in the form of photons at a

wavelength determined by the semiconductor material [55]. Green LEDs (around 520-530 nm) are widely used in wearable devices for heart rate monitoring, while red (660 nm) and near-infrared (940 nm) LEDs are employed in pulse oximeters for oxygen saturation measurement. The choice of wavelength has significant implications for signal quality and tissue penetration depth, as discussed in Section 2.2.4 [56,57].

The photodetector, most commonly a silicon photodiode, converts the optical energy of the detected photons into an electrical current (photocurrent) that is proportional to the incident light intensity. Other detector types, such as phototransistors and photocells, have been reported in the literature but are less frequently employed [58]. The photocurrent is then converted into a voltage signal by a trans-impedance amplifier (TIA), which is a critical stage of the analogue front-end. The TIA consists of an operational amplifier with a high-value feedback resistor (typically in the megaohm range) and a compensation capacitor that determines the circuit bandwidth and stability. The design of the TIA requires careful consideration, as improper selection of components can introduce oscillations, excessive noise, or signal distortion [59].

Following amplification, the PPG signal undergoes analogue filtering to remove high-frequency noise and mains interference (anti-aliasing filter), and bandwidth-limiting filters are used to separate the AC and DC components. The AC component, which varies with each heartbeat, typically occupies a frequency range of 0.5 to 5 Hz, while the DC component represents the quasi-static baseline of the signal. A further amplification stage is generally required before digitisation, given the small amplitude of the raw PPG signal. The digitisation is typically performed by a sigma-delta ADC, which offers high resolution (16-24 bits), low noise, and the capability of directly digitising the sensor output without prior DC removal [60].

The spatial arrangement of the LED and photodetector defines two fundamental measurement configurations. In *transmission mode* (also called trans-illumination), the LED and photodetector are placed on opposite sides of the tissue, so that light passes entirely through the tissue sample before reaching the detector. This configuration is limited to anatomical sites thin enough to be transilluminated, such as the fingertip, the earlobe, or the toe, and is the most widely used arrangement in clinical pulse oximetry. In *reflectance mode*, the LED and photodetector are mounted side by side, typically a few millimetres apart, so that the light enters the tissue, undergoes multiple scattering and absorption events, and a fraction of the backscattered light is detected. Reflectance

probes offer the advantage of being applicable to virtually any vascular tissue site, including the wrist, forehead, and forearm, and are therefore predominantly used in consumer wearable devices [61,62].

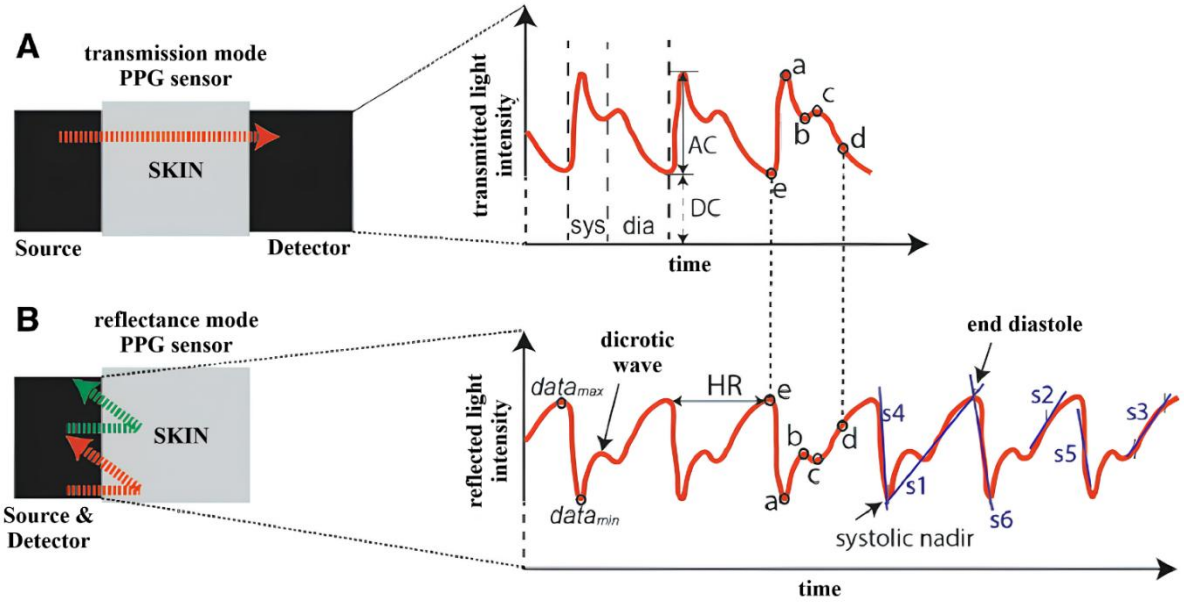

Figure 2.6 *Comparison of transmission and reflectance mode PPG sensors. The signal intensity and shape of transmitted PPG signal (A) behaves inverse to PPG signal detected by a reflectance mode PPG sensor (B) [62]*

Modern PPG systems often employ multiple wavelengths simultaneously, requiring more complex instrumentation. In a multiwavelength system, the LEDs are driven sequentially by time-multiplexed current drivers, and the mixed-wavelength signal at the output of the TIA is separated into individual wavelength channels using sample-and-hold amplifiers synchronised to the LED switching clocks. A programmable microcontroller coordinates the timing of LED activation and signal sampling. This architecture enables dual-wavelength pulse oximetry and, more recently, multispectral PPG systems that interrogate tissue at more wavelengths, providing richer physiological information [63,64]. Today, all the circuitry required to acquire PPG signals, including the optical components, signal conditioning amplifiers, and digitisation engine, can be integrated into a single chip, enabling the miniaturised PPG sensors found in wristbands and smartwatches [65].

2.2.3 The Beer-Lambert Law and Its Modification for Biological Tissue

The theoretical framework underlying the interaction of light with tissue in PPG is based on Beer-Lambert's law, one of the fundamental principles of spectrophotometry. Its development spans more than a century: in 1729, Pierre Bouguer first observed that the loss of light intensity through a medium is proportional to the intensity itself and to the path traversed. Johann Heinrich Lambert formalised this observation in 1760. Almost a century later, in 1852, August Beer demonstrated that the attenuation also depends on the concentration of the absorbing substance. The modern formulation, known as the Beer–Lambert law, combines both contributions [66,67].

According to the generic Beer–Lambert law, the absorbance A of monochromatic light passing through a homogeneous, non-scattering medium is given by:

$$A = \varepsilon \cdot d \cdot C \tag{2.4}$$

where ε is the molar extinction coefficient of the absorbing species, d is the optical path length (equal to the sample thickness in a non-scattering medium), and C is the molar concentration of the absorber. The transmitted intensity I_t is related to the incident intensity I_0 by an exponential decay:

$$I_t = I_0 e^{-\varepsilon \cdot d \cdot C} \tag{2.5}$$

However, biological tissue is a complex medium composed of multiple absorbers (haemoglobin, water, melanin) and scatterers (collagen fibres, cell membranes, organelles). The generic Beer–Lambert law does not account for scattering, and therefore cannot be directly applied to tissue. To address this, Delpy introduced a modification in 1988 [68]. In tissue, photons undergo multiple scattering events, travelling along tortuous paths that are considerably longer than the straight-line distance between source and detector. This elongation is quantified by the *differential path length factor* (DPF) and the effective optical path length l is related to the source–detector separation d by $l = \text{DPF} \times d$, with DPF always greater than unity. The modified Beer–Lambert law for a scattering–absorbing medium at a given wavelength λ is expressed as:

$$A_\lambda = \varepsilon_\lambda \cdot d \cdot DPF_\lambda \cdot C + G_\lambda \tag{2.6}$$

where the term G is a scattering-dependent parameter that accounts for geometry-related losses and does not depend on the concentration of the absorber. When multiple

absorbers are present, the total absorbance is simply the sum of the individual contributions of each chromophore, each weighted by its own extinction coefficient and concentration.

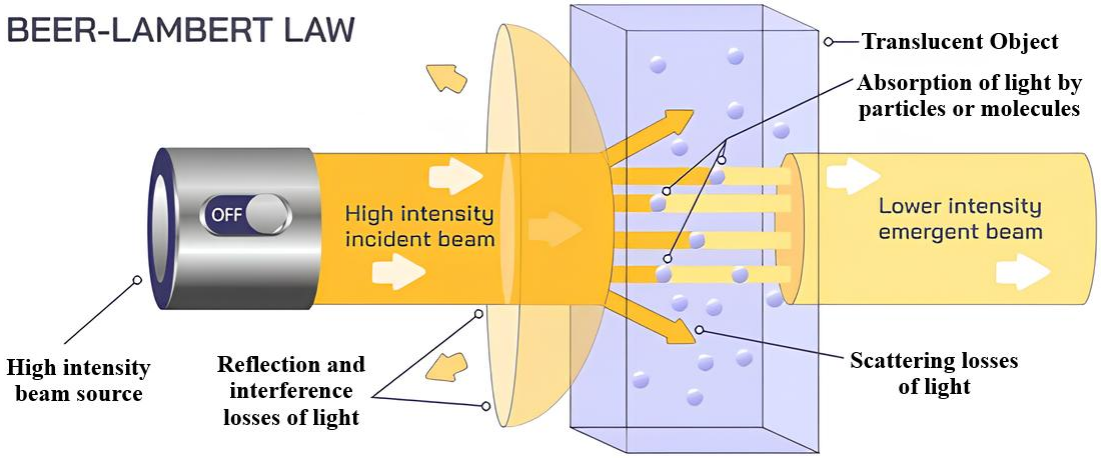

Figure 2.7 *Schematic representation of the Beer–Lambert law: a collimated light beam is attenuated as it traverses an absorbing and scattering medium, resulting in a lower-intensity emergent beam.*

The application of this framework to PPG is straightforward. During each cardiac cycle, the volume of arterial blood in the tissue increases during systole and decreases during diastole, causing a corresponding change in light absorbance. Since the scattering parameter G does not depend on the pulsatile blood volume, it remains approximately constant throughout the cardiac cycle [69].

This framework also underpins pulse oximetry. In a dual-wavelength system (typically red at 660 nm and near-infrared at 940 nm), a quantity known as the *ratio of ratios* (R) is computed from the PPG signals at the two wavelengths:

$$R = \frac{AC_{\lambda 1}/DC_{\lambda 1}}{AC_{\lambda 2}/DC_{\lambda 2}} \tag{2.7}$$

where AC and DC denote the pulsatile and non-pulsatile components of the PPG signal at each wavelength. Because oxyhaemoglobin (HbO_2) and deoxyhaemoglobin (Hb) have markedly different extinction coefficients in the red and near-infrared regions, the value of R can be related to arterial oxygen saturation (SpO_2) through empirical calibration curves. This elegant approach, first conceived by Aoyagi, remains the foundation of all modern pulse oximeters [70,71].

2.2.4 Physical Principles of Light-Tissue Interaction

When light is directed at a biological tissue site, it undergoes two fundamental interaction processes: *absorption* and *scattering*. Their relative contributions depend on the wavelength of the incident light and on the structural and biochemical composition of the tissue layers [72]. Absorption occurs when photon energy is transferred to chromophores, molecules that selectively absorb light at specific wavelengths. The principal chromophores in the spectral window relevant to PPG (approximately 450–1100 nm) are oxyhaemoglobin (HbO_2) and deoxyhaemoglobin (Hb) in blood, melanin in the epidermis, and water in the deeper tissue layers. HbO_2 and Hb exhibit markedly different absorption profiles between 600 and 1000 nm, which forms the physical basis of pulse oximetry [73]. Scattering refers to the redirection of photons caused by structural inhomogeneities such as cell membranes, collagen fibres, and organelles. Since the scattering coefficient decreases with increasing wavelength, longer wavelengths penetrate deeper into tissue [74].

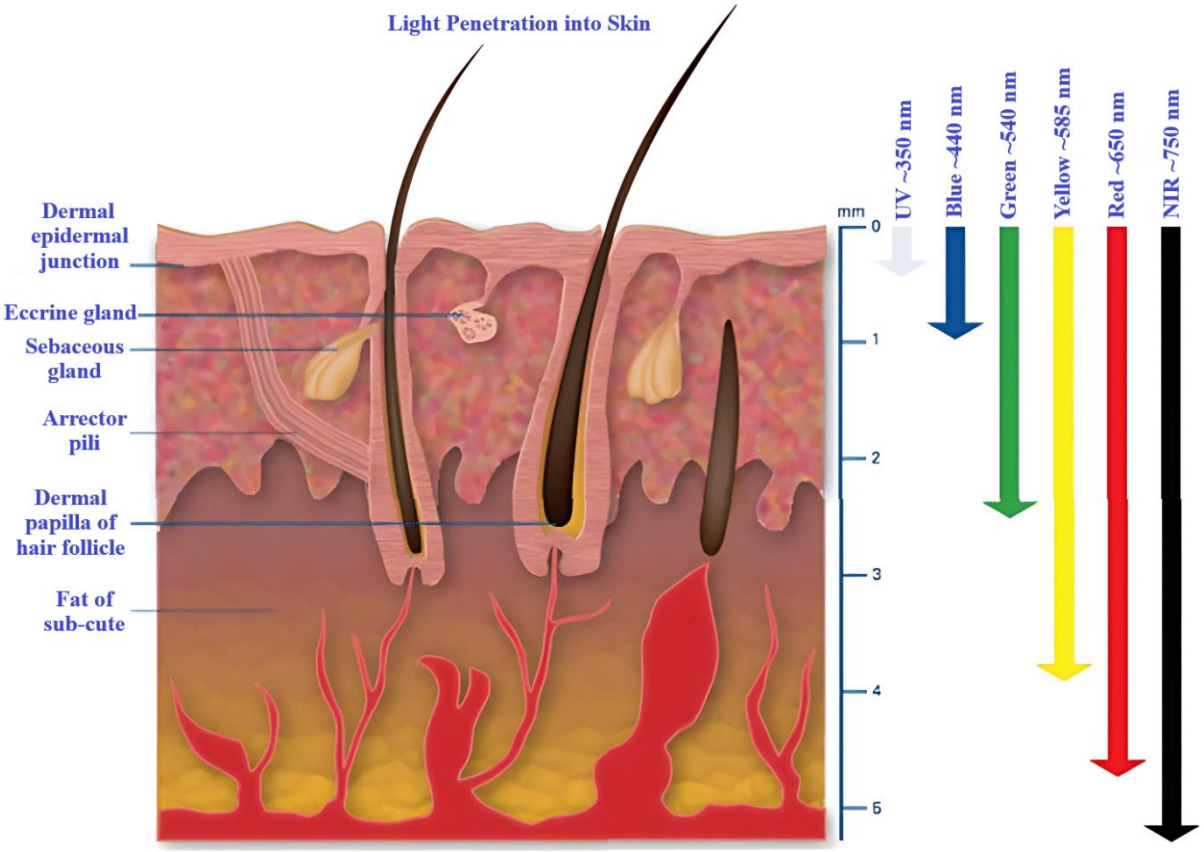

Figure 2.8 *Light penetration into skin illustrating the depth to which wavelengths penetrate human skin. Red light is extinguished some 4–5 mm beneath the surface of the skin whereas ultraviolet hardly penetrates at all and blue barely 1 mm into tissue [75]*

The combined effects of absorption and scattering determine the *optical penetration depth*, a parameter with critical implications for PPG sensor design because it dictates which tissue layers and vascular structures are interrogated by a given wavelength. In particular, blue light (~440 nm) is confined to the superficial epidermis, with a penetration depth of approximately 0.2 mm, while green light (~540 nm) reaches the papillary dermis at about 0.3 mm. Red light (~650 nm) penetrates through all dermal sublayers to the subcutaneous fat layer (~1.5 mm), and near-infrared light (~ 750 nm) achieves the deepest penetration, extending beyond the subdermis into muscle tissue at depths exceeding 2.5 mm. At higher near-infrared wavelengths (above 1000 nm), penetration decreases again due to the increasing dominance of water absorption [75].

2.2.5 The PPG Signal: Components and Waveform Morphology

The PPG signal represents the time-varying intensity of light attenuated by tissue. This attenuation has both a pulsatile and a non-pulsatile component, giving rise to the two fundamental constituents of the PPG waveform. The *direct current (DC) component* constitutes the largest portion of the signal and originates from the quasi-static absorption by non-pulsatile structures: bone, muscle, connective tissue, venous blood, and the baseline arterial blood volume. It also exhibits slow oscillations (below 0.5 Hz) associated with respiration, sympathetic nervous system activity, and thermoregulatory vasomotion. The *alternating current (AC) component*, superimposed on the DC baseline, reflects the pulsatile arterial blood volume changes synchronous with each heartbeat. Its amplitude is typically only 1–2% of the DC level. Since higher blood volume corresponds to lower detected intensity, the signal is conventionally displayed inverted, so that the systolic peak appears as an upward deflection [54].

Each cardiac cycle produces a single PPG pulse wave with a characteristic morphology consisting of two phases. The *anacrotic phase* corresponds to the rapid increase in blood volume during ventricular ejection, culminating in the systolic peak. The *catacrotic phase* reflects the gradual decrease in blood volume; within it, a small inflection known as the *dicrotic notch* marks aortic valve closure, often followed by a secondary *diastolic wave*. The overall waveform morphology is shaped by cardiac output parameters, vascular properties, respiratory modulation, autonomic nervous system activity, and the presence of pathological conditions [76].

A well-documented effect is the change in PPG waveform associated with healthy ageing. In young adults, the pulse wave exhibits a clear dicrotic notch and a prominent

diastolic wave, reflecting good arterial compliance. With advancing age, increasing arterial stiffness causes the reflected pressure wave to return earlier in the cardiac cycle, merging with the forward-travelling systolic wave, progressively blurring the dicrotic notch and attenuating the diastolic wave until a single dominant peak remains [18,76]. These age-related changes underpin the use of PPG pulse wave analysis for vascular ageing assessment, a central topic of this thesis.

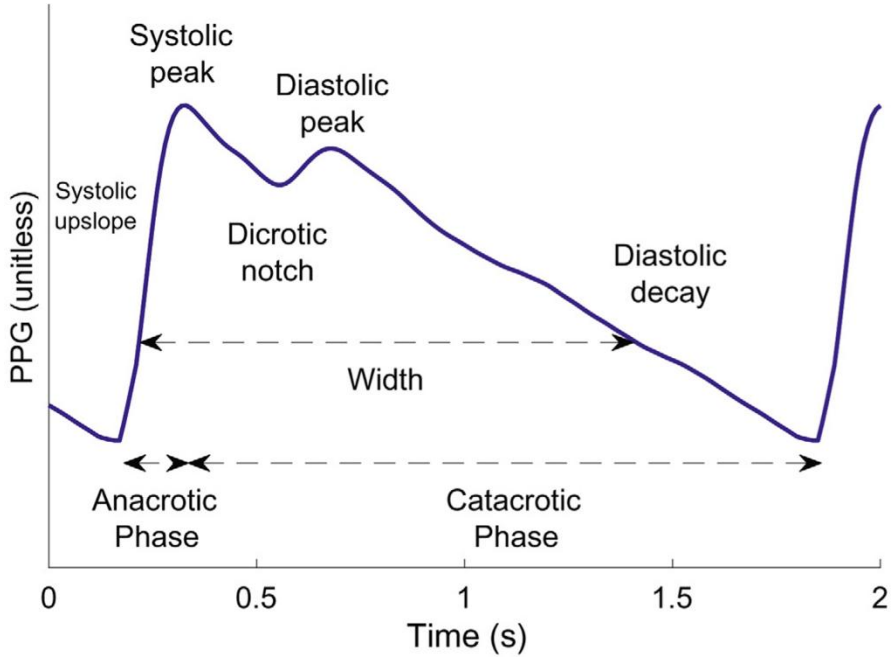

Figure 2.9 *A typical photoplethysmogram (PPG) pulse wave [76]*

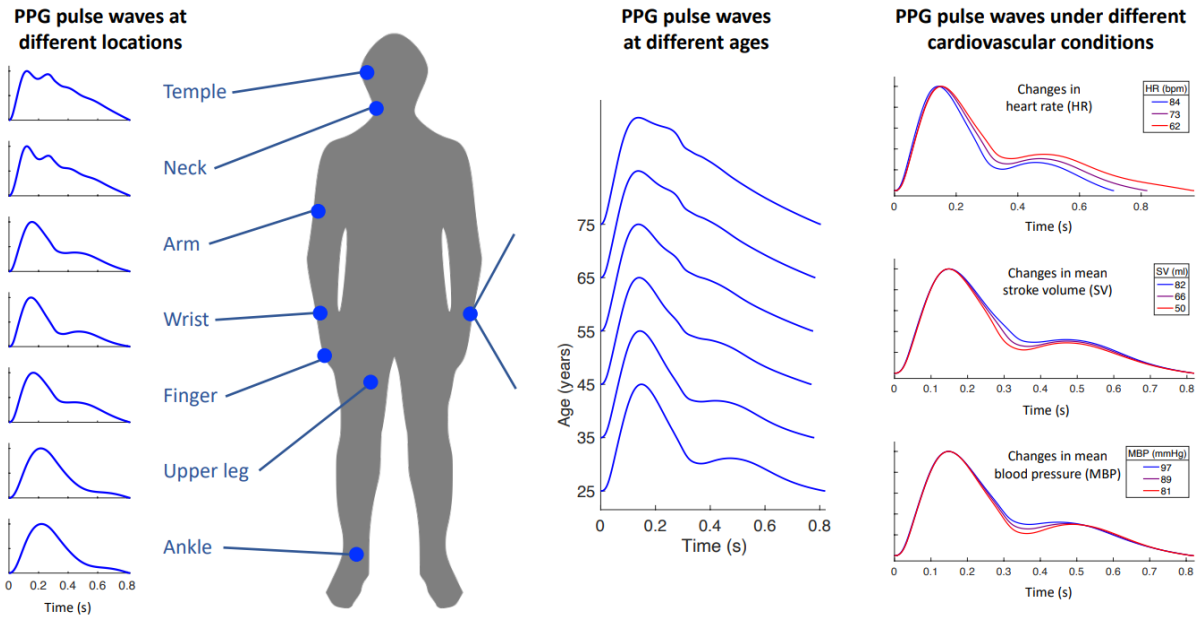

Figure 2.10 *PPG pulse waves: (i) at different locations around the body (healthy 25-year-old); (ii) for healthy subjects of different ages; (iii) under different cardiovascular conditions [76]*

2.2.6 Established Clinical Applications

Since its inception, PPG has been adopted in a wide range of clinical and consumer health applications. The versatility of this technique stems from the richness of physiological information encoded in its waveform, combined with the simplicity and low cost of the required hardware. The following paragraphs provide an overview of the principal established applications.

Pulse oximetry remains the most widespread and clinically relevant application of PPG. By exploiting the differential absorption of oxyhaemoglobin and deoxyhaemoglobin at red and near-infrared wavelengths, pulse oximeters provide a continuous, non-invasive estimate of arterial oxygen saturation (SpO_2). This measurement has become an indispensable component of patient monitoring during anaesthesia, in intensive care units, during post-operative recovery, and in neonatal screening for congenital heart disease. The development of motion-resistant pulse oximetry has further expanded its utility to ambulatory and wearable settings [77].

Heart rate monitoring is the simplest and most direct application of PPG. Since each arterial pulse produces a corresponding peak in the PPG waveform, heart rate can be derived by detecting the inter-beat interval. This application is now ubiquitous in consumer wearable devices, including smartwatches and fitness trackers, where green-wavelength reflectance PPG sensors on the wrist provide continuous heart rate data during daily activities and exercise [78].

Blood pressure estimation using PPG has attracted considerable research interest as a potential alternative to cuff-based sphygmomanometry. The most established approach exploits *pulse transit time* (PTT), the time required for the arterial pulse wave to travel between two measurement sites. Since PTT has a well-understood inverse relationship with blood pressure, mediated by the pressure-dependent arterial compliance, it can be calibrated to yield blood pressure estimates. PTT can be measured using the time delay between an electrocardiogram (ECG) R-wave and a distal PPG pulse, or between two PPG signals at different body sites. More recently, approaches based on pulse wave analysis (PWA) have also been investigated, extracting morphological features from a single PPG waveform that correlate with blood pressure changes. However, the generalisability and clinical accuracy of these methods remain areas of active research [79–81].

Peripheral vascular disease (PVD) assessment is one of the earliest clinical applications of PPG. By recording PPG waveforms from the toes or fingers, clinicians can evaluate the adequacy of peripheral perfusion and detect the presence of occlusive arterial disease. The amplitude, contour, and timing features of the peripheral PPG pulse provide information about the patency of the arterial supply. Multisite PPG measurements, comparing waveforms from the head, hands, and feet, have also been developed for the simultaneous assessment of bilateral peripheral vascular function [82,83].

Arterial stiffness and vascular ageing assessment using PPG is an increasingly active area of investigation, and one that is central to the work presented in this thesis. PPG-based approaches to arterial stiffness estimation include regional pulse wave velocity measurement, where the transit time of the pulse wave between two PPG sensors placed at known distances apart is used to calculate PWV. Additionally, PPG pulse wave analysis methods extract morphological indices from the waveform that are sensitive to changes in arterial compliance. Among these, the analysis of the second derivative of the PPG signal (acceleration plethysmography, APG) has been shown to provide indices that correlate with arterial stiffness and vascular age, as will be discussed in detail in Section 2.3 [84–87].

Other notable applications include *respiratory rate estimation* from the modulation of the PPG signal by breathing, *autonomic function assessment* through heart rate variability analysis derived from PPG inter-beat intervals, *venous assessment* for the detection of venous insufficiency and reflux, and *anaesthesia and surgical monitoring* where PPG-derived perfusion indices provide information about peripheral haemodynamic status. The recent integration of PPG sensors into smartphones, smartwatches, and other wearable platforms has further expanded the range of potential applications, enabling continuous, long-term, out-of-hospital monitoring of cardiovascular health parameters that were previously accessible only in clinical settings [88–90].

2.3 Photoplethysmography Signal Processing and Analysis

2.3.1 Signal Processing Fundamentals

The processing of a raw PPG signal is conventionally organised as a sequential pipeline encompassing preprocessing, pulse segmentation, feature extraction, and, depending on the application, parameter estimation. Although the specific implementation varies across studies, the community has converged on a set of shared principles, systematised in recent comprehensive reviews [76,91]. Figure 2.11 summarises the pipeline adopted in this thesis.

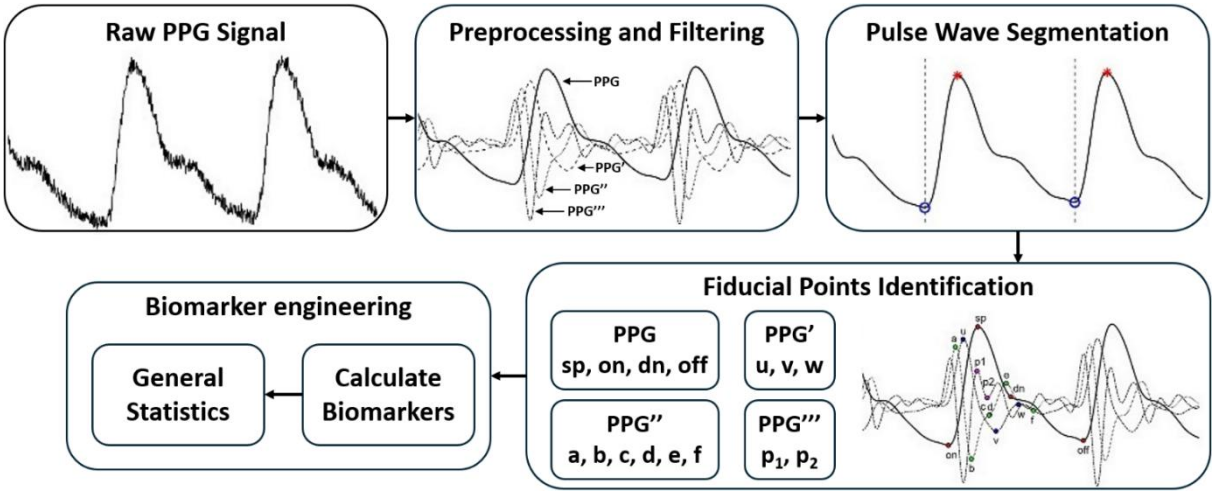

Figure 2.11 *Pipeline for continuous PPG time series analysis. The terms PPG', PPG'', and PPG''' correspond to the first, second, and third derivatives of the PPG signal, respectively.*

The first stage of preprocessing aims to attenuate noise and interferences while preserving the morphological content of the waveform. Digital filtering is universally employed, since most sources of noise, such as high-frequency electronic noise and low-frequency baseline drift caused by respiration and vascular movement, lie outside the cardiac spectral range, which is concentrated approximately between 0.5 and 15 Hz, with most of the signal energy contained in the first four harmonics of the fundamental heart rate [92].

Two families of filters are most commonly used: Finite Impulse Response (FIR) filters and Infinite Impulse Response (IIR) filters. FIR filters are intrinsically stable and have a linear phase response, which preserves the timing relationships between waveform features but requires a relatively high filter order to achieve sharp transitions. IIR filters achieve equivalent frequency selectivity with a lower order, and therefore with lower computational cost, at the price of a non-linear phase response that can shift and distort

pulse morphology [93,94]. Among IIR designs, the Butterworth, Bessel, Elliptic, and Chebyshev Type I and II responses are the most widely adopted [91].

The choice of filter type has been explicitly addressed by two recent and highly relevant studies. Liang et al. [92] systematically compared ninety combinations of filter type and order on short PPG records, and identified the fourth-order Chebyshev Type II bandpass filter as providing the best trade-off between noise attenuation and morphological preservation. This result was independently confirmed by Lapitan et al. [91], who quantified the waveform distortions introduced by five IIR filter families across three filter orders, using the skewness signal quality index, the reflection index, and the ejection-time compensated as distortion metrics. Their study confirmed that Butterworth, Bessel, Elliptic, and Chebyshev Type I filters behave similarly in preserving pulse morphology, whereas the Chebyshev Type II filter shows an ambiguous behaviour: the second-order version introduces severe waveform distortions (including the loss of the dicrotic notch), while the fourth-order and sixth-order versions strongly enhance signal quality as measured by skewness. Based on this combined evidence, the experimental work presented in Chapters 5, 6, and 7 of this thesis adopts a fourth-order Chebyshev Type II bandpass filter with a passband of 0.5–8 Hz and a stopband attenuation of 20 dB for PPG preprocessing.

The selection of cut-off frequencies represents a compromise between noise rejection and waveform preservation. No universal standard exists, but the empirical consensus places the lower cut-off between 0.05 and 0.5 Hz to remove baseline wander without attenuating the diastolic component and the upper cut-off between 8 and 20 Hz, to suppress high-frequency noise while preserving the inflection points needed for derivative analysis [76,95]. A further consideration concerns phase distortion: when the cut-off frequencies approach the dominant harmonics of the PPG, IIR filters introduce non-negligible group delays that can reach hundreds of milliseconds and shift the position of fiducial points [91,96].

Once the signal has been filtered, the next stage consists in the identification of individual cardiac cycles. Systolic peak detection is commonly performed through adaptive thresholding, zero-crossing of the first derivative, slope-sum functions, or through wavelet-based and machine-learning approaches [97–99]. Once the onset and the peak of each pulse have been located, the waveform can be segmented into individual beats for subsequent analysis.

2.3.2 Factors Influencing PPG Signal Quality

The accuracy of any measurement derived from PPG is ultimately determined by the quality of the acquired signal, which in turn is influenced by a diverse set of parameters. These can be grouped into three broad categories, namely physiological, technical, and environmental [100]. Understanding and, where possible, controlling these factors is a prerequisite for the clinical and research use of PPG, and was an explicit objective of part of the experimental work carried out during this doctoral project [101–103].

The most fundamental physiological determinant of PPG signal amplitude is the pulsatile blood volume itself, which in turn depends on cardiac output, vascular tone, and local perfusion. Peripheral vasomotion introduces low-frequency modulations of the DC baseline at frequencies typically below 0.1 Hz. Respiration superimposes three distinct modulations on the PPG signal: baseline wander, amplitude modulation, and frequency modulation, whose combined effect can distort morphological features if not properly filtered out [104,105]. With advancing age, the dicrotic notch gradually diminishes and the prominence of the late systolic and early diastolic components of the pulse wave decreases, as already explained in Section 2.2.5; this phenomenon directly justifies the use of derivative-based analysis for vascular assessment [106]. Skin pigmentation, quantified through the Fitzpatrick scale, affects light absorption by epidermal melanin and has been shown to reduce the signal-to-noise ratio and to increase heart-rate estimation errors in subjects with darker skin tones, particularly during physical activity [107,108].

Among the technical determinants of PPG quality, the sensor-to-skin contact pressure is one of the most critical and least standardised. Two opposite extremes can be identified: an insufficient contact pressure allows external light to reach the photodetector, promotes motion artifacts, and results in a non-optimal optical coupling; conversely, an excessive contact pressure compresses the underlying capillary bed, altering the very quantity being measured and distorting the pulsatile component [109,110]. Other technical factors include the choice of wavelength (see Section 2.2.4), the optical configuration (transmission versus reflectance) and the stability of the analogue front-end and of the analogue-to-digital converter.

The measurement site can also be considered a strictly technical choice, given its decisive influence on signal morphology and clinical interpretation. The fingertip provides a high-amplitude pulsatile signal, thanks to the finger’s dense terminal vascular network, but is less suitable for continuous monitoring via wearable devices.

The wrist, which has become the standard site for commercial wearable devices, offers the opposite trade-off: comfort and acceptability at the cost of a more attenuated and morphologically variable signal, since the radial and ulnar arteries lie beneath multiple layers of connective tissue and tendons [111,112]. The earlobe, forehead, and toes represent niche alternatives used in specific clinical contexts.

Among the most common external factors is motion-induced noise, which is widely regarded as the primary source of interference affecting PPG signals, particularly in wearable and sports applications [57,113]. Large-scale body movements, tremors, coughing and even speech can produce signal distortions that cover the same frequency range as physiological variations, making filter-based removal only partially effective. A wide range of mitigation strategies has been proposed, including adaptive filtering using reference signals from accelerometers or gyroscopes, independent component analysis, empirical mode decomposition, wavelet denoising, and model-based exclusion of poor-quality heartbeats [114–117].

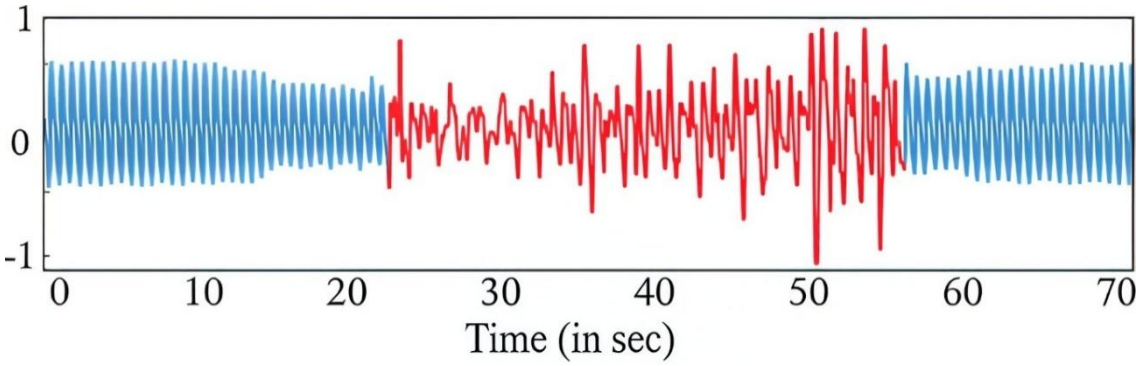

Figure 2.12 *An instance of a motion-contaminated PPG signal (shown in red), obtained from a smartwatch [117]*

External temperature acts on the PPG signal through the physiological mechanism of thermoregulatory vasomotion: cold exposure triggers peripheral vasoconstriction, reducing blood volume in the microvascular bed and attenuating the pulsatile component, whereas warmth induces vasodilation with the opposite effect. These effects are particularly relevant in wearable and ambulatory contexts, where environmental conditions cannot be controlled [118,119]. Ambient light pollution represents a further environmental concern, since any external light reaching the photodetector introduces spurious components into the signal; optically insulated probe designs, differential acquisition schemes, and dedicated cancellation stages in the readout circuitry have been proposed to mitigate this effect [58,120].

2.3.3 Derivatives of the PPG Signal

Although the raw PPG waveform carries a remarkable amount of physiological information, several clinically relevant inflection points are subtle and difficult to identify by visual inspection, particularly in older subjects or in the presence of reduced arterial compliance [121–123]. The mathematical differentiation of the PPG signal represents a powerful and well-established strategy to overcome this limitation: successive derivatives progressively amplify local changes in curvature, transforming barely visible shoulders and inflections of the original waveform into clearly detectable extrema. The historical introduction of derivative analysis dates back to Ozawa, who in 1972 and 1978 first demonstrated that the first and second derivatives of the PPG carry characteristic waveform features that facilitate the interpretation of the original signal, as retrospectively reported by Takazawa et al. [124]. This section describes the three most commonly used PPG signal derivatives and the numerical strategies employed to calculate them reliably. Figure 2.13 illustrates the progressive amplification of morphological details across the hierarchy of derivatives.

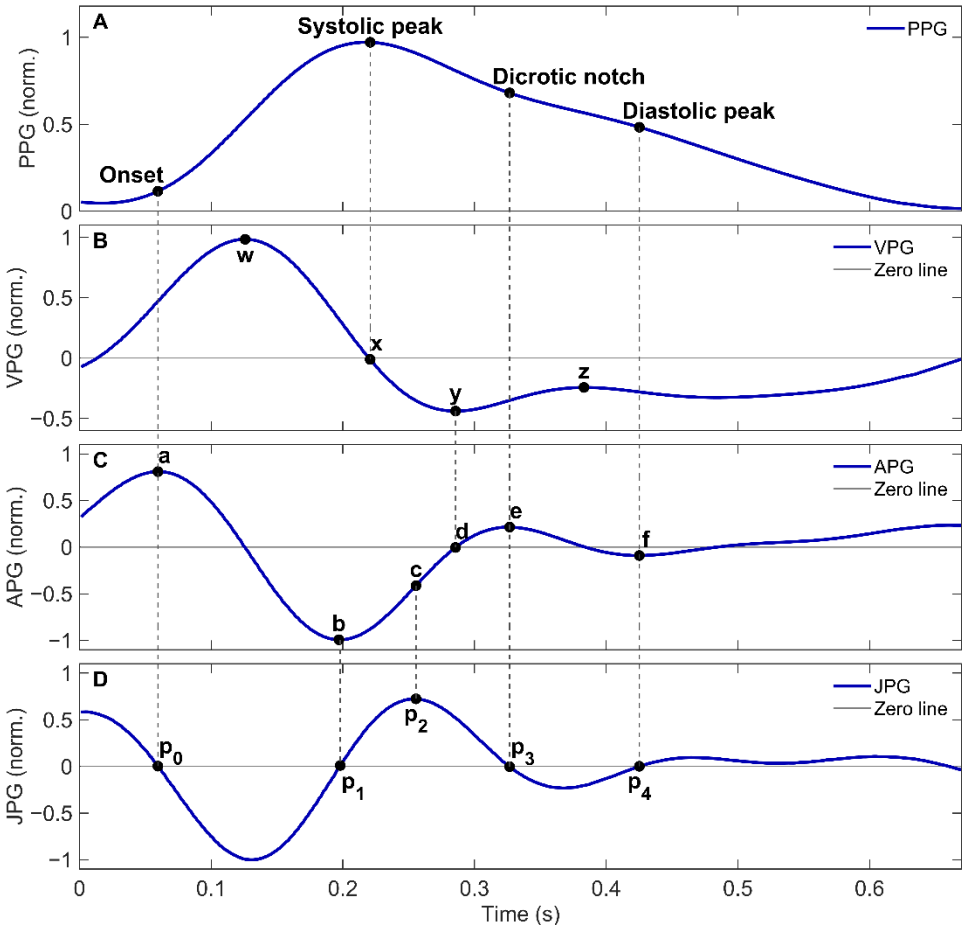

Figure 2.13 *Photoplethysmographic waveform and its successive time-derivatives. (A) PPG signal; (B) first derivative (VPG); (C) second derivative (APG); (D) third derivative (JPG).*

The first derivative of the PPG signal, also known as the Velocity Plethysmogram (VPG), represents the rate of change of blood volume in the microvascular bed and, under the standard haemodynamic assumptions, is proportional to the local blood flow velocity. The VPG typically exhibits three prominent features: a positive peak (u-peak) corresponding to the maximum systolic upslope, a negative peak (v-peak) associated with the minimum slope point in late systole, and a second positive peak (w-peak) associated with the maximum slope in diastole [125]. The morphology of the VPG can be used in pulse onset detection algorithms and in the estimation of pulse transit time through maximum-slope methods [126].

The second derivative of the PPG signal was brought to the attention of the international scientific community by the seminal work of Takazawa et al. in 1998, who demonstrated its clinical utility for the non-invasive assessment of vascular ageing and of the effects of vasoactive agents [124]. It is referred to in the literature by several names, including Second Derivative Photoplethysmogram (SDPPG, also abbreviated SDPTG in the original work) and Acceleration Plethysmogram (APG). Following the terminological recommendation of Elgendi [127], this thesis adopts the APG notation consistently. From a physical standpoint, the APG expresses the rate of change of the velocity of blood volume and thus represents a proxy for the local acceleration of peripheral blood flow. From a morphological standpoint, the APG highlights five characteristic deflections, conventionally labelled a, b, c, d, and e, that are directly linked to specific phases of the cardiac cycle [128]. These waves and the algorithms used to detect them are described in detail in Section 2.3.4.

The third derivative of the PPG signal, although it has received less attention than the APG, has established itself as a useful complement for the detection of landmarks and features in the PPG signal. The third derivative, known as the Jerk Plethysmogram (JPG), physically represents the rate of change of acceleration [129]. The usefulness of this higher-order derivative stems from a fundamental mathematical property: the points where the JPG crosses zero correspond, by definition, to the maxima and minima of the APG. When the morphology of the APG is not well defined, as is frequently the case for waves c and d in older subjects, the JPG can provide independent confirmation of the position of the corresponding reference points [130]. This multi-derivative strategy offers a robust framework for landmark detection across a wide range of age groups and clinical conditions [131].

2.3.4 APG Waveform, Fiducial Points and Clinical Interpretation

The APG waveform, obtained as the second derivative of the filtered PPG signal, exhibits a characteristic morphology consisting of five distinct deflections representing the APG fiducial points. Each wave reflects a specific haemodynamic event and provides complementary information on the structural and functional status of the arterial tree [132].

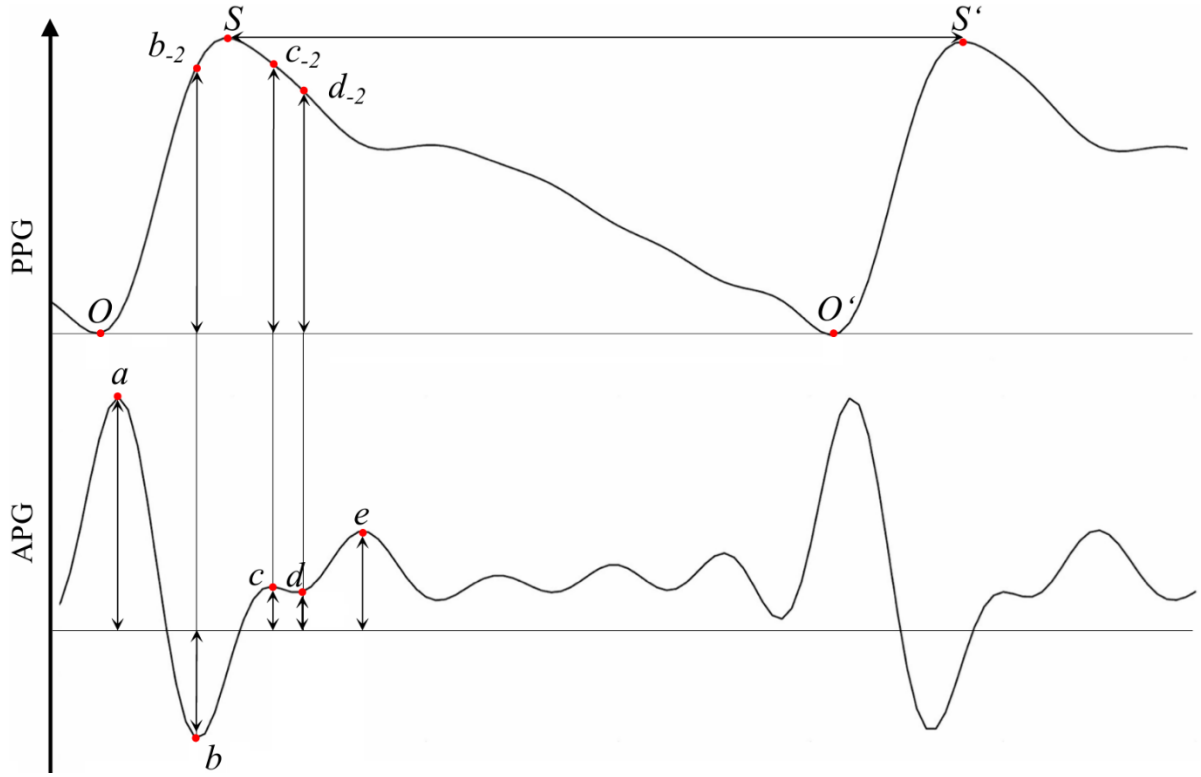

Figure 2.14 *Schematic representation of the PPG waveform (top) and its corresponding second derivative (bottom) with the five characteristic fiducial points a, b, c, d, and e [132].*

The *a* wave is the first and most prominent deflection of the APG and corresponds to a pronounced positive peak. Physiologically, it marks the onset of systole and coincides with the maximum acceleration of blood flow at the beginning of ventricular ejection, as the aortic valve opens and the pressure pulse propagates along the arterial tree. Because of its amplitude and its robust morphological signature, the a wave is used as the reference amplitude for the normalisation of all the other fiducial points and is conventionally identified as the global maximum of the APG within each cardiac cycle. The *b* wave is the first negative deflection of the APG and typically represents the global minimum of the waveform. It corresponds to the rapid deceleration of blood flow that follows the initial systolic acceleration, occurring when the forward pressure wave is counterbalanced by peripheral resistance and by the early-returning reflected waves.

The *c* wave is a smaller positive deflection that appears after the b wave and is physiologically attributed to the re-acceleration of blood flow caused by reflected waves arriving from the peripheral circulation. Its amplitude is strongly modulated by arterial compliance: stiffer arteries generate earlier and larger reflected waves, which alter both the timing and the magnitude of the c wave. The *d* wave is the second negative deflection of the APG, occurring shortly after the c wave. It represents the late systolic re-decrement wave, related to the timing and magnitude of the reflected waves. Finally, the *e* wave is the third positive deflection of the APG, associated with the dicrotic notch and closure of the aortic valve.

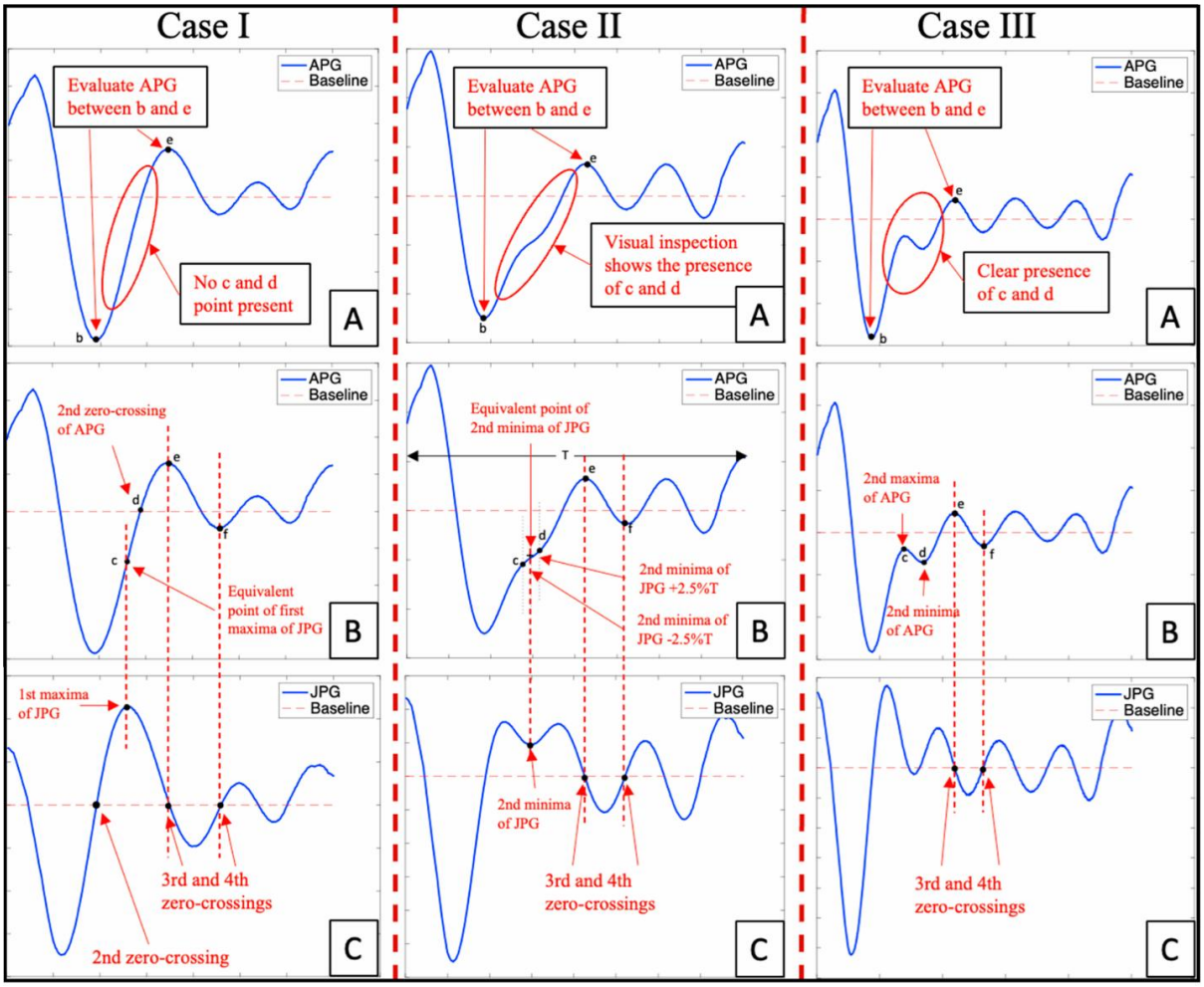

Figure 2.15 *Three-case classification of the APG morphology. (A) APG segment evaluated between the b and e waves; (B) identified c and d fiducial points; (C) corresponding JPG waveform used as auxiliary reference. In Case I the c and d waves are absent from the APG and are recovered from JPG zero-crossings and extrema; in Case II they are faintly present and estimated around the second minimum of the JPG; in Case III they are prominent and identified directly on the APG [130].*

In subjects with good arterial compliance, typically young and healthy, all five waves are clearly distinguishable, and the a, b, c, d, e sequence is fully preserved. However, recent studies have shown that the morphological clarity of the APG signal decreases with age, and in the presence of cardiovascular disease, the c and d waves progressively flatten until they can no longer be reliably identified. Abdullah et al. [130] classified this pattern as "Case I", characterised by the absence of prominent c- and d-waves in the APG signal, and proposed a multi-derivative detection strategy that utilises the first and third derivatives of the PPG signal to identify the corresponding fiducial points.

From the amplitudes of the five fiducial points, a family of dimensionless indices has been defined to quantitatively characterise the state of the arterial tree. These indices, conventionally referred to as APG indices, constitute the primary analytical tools adopted in Chapters 5, 6, and 7 of this thesis for the non-invasive assessment of vascular ageing. Their mathematical formulation, introduced by Takazawa et al. [124], and their clinical interpretation are summarised in Table 2.1.

Table 2.1 *APG indices: mathematical formulation and clinical interpretation.*

Index	Formula	Clinical Interpretation
b/a ratio	b ÷ a	Increases with age. Indicator of increased arterial stiffness and reduced distensibility of peripheral arteries [132,133]
c/a ratio	c ÷ a	Decreases with age. Reflects the late systolic component and vascular compliance [124]
d/a ratio	d ÷ a	Decreases with age. Reflects the increase in late systolic pressure in the ascending aorta caused by peripheral reflected waves [134]
e/a ratio	e ÷ a	Decreases with age. Reflects diastolic function and the dicrotic wave amplitude. [128]
AGI	(b−c−d−e) ÷ a	The most comprehensive index for assessing vascular ageing. Increases with age. Useful for screening for atherosclerosis and cardiovascular risk stratification [135]

Chapter 3 — State of the Art

3.1 Non-Invasive Methods for Arterial Stiffness Estimation

Over the last three decades, the evolution of arterial stiffness from a haemodynamic concept to a clinically applicable biomarker has driven the development of a diverse range of non-invasive techniques. These methods differ in terms of the segment of the arterial tree analysed (regional, local or systemic), the physical transducer used (tonometric, piezoelectric, oscillometric, ultrasound, magnetic resonance or optical) and the underlying assumptions linking the measured parameter to wall mechanics.

The landscape is defined by three authoritative consensus documents that continue to guide all subsequent validation activities: the original European expert consensus on arterial stiffness [136], the Artery Society's methodological standard for measuring carotid-femoral pulse wave velocity (cfPWV) [137] and the American Heart Association's scientific statement on the standardisation of vascular research [138]. These documents have recently been supplemented by the 2018 and 2024 guidelines of the European Society of Cardiology / European Society of Hypertension, which established a cfPWV threshold of 10 m/s as a marker of hypertension-mediated organ damage [40,139], and by the 2024 joint VascAgeNet/ARTERY recommendations for the validation of non-invasive PWV measurement devices [140], which codify device-independent validation requirements and formalise the concept of early vascular ageing as a clinical endpoint.

Building on the fundamentals of haemodynamic and wall mechanics introduced in 2.1.3, the present section reviews the state of the art of non-invasive arterial stiffness estimation from three complementary perspectives. Sub-section 3.1.1 surveys the conventional clinical techniques that currently populate the diagnostic landscape and that represent, at the time of writing, the reference against which any new device must be validated. Sub-section 3.1.2 focuses on the photoplethysmography-based family of approaches, which, unlike tonometric and oscillometric devices, can be implemented through low-cost, operator-independent, and miniaturised sensors suitable for wearable and ambulatory deployment. Sub-section 3.1.3, finally, provides a dedicated critical review of the second derivative of the PPG signal (APG) as a surrogate of vascular ageing, which constitutes the principal analytical tool of Chapters 5, 6, and 7 of this thesis.

3.1.1 Conventional Techniques

The clinical landscape for non-invasive arterial stiffness assessment is articulated around three measurement scales, namely regional, local and systemic, each populated by specific device families with distinct physical principles, accuracy profiles and operational constraints. As outlined in Section 2.1.3, regional carotid–femoral pulse wave velocity (cfPWV) constitutes the methodological reference and is operationalised by recording the foot-to-foot transit time of the pressure wave between the carotid and femoral sites, dividing it by 0.8 times the direct surface distance to approximate the aortic path length [141]. Age- and blood-pressure-stratified reference values from 16,867 subjects pooled across thirteen European centres provide the normative framework against which all subsequent device-specific validations are now benchmarked [142].

Within the tonometric family, the SphygmoCor system (AtCor Medical) implements ECG-gated sequential applanation tonometry and remains the most widely cited platform in epidemiological cohorts, including the Framingham Heart Study [143]. Its hybrid evolution, the SphygmoCor XCEL, combines a brachial cuff with carotid tonometry and extends the technique to operators without specialised training [144]. The PulsePen device (DiaTecne) adopts either a single ECG-gated tonometer or a dual-tonometer simultaneous configuration, with reported short-term coefficients of variation of 8.0% and 5.8%, respectively [145,146]. Piezoelectric solutions such as the Complior system (Alam Medical) acquire carotid and femoral mechanograms simultaneously through piezoelectric transducers and apply a second-derivative foot-detection algorithm; their cfPWV values are systematically about 2 m/s higher than SphygmoCor estimates, a discrepancy historically traceable to differences in distance conventions and now of central importance for cross-device comparability [147].

Oscillometric cuff-based devices, including the Mobil-O-Graph (IEM) and the Arteriograph (TensioMed), reconstruct the central aortic waveform from brachial pressure pulses through proprietary transfer functions and anthropometric path-length assumptions. Although operator-independent and well suited for ambulatory monitoring (with reported coefficients of variation around 3.4% for Mobil-O-Graph), they tend to underestimate cfPWV by 0.5–0.6 m/s relative to tonometric references and exhibit only moderate Bland–Altman agreement, supporting their use as population-level screening tools rather than individual diagnostic substitutes [148,149]. The pOpmètre (Axelife), a piezoelectric–photoelectric hybrid that estimates finger-to-toe

PWV from two optical sensors and a height-based path length, has shown moderate concordance with SphygmoCor ($R^2 \approx 0.43$) and intra-session CV of 4.5%, positioning it as a simplified primary-care tool [150].

Beyond cfPWV, brachial–ankle PWV (baPWV), measured with four-cuff oscillometric systems (Omron Colin, VaSera), is predominant in East Asian cardiovascular cohorts; the J-BAVEL individual-participant meta-analysis of 14,673 subjects has documented a hazard ratio of 3.50 for cardiovascular events in the highest versus lowest quintile [151,152]. The Cardio-Ankle Vascular Index (CAVI), derived on the VaSera platform by combining the Hayashi β stiffness parameter with the Bramwell–Hill formulation introduced in Section 2.1.3, was specifically engineered to be mathematically independent of the instantaneous blood pressure at which the measurement is taken [153,154]. Recent meta-analyses have confirmed its prognostic value for incident cardiovascular and renal outcomes [155], although methodological work has proposed the refined $CAVI_0$ formulation to address residual blood-pressure dependence [156].

At the local scale, ultrasound echo-tracking and ultrafast ultrasound imaging provide simultaneous estimates of carotid distensibility, Peterson's elastic modulus and β-stiffness, with age- and sex-specific reference values now available from cohorts of more than 1,800 healthy subjects [157]. At the imaging end of the spectrum, 4D-flow magnetic resonance imaging delivers global and regional aortic PWV with inter-observer coefficients of variation around 7%, but its cost and acquisition time confine it to research applications [158]. Pulse wave analysis (PWA), finally, derives the augmentation index (AIx) and the central aortic pressure waveform from radial tonometry through a generalised transfer function: AIx is a systemic descriptor of wave reflection rather than a pure stiffness marker, depends strongly on heart rate and provides prognostic information independent of cfPWV [159].

The heterogeneity of these methods, combined with the systematic biases observed across devices, has long undermined the cross-comparability of stiffness measurements obtained in different clinical settings. The 2024 VascAgeNet/ARTERY consensus on the validation of non-invasive PWV devices [140] explicitly addresses this issue by codifying study design, reference standards and acceptance limits, and represents the methodological framework against which any new technology, including the PPG-based approaches developed in this thesis, must now be evaluated.

3.1.2 PPG-Based Approaches

The PPG waveform encodes both timing and morphological information that, suitably extracted, mirrors the haemodynamic phenomena exploited by tonometric devices and motivates the use of PPG as a low-cost, miniaturisable surrogate for arterial stiffness assessment. Four methodological families have crystallised over the last two decades.

The first family is grounded on global descriptors of the digital volume pulse contour. Millasseau et al. [160] introduced the Stiffness Index (SI), defined as the ratio between subject height and the temporal delay (ΔT) between the systolic peak and the late-systolic/diastolic peak of the finger volume pulse, on the rationale that ΔT reflects the round-trip transit time of the pressure wave from the ascending aorta to the lower-body reflecting sites [161]. In 87 normotensive subjects, SI correlated with tonometric cfPWV ($r = 0.65$), tracked age and mean arterial pressure with comparable regression slopes and responded coherently to glyceryl-trinitrate challenge, although an independent multi-device comparison reported a more modest correlation ($r = 0.55$) and a bias of -1.12 ± 4.92 m/s against the dual-tonometer reference [160,162]. The complementary Reflection Index (RI), defined as the amplitude ratio between the diastolic and systolic peaks [163], quantifies the magnitude of wave reflection and has been shown to be modulated by endothelial and endothelium-independent vasodilators and to be blunted in type II diabetes [164]. The clinical relevance of these contour-based indices has been confirmed at population scale by the UK Biobank analysis of 169,613 participants, in which the Arterial Stiffness Index, a PulseTrace-derived variant of SI, independently predicted incident cardiovascular events and all-cause mortality [165].

The second family is based on transit-time estimates. Pulse arrival time (PAT) is computed from the ECG R-peak to the PPG foot at a single peripheral site and is contaminated by the pre-ejection period, which is itself modulated by sympathetic tone; PAT is therefore only an approximate surrogate of true arterial transit time [166,167]. Multi-site pulse transit time (PTT) configurations, derived between two PPG sensors placed at known distances along the arterial tree (typically finger–toe, ear–finger or forehead–toe), bypass the pre-ejection period and have been shown to discriminate atherosclerotic from healthy subjects in a substantial fraction of the parameters extracted [168,169]. Dedicated multi-channel PPG systems and head-to-toe configurations correlate strongly with SphygmoCor XCEL cfPWV and meet the Artery Society validation thresholds [170]. The in vitro results obtained as part of this doctoral project further confirm the feasibility of estimating pulse wave velocity (PWV) using a

pair of PPG sensors positioned on the surface of silicone phantom models with different mechanical properties to simulate different physiological conditions, operating within a controlled simulated circulatory circuit that reproduces the Moens-Korteweg relationship, a topic that will be explored in greater depth in Chapter 4.

The third family, single-site pulse contour analysis, exploits morphological features of the PPG waveform and of its derivatives. Beyond the SI/RI dichotomy [171], several timing- and area-based parameters have been investigated, including the crest time, the inflection-point area ratio (A_2/A_1, correlated with total peripheral resistance) and the composite IPAD index [128,172], which combines the inflection-point area with the d-peak of the second derivative and reaches $r = 0.56$ with chronological age, the highest reported among 24 indices systematically tested by Ahn [173]. Complexity-based descriptors such as multiscale entropy and Higuchi/Katz fractal dimensions have also been shown to correlate with blood pressure and to outperform heart rate variability as haemodynamic indicators [174,175]. The role of the second derivative itself, which provides the most extensively validated subset of single-site PPG indices, is treated separately in Section 3.1.3.

The fourth family is driven by machine learning and wearable deployment. Lasso regression and gradient-boosted tree models trained on finger or wrist PPG features have been reported to predict cfPWV with root-mean-square errors in the 0.5–0.75 m/s range, approaching the reproducibility limit of the reference devices [176]. Deep convolutional networks trained on raw PPG from large epidemiological cohorts yield a data-driven vascular age that independently predicts coronary events, heart failure and all-cause mortality over follow-up periods of up to ten years [177,178]. In parallel, the methodological frontier has shifted towards remote photoplethysmography (rPPG), in which the pulsatile signal is reconstructed from the RGB time series of a facial video captured by a standard smartphone or webcam, eliminating the need for any contact transducer [179]. The reliability of rPPG critically depends on the suppression of motion- and illumination-related artefacts, and recent work by Elgendi, Martinelli and Menon has identified the signal-to-noise ratio index (NSQI < 0.293) as the optimal single-feature quality metric, enabling low-complexity isolation of high-quality cardiac information directly on portable devices [180]. Taken together, the convergence of supervised feature extraction, deep-learning vascular-age regression and standardised quality screening is progressively closing the gap between traditional reference devices and ubiquitous, low-cost optical platforms.

3.1.3 Second Derivative of the PPG Signal for Vascular Assessment

The second derivative of the PPG signal, alternatively termed APG, SDPPG or SDPTG in the older Japanese literature, occupies a privileged position in the methodological landscape outlined above because, unlike timing-based methods, it directly exposes the inflection points of the arterial pressure wave and, unlike SI or RI, is largely independent of absolute amplitude calibration. The morphological structure of the APG (waves a, b, c, d, e), the dimensionless indices derived from it (b/a, c/a, d/a, e/a, AGI) and their physiological interpretation have been introduced in Section 2.3.4; the present section reviews the validation landscape that has cemented the APG's role as a surrogate of vascular ageing.

The seminal study by Takazawa et al. [124] remains the benchmark against which every subsequent investigation is framed. In the first part of their study, authors enrolled 39 patients in whom simultaneous ascending-aortic pressure and fingertip APG were recorded during pharmacological perturbation: intravenous angiotensin increased central blood pressure from 126/74 to 160/91 mmHg and drove d/a from -0.40 ± 0.13 to -0.62 ± 0.19, whereas sublingual nitroglycerin produced the opposite excursion to -0.25 ± 0.12 ($p < 0.001$), demonstrating that d/a tracks central pressure modulation in a physiologically predictable way. A complementary epidemiological investigation, conducted on 600 subjects evenly distributed across age decades, established the AGI as correlated with chronological age at $r = 0.80$ and significantly elevated in 126 subjects with diabetes, hypertension, hypercholesterolaemia or ischaemic heart disease relative to age-matched controls, providing a dual mechanistic-epidemiological foundation for APG-based vascular ageing assessment [124].

Cross-sectional cohorts have consistently confirmed the age-related drift of APG indices: b/a becomes progressively less negative (i.e. increases) with age, whereas c/a, d/a and e/a decrease, and the composite AGI rises. Among these studies, the Korean community study of 300 subjects has quantified these slopes (b/a $\approx +0.0045$ yr^{-1}; d/a ≈ -0.0062 yr^{-1}; AGI $\approx +0.0162$ yr^{-1}) and identified systematic sex differences, with women exhibiting higher b/a and AGI [181]. Otsuka's community study of 211 subjects reported correlations of b/a with the Framingham risk score up to $r = 0.54$ in women and negative correlations of d/a up to $r = -0.58$ [133]. Notably, the age-dependence inverts in children and adolescents, where b/a and AGI decrease with age up to about 20 years because vessel growth dominates over wall stiffening in that interval, underlining the composite physiological nature of these indices [182].

In hypertensive populations, APG indices behave as proxies for target-organ damage. Imanaga linked lower |b/a| to higher carotid intima–media thickness and to direct carotid distensibility, providing the first mechanistic bridge between APG and local wall mechanics [183]. In a study of 973 middle-aged men, Otsuka identified hypertension (OR 1.65), dyslipidaemia (OR 1.51) and impaired fasting glucose (OR 2.43) as independent determinants of elevated b/a, with hypertension as the strongest modifier of d/a (OR 3.44) [184]. Baek introduced a simplified (b−e)/a variant to address the frequent disappearance of the c and d waves in older subjects, improving robustness in elderly and hypertensive cohorts [185].

The decisive comparative benchmark against cfPWV was set by Bortolotto in 524 essential hypertensives, 140 of whom exhibited atherosclerotic vascular alterations [186]. While cfPWV discriminated atherosclerotic status across all ages, the APG-derived index retained discriminatory power only beyond the sixth decade, positioning APG as a complementary rather than substitutive index, a conclusion reinforced in the Ohasama cohort, where APG and baPWV captured information from partially distinct arterial beds [187]. The prognostic stature of APG was cemented by the longitudinal study of 4,373 Japanese women followed for a median of nine years, in which d/a emerged as an independent predictor of cardiovascular mortality after adjustment for classical risk factors and, unlike augmentation-index-based markers, retained age-informativeness in older women [134].

Recent methodological advances have increasingly shifted from manual fiducial-point identification to data-driven feature extraction. Elgendi's event-related thresholding algorithm improved a- and b-wave detection against nine fixed-threshold methods on 1,540 heat-stressed beats [188]; Dall'Olio demonstrated that a twelve-layer ResNet and a ridge-regression model based on only two hand-crafted features (the SDPPG a-wave amplitude and the time to reflected wave) both achieved AUC ≈ 0.95 for healthy-vascular-aging classification on smartphone PPG [189]; convolutional networks trained directly on the raw PPG waveform localise the systolic peak as the most informative region and outperform hand-crafted APG indices in predicting vascular age [190].

Together, these results consolidate the APG signal as one of the most robust and physiologically interpretable surrogates of vascular ageing accessible from a single PPG channel and set the methodological foundation for the experimental work presented in Chapters 5, 6 and 7 of this thesis.

3.2 Other Vascular and Cardiovascular Applications of PPG

The methodological landscape reviewed in Section 3.1 has crystallised around vascular ageing and arterial stiffness because these endpoints have driven the clinical translation of pulse-wave analysis over the past two decades. The same waveform, however, encodes haemodynamic information that goes well beyond wall mechanics, and a non-negligible body of work has progressively extended PPG to a broader set of cardiovascular outcomes. The applications outlined below are not intended as an exhaustive review, but rather as a concise overview of how the photoplethysmographic waveform, beyond its established role in pulse oximetry, encodes a richer set of haemodynamic features that have progressively been exploited across multiple downstream applications.

Established clinical applications of PPG, namely pulse oximetry, heart-rate monitoring, peripheral perfusion assessment and respiratory-rate estimation, have already been outlined in Section 2.2.6 and are not revisited here. More recent investigations have extended PPG-derived features to atrial fibrillation screening on wearable devices [191–193], cuffless blood-pressure estimation through pulse transit time and machine-learning regression on single-channel waveforms [194,195], autonomic-function assessment via pulse-rate variability [123,196], and the screening of valvular and structural heart conditions, where preliminary evidence has shown that PPG morphology can capture the haemodynamic signature of aortic stenosis and regurgitation at population scale [197,198].

Within this expanding spectrum, the monitoring of transcatheter heart valves (THV) represents a particularly relevant emerging application. The progressive extension of transcatheter aortic valve implantation (TAVI) to younger and lower-risk patients, together with the limited durability of bioprosthetic leaflets and the residual risk of subclinical leaflet thrombosis [199], has motivated the search for non-invasive, continuous monitoring strategies that may complement intermittent imaging-based follow-up. In this context, the initial in vitro results from this doctoral project have shown that a pair of PPG sensors positioned on the surface of a flexible aortic model containing a transcatheter device can determine the geometric area of the orifice using regression models and identify conditions of reduced leaflet mobility with high classification accuracy [200,201]; this complementary line of work, which extends the in vitro PPG methodology beyond vascular ageing, will be briefly revisited in Section 4.5.

Chapter 4 — In Vitro Study: Arterial Stiffness Estimation Using PPG Sensors

4.1 Introduction and Study Objectives

The state of the art reviewed in Chapter 3 has documented an extensive PPG-based research effort directed towards the indirect characterisation of arterial stiffness, which has consolidated around a relatively small set of waveform-derived surrogates: the Stiffness Index, the Reflection Index, the Augmentation Index, the timing-based pulse transit time and the morphological indices computed from the second derivative of the PPG signal. These quantities have been extensively validated against tonometric and oscillometric references and have shown clinically informative correlations with chronological age and with cardiovascular outcomes. None of them, however, returns the mechanical property of interest (Young's modulus E), and none allows a direct comparison with the gold-standard mechanical characterisation of the vessel wall, namely the uniaxial tensile test.

This methodological gap motivates the in vitro study presented in this chapter. The rationale rests on three considerations. Firstly, a direct estimate of E provides a transparent and physically interpretable indicator of vascular stiffness, free from the device-specific biases that affect surrogate indices. Secondly, the only feasible way to validate any PPG-based estimate of E against an independent mechanical reference is to operate in a controlled environment where the wall material can be sampled and tested ex situ, a condition that no in vivo experiment can satisfy. Thirdly, the very few studies that have attempted a direct E estimation from PPG, such as those of Fuiano et al. with LVDT sensors [202] and of Njoum and Kyriacou with the volumetric elastic modulus [203], have employed either a single phantom geometry or surrogate sensors, leaving open the question of whether a pair of conventional optical PPG sensors can recover E across a clinically relevant range of vessel mechanical and geometric properties.

Within this framework, the study presented in this chapter, originally published as Diana et al., Sensors 2025 [204], and previously introduced as a conference contribution [205], pursued three specific objectives:

(i) to demonstrate, on a custom-designed mock circulatory loop, that a pair of low-cost PPG sensors is capable of determining Young's modulus using the Moens–Korteweg equation, across four silicone phantom models with different geometric (radius, wall thickness) and

mechanical (E ranging from approximately 2 to 6 MPa) properties, selected to simulate different physiological and pathological conditions of blood vessels;

(ii) to identify the optimal inter-sensor distance for PTT estimation, by systematically comparing three distances (10, 15 and 20 cm) compatible with peripheral anatomical sites, such as the forearm;

(iii) to validate the PPG-derived estimates of E against the reference value obtained from uniaxial tensile testing of the same silicone material, using both standard error analysis and the Bland–Altman framework.

To the best of the author's knowledge, no previous study has combined these three elements (direct E estimation through Moens–Korteweg, multi-distance sensor placement, and tensile-test validation across multiple phantom geometries) in a single experimental design.

4.2 Experimental Setup Design

The experimental setup was designed to reproduce, under controlled and repeatable conditions, the haemodynamic environment in which a peripheral arterial segment operates, while preserving the optical and mechanical conditions required for reliable PPG acquisition. The architecture of the mock circulatory loop is shown schematically in Figure 4.1 and consists of six main components connected through silicone tubing and standard plastic connectors.

Pulsatile flow was generated by a pulsatile linear pump (P01-48×360F, LinMot, Spreitenbach, Switzerland), whose piston stroke and frequency were programmed via the LinMot Talk software (v6.7) to reproduce the systolic and diastolic phases of a representative cardiac cycle. The pump was set to a frequency of approximately 90 cycles per minute and a cardiac output of 5 L/min. Downstream of the pump, an adjustable compliance chamber, based on a spring-mounted piston, reproduced the Windkessel buffering of the central circulation. The instantaneous flow rate was monitored by an electromagnetic flowmeter (Optiflux 5300C, Krohne, Duisburg, Germany), and the systemic pressure was measured by a commercial pressure transducer (X5072 Druck, GE Measurement & Control, Italy) connected to the circuit immediately upstream of the silicone model. An adjustable valve placed at the outlet of the silicone phantom allowed the operator to modulate peripheral resistance and to maintain the cycle pressure within the target range of 70–120 mmHg, consistent with normal systolic–diastolic values.

The test segment was a replaceable, 50-cm-long cylindrical silicone phantom, available in four variants designed to span a clinically relevant range of mechanical and geometric

properties. The four phantoms differed in internal radius (4.0–8.0 mm) and wall thickness (1.0–2.0 mm), and their nominal Young's modulus, characterised by uniaxial tensile testing, as described in Section 4.3.3, ranged from approximately 2.1 MPa for the most compliant model up to 5.6 MPa for the stiffest one. This range was chosen to cover both healthy aortic-like values and the pathologically stiffened conditions, where an increase of up to 60% in the elastic modulus has been documented in the presence of vascular disease.

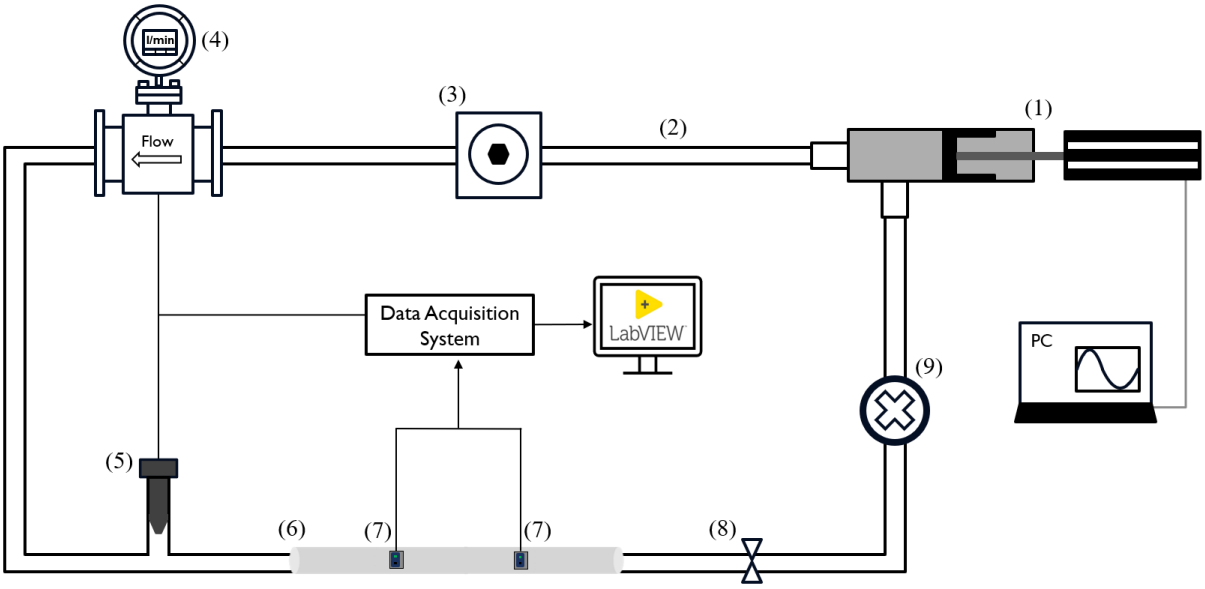

Figure 4.1 *Experimental setup scheme. The numbers reported refer to the following components: pulsatile pump (1), silicone tubes (2), compliance chamber (3), flowmeter (4), pressure transducer (5), silicon phantom model (6), PPG sensors (7), adjustable valve (8), fluid collector (9).*

Signals were acquired by a pair of PPG sensors operating at 520 nm (DFRobot, Beijing, China), the green wavelength most widely adopted in wearable devices for its favourable trade-off between superficial vascular sensitivity and motion robustness. The two sensors were tied around the silicone phantom by elastic bands ensuring a stable contact pressure throughout each test, and the inter-sensor distance, defined as the photodetector-to-photodetector separation, was set to one of three predefined values (10, 15 or 20 cm) measured with a caliper (Universal vernier models; TESA Technology, Switzerland). The selection of these three distances is discussed in Section 4.3.4.

The PPG signals, together with pressure and flow data, were acquired using a National Instruments USB-6009 data-acquisition board at a sampling frequency of 5 kHz and recorded in real time through a dedicated LabVIEW (v2021) acquisition pipeline. The fluid used for the experiments was distilled water, approximately 3 L stored in the fluid collector.

4.3 Methodology

The estimation of Young's modulus from the acquired PPG signals required the sequential application of three operations: extraction of the pulse transit time between the two PPG sensors (Section 4.3.1), conversion of PTT into pulse wave velocity and inversion of the Moens–Korteweg equation to obtain Young's modulus (Section 4.3.2), and validation of the optical estimates against an independent mechanical reference (Section 4.3.3).

Before any feature extraction, the raw PPG waveforms underwent a preprocessing step consisting of a fourth-order Butterworth bandpass IIR filter with passband 0.5–5 Hz, selected after a preliminary frequency-domain analysis aimed at preserving the fundamental harmonics of the pulse while suppressing both baseline drift and high-frequency electronic noise.

4.3.1 PTT Estimation: Peak-to-Peak and Tangent Methods

Two complementary approaches were implemented for the estimation of the pulse transit time between the upstream and downstream PPG sensors, and their relative performance was systematically compared. The peak-to-peak method identifies the maximum of each pulse on both signals through the standard findpeaks algorithm and computes PTT as the time difference between the corresponding fiducial points (Figure 4.2A). This approach is computationally efficient and easy to implement, and it represents the most common choice in the in vitro PPG literature [126]. The tangent method estimates PTT from the time difference between the points of maximum slope on the ascending limb of the two waveforms (Figure 4.2B). Operationally, the maxima of the first derivative of each filtered PPG signal are extracted with the same findpeaks routine, and the corresponding inflection points are taken as fiducial points. Although computationally more demanding, this method exploits a portion of the waveform that is intrinsically less affected by the superposition of forward and backward-travelling pressure waves and is therefore expected to be more robust under reflection-rich conditions (e.g. short inter-sensor distances or stiffer vessel walls).

Both methods were applied to all the experimental conditions investigated, and the choice of the most appropriate one for each combination of phantom model and inter-sensor distance was driven by the empirical performance reported in Section 4.4.

A third class of techniques, based on the cross-correlation between the two waveforms, was reported as a robust alternative by Filippi et al. [126] and is left as a methodological development for future work.

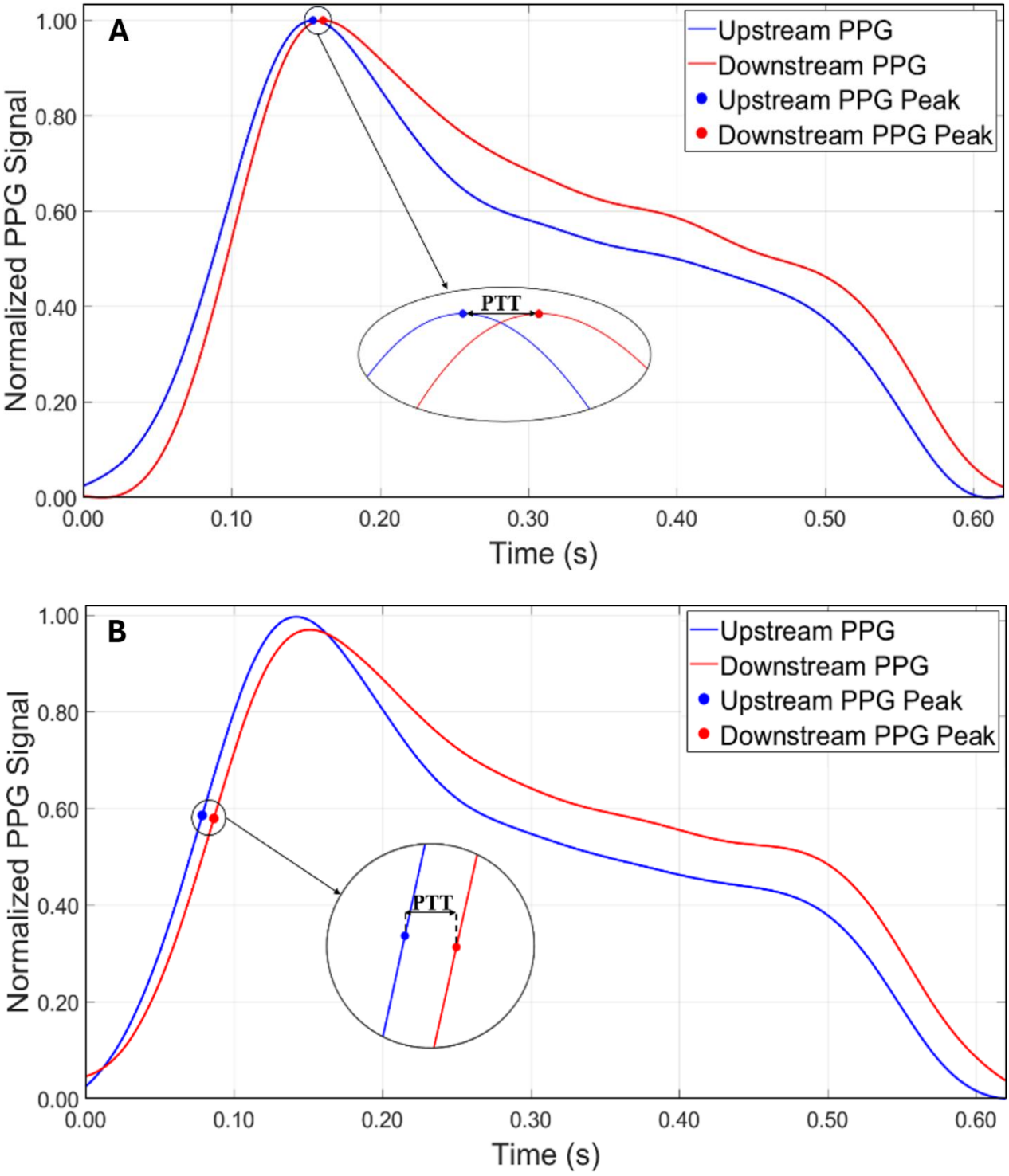

Figure 4.2 *Comparison between two approaches for calculating PTT. (A) Peak-to-peak method. (B) Tangent method.*

4.3.2 PWV and Young's Modulus Calculation

Once the pulse transit time has been estimated, the pulse wave velocity is obtained as the ratio between the inter-sensor distance and the PTT, according to Eq. (2.1), introduced in Section 2.1.3. Knowing the geometric parameters and the fluid density, it is possible to calculate the Young's modulus of the wall material by inverting the Moens-Korteweg equation (Eq. 2.2), which was presented in Section 2.1.3:

$$E = \left(\frac{2\,r\,\rho}{h}\right) PWV^2 \tag{4.1}$$

where r and h are the inner radius and wall thickness of the silicone phantom (measured ex situ for each model) and ρ is the density of the working fluid, taken as that of distilled water ($\rho \approx 1000$ kg/m^3). It is worth recalling that, as discussed in Section 2.1.3, the Moens–Korteweg equation is derived under simplifying assumptions (thin-walled, homogeneous, linearly elastic vessel; incompressible and non-viscous fluid; absence of wave reflections) which are well approximated by a cylindrical silicone phantom in a controlled mock loop, but are only partially satisfied in vivo. The validity of Eqs. (2.1) and (4.1) within the present in vitro setup is therefore considered methodologically sound and provides a defensible reference framework for the validation campaign described below.

To capture the natural beat-to-beat variability of the PWV estimates, the Young's modulus was not computed once per test but every 5 s within each 3-minute acquisition, yielding a distribution of values from which mean and standard deviation could be derived. For each combination of phantom model and inter-sensor distance, ten repeated acquisitions were collected, for a total of 120 tests across the experimental campaign.

4.3.3 Validation Through Tensile Testing

The reference Young's modulus of each silicone phantom was independently determined by uniaxial tensile testing on twelve specimens cut from the same batch of material used for the corresponding mock-loop model. Each specimen was firmly clamped between the grips of a tensile testing machine (Figure 4.3A), with care taken to ensure axial alignment and a uniform stress distribution within the gauge length. To enable an accurate, contactless measurement of the local strain field, two black markers were placed on each specimen at one-quarter and three-quarters of its length and tracked

through a high-definition camera (C910, Logitech) operating at 30 fps. The marker centroids were extracted in real time by a LabVIEW Vision Development Module routine adapted from Pasta et al. [206], based on a pixel-weighted pattern-matching procedure on monochromatic 380×240 frames.

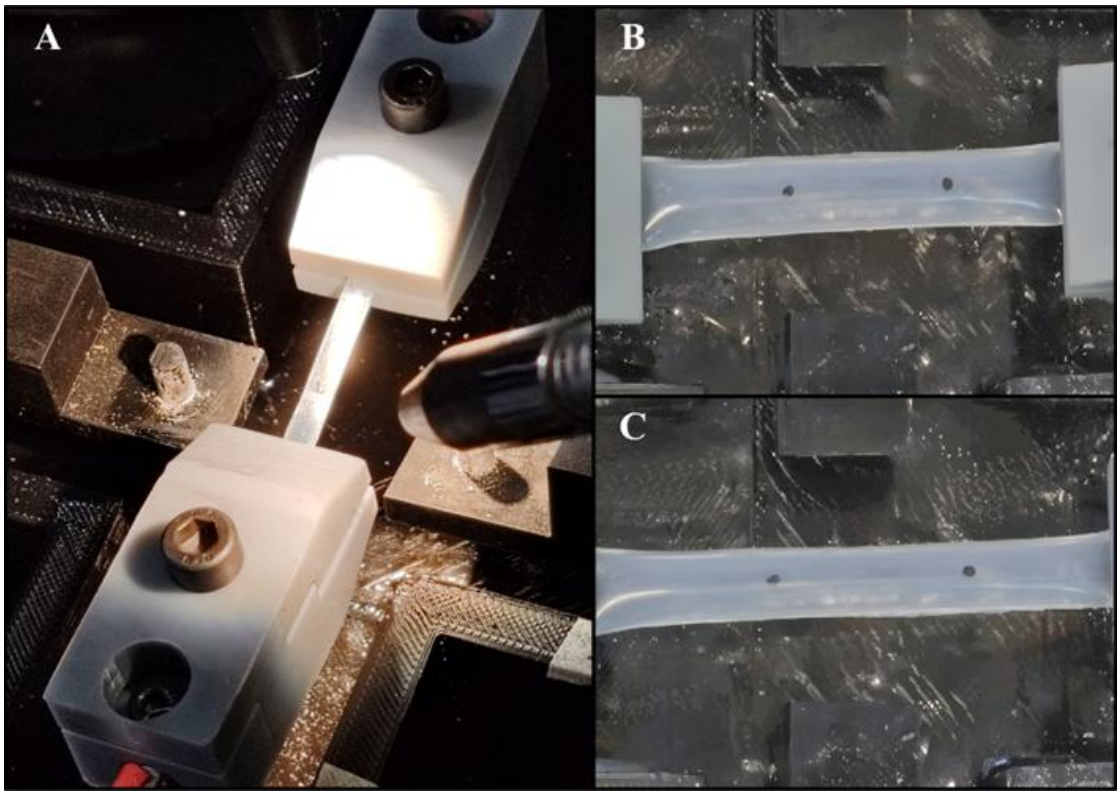

Figure 4.3 *Tensile test setup. (A) Universal tensile machine with mounted silicone specimen. (B) Specimen at rest with initial marker positions. (C) Specimen at the end of the test, showing marker displacement and elongation.*

Each test consisted in a controlled elongation of 20 mm at a crosshead speed of 2 mm/min. The recorded force signal was converted into engineering stress by dividing by the cross-sectional area of the specimen, while the engineering strain was computed from the relative displacement of the marker pair with respect to its initial separation. Stress–strain curves were generated and Young's modulus was extracted as the slope of the linear regression fit to the elastic region of the curve. The twelve modulus values obtained for each silicone model were averaged to yield the reference E used in the validation analyses of Section 4.4. The uncertainty of these reference values combines a Type A component (the standard deviation across the twelve specimens) and Type B components from the force measurement, specimen geometry, optical marker tracking and camera calibration, and the operator-dependent choice of the linear elastic region.

4.3.4 Analysis of the Influence of Sensor Distance

The inter-sensor distance enters the PWV estimation in two distinct ways. On one hand, it appears explicitly at the numerator of Eq. (2.1), so that for a given temporal resolution of the acquisition, longer distances translate proportionally larger PTT values, increasing the relative accuracy of the time-delay measurement. On the other hand, the propagation of the pulse wave along a longer segment is more affected by attenuation and by the superposition of forward and reflected waves, particularly in the presence of impedance mismatches at the boundaries of the test segment. Three placements were therefore investigated, namely 10, 15 and 20 cm, chosen to bracket the range of inter-sensor separations that can be physically realised on peripheral anatomical sites such as the forearm.

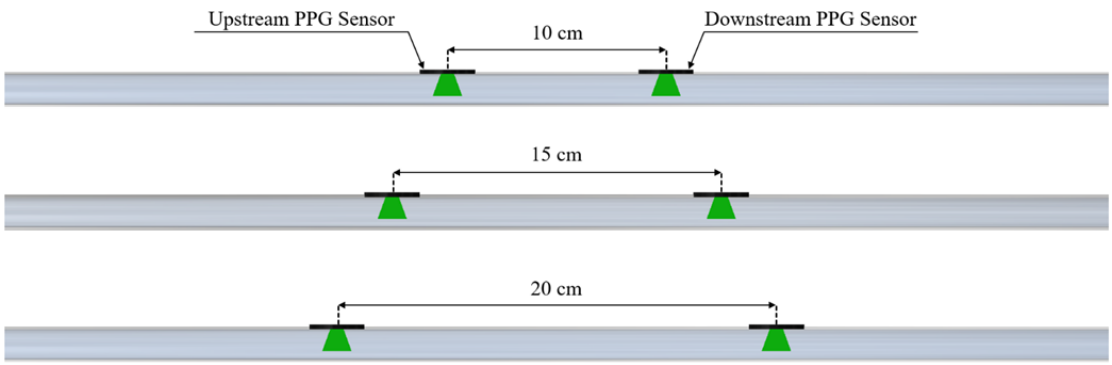

Figure 4.4 *Configurations of PPG sensors on the phantom model for PTT detection.*

This range constitutes a deliberate methodological compromise: distances shorter than 10 cm would compress the PTT into a few milliseconds, dominated by quantisation and noise, while distances longer than 20 cm would not be compatible with a single peripheral measurement segment in vivo. The systematic comparison of the three placements, combined with the two PTT estimation methods of Section 4.3.1, defines the parameter grid on which the experimental campaign was designed.

4.4 Results and Discussion

The experimental campaign produced one hundred and twenty individual tests, organised as a 4 × 3 × 10 factorial design (four silicone models, three inter-sensor distances, ten repeated acquisitions per condition). For each test, the Young's modulus distribution obtained from the 5-second windows was summarised by its mean and standard deviation, and the resulting estimates were compared against the tensile-test reference for the corresponding model. The results obtained with the peak-to-peak and tangent methods are reported in Table 4.1 and Table 4.2, respectively, alongside the geometric and reference mechanical parameters of each phantom.

Table 4.1 *— Geometric and mechanical properties of the four silicone phantoms (radius, wall thickness, tensile-test E ± SD) and Young's modulus values estimated from PPG sensors using the peak-to-peak method at 10, 15 and 20 cm.*

N.	Radius (mm)	Thickness (mm)	Tensile Test (MPa)	Experimental Value 10 cm (MPa)	Experimental Value 15 cm (MPa)	Experimental Value 20 cm (MPa)
1	4.30	1.30	2.10 ± 0.19	2.68 ± 0.83	2.04 ± 0.15	2.00 ± 0.19
2	7.50	1.50	2.70 ± 0.16	2.40 ± 0.72	2.63 ± 0.24	2.78 ± 0.28
3	4.00	1.00	4.00 ± 0.28	3.17 ± 0.51	4.04 ± 0.51	4.20 ± 0.58
4	8.00	2.00	5.65 ± 0.34	0.71 ± 0.65	5.74 ± 0.65	6.18 ± 0.82

Table 4.2 *— Same as Table 4.1, with PPG-derived E obtained through the tangent method.*

N.	Radius (mm)	Thickness (mm)	Tensile Test (MPa)	Experimental Value 10 cm (MPa)	Experimental Value 15 cm (MPa)	Experimental Value 20 cm (MPa)
1	4.30	1.30	2.10 ± 0.19	2.01 ± 0.23	2.27 ± 0.19	2.04 ± 0.27
2	7.50	1.50	2.70 ± 0.16	2.50 ± 0.53	2.96 ± 0.43	2.42 ± 0.48
3	4.00	1.00	4.00 ± 0.28	3.83 ± 0.81	4.24 ± 0.65	3.85 ± 0.79
4	8.00	2.00	5.65 ± 0.34	5.53 ± 0.87	6.14 ± 0.76	6.24 ± 0.86

A first qualitative observation, evident from both tables and from the corresponding error-bar plots in Figure 4.5 and Figure 4.6, concerns the standard deviation of the Young's modulus estimates: the dispersion of the PPG-derived values increases monotonically with the stiffness of the silicone model, regardless of the chosen PTT method or inter-sensor distance. A consistent trend was previously reported by Fuiano et al. [207] and was attributed to the viscoelastic behaviour of silicone, whose relaxation dynamics introduce

small beat-to-beat variations in the apparent wall mechanical response which are amplified in the PWV estimate through Eq. (4.1). The same physical mechanism explains the slight overestimation of E observed at 20 cm for the stiffest model (Model 4), where the propagation of the pulse over a longer segment of stiff material amplifies the contribution of high-frequency reflections.

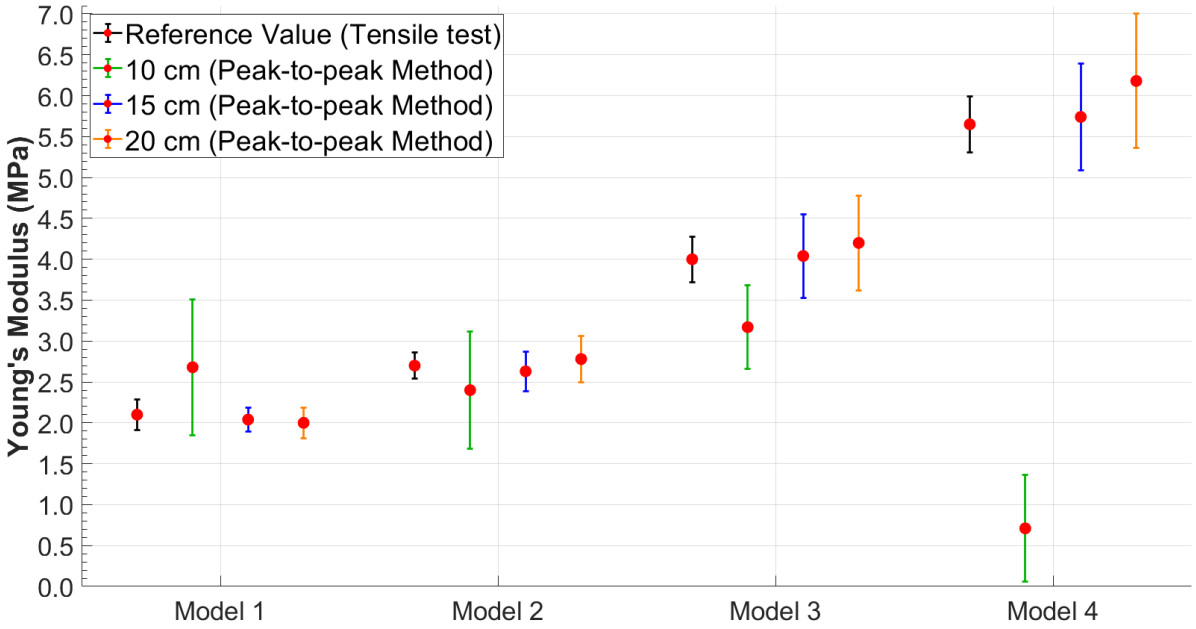

Figure 4.5 *Young's modulus estimates obtained with the peak-to-peak method, compared to the tensile-test reference (red), for the four phantom models at the three inter-sensor distances.*

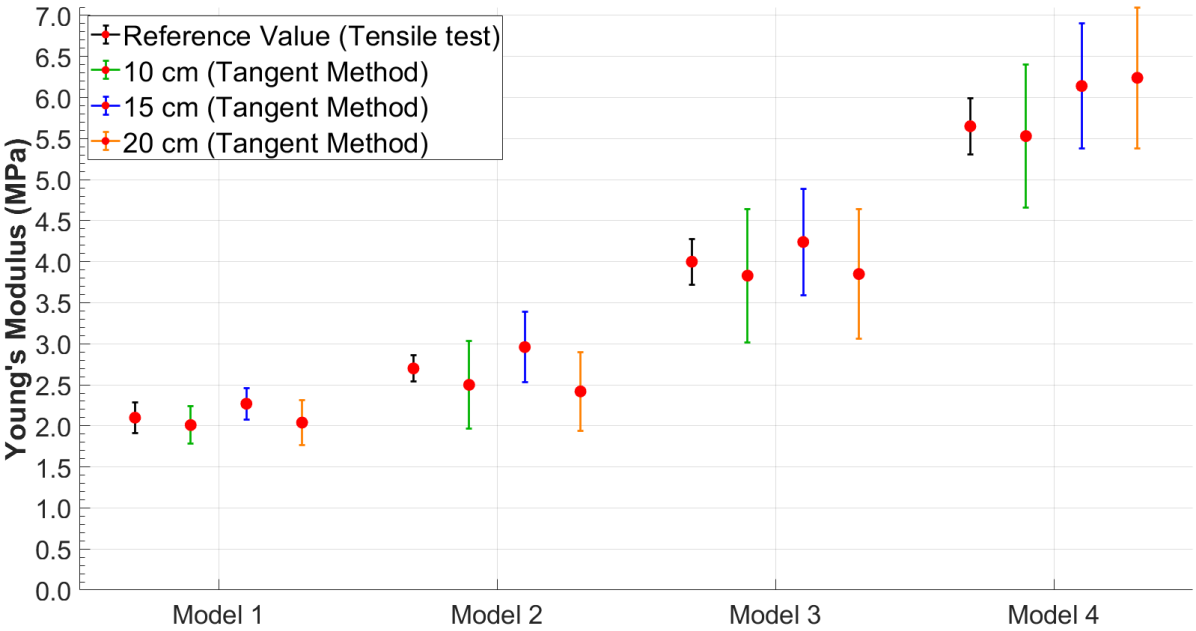

Figure 4.6 *Young's modulus estimates obtained with the tangent method, compared to the tensile-test reference (red), for the four phantom models at the three inter-sensor distances.*

The most distinctive methodological finding concerns the relative performance of the two PTT estimators as a function of the inter-sensor distance. At the shortest distance (10 cm), the peak-to-peak method produced systematically biased estimates, with average errors of approximately 20% across all phantoms and a marked underestimation for the stiffest model (Model 4 was estimated at 0.71 ± 0.65 MPa against a reference of 5.65 ± 0.34 MPa). The tangent method, in contrast, returned values closely matching the reference for every model at the same distance (e.g. 5.53 ± 0.87 MPa for Model 4). At the longer distances of 15 and 20 cm, both methods produced consistent and accurate estimates, but the peak-to-peak approach yielded slightly tighter distributions and lower bias. The most likely physical explanation lies in the wave-reflection content of the signals: the pulsatile linear pump used in the mock loop, although designed to mimic a continuous cardiac cycle, introduces residual backward pressure fluctuations through its valve action, and these reflections superimpose more strongly on the systolic peak when the inter-sensor distance is short. The tangent method, by anchoring the fiducial point on the maximum slope of the ascending limb (a portion of the waveform that has not yet been contaminated by the reflected component), is intrinsically more robust under these conditions, at the cost of a higher computational complexity. As a result, the analyses that follow combine the two estimators according to the best-performing one at each distance, namely the tangent method at 10 cm and the peak-to-peak method at 15 and 20 cm.

Adopting this best-method-per-distance combination, the agreement between the PPG-derived Young's modulus and the tensile-test reference was quantified through three complementary statistical analyses. The standard error of each PPG estimate, reported in Table 4.3, increased systematically from a minimum of 0.05 MPa for Model 1 at 15 cm to 0.28 MPa for Model 4 at 10 cm, confirming the growing measurement uncertainty associated with stiffer materials. The Pearson correlation coefficients between PPG-derived and tensile-derived values, summarised in Table 4.4, exceeded 0.95 for the two softer phantoms (Models 1 and 2) at all three distances, and remained consistently higher than 0.42 even for the stiffest model. The Bland–Altman analysis (Figure 4.7) confirmed both findings graphically, showing a tighter clustering of the differences around the bias line for the softer models and a progressively wider dispersion for the stiffer ones.

Table 4.3 *— PPG-derived Young's modulus values (mean ± standard error) for the four phantoms at the three inter-sensor distances.*

N. Model	10 cm (MPa)	15 cm (MPa)	20 cm (MPa)
1	2.01 ± 0.07	2.04 ± 0.05	2.00 ± 0.06
2	2.50 ± 0.17	2.63 ± 0.08	2.78 ± 0.09
3	3.83 ± 0.26	4.04 ± 0.16	4.20 ± 0.18
4	5.53 ± 0.28	5.74 ± 0.21	6.18 ± 0.26

Table 4.4 *— Pearson correlation coefficients between PPG-derived and tensile-test reference values.*

N. Model	10 cm	15 cm	20 cm
1	0.95	0.98	0.97
2	0.95	0.97	0.96
3	0.61	0.62	0.61
4	0.42	0.44	0.43

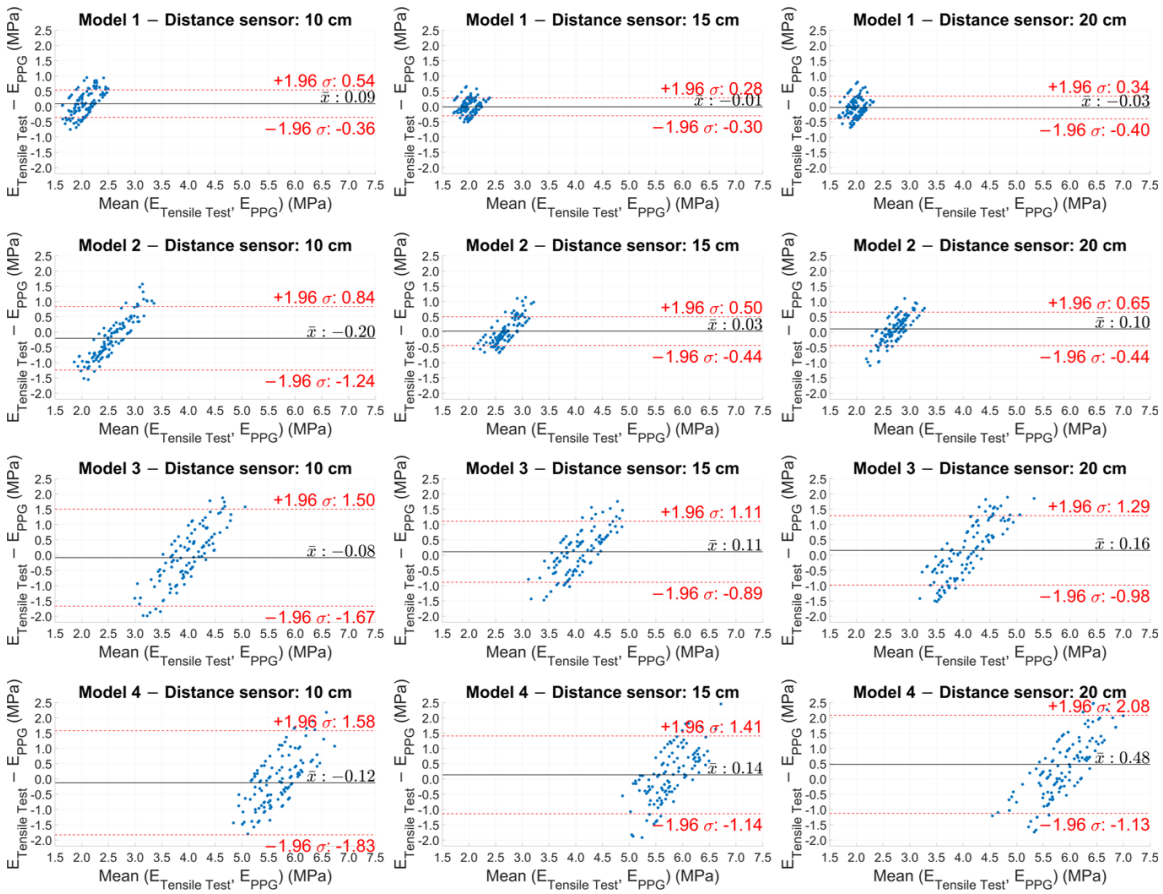

Figure 4.7 *Bland–Altman plots for the four phantoms at the three inter-sensor distances.*

The preceding analyses (standard deviation, standard error and Bland–Altman) describe the dispersion and agreement of the estimates, but do not constitute a formal uncertainty budget. The following analysis complements them by propagating the uncertainty on Young's modulus, distinguishing Type A components, evaluated statistically from the data (the beat-to-beat variability already reported in Tables 4.1–4.3), from Type B components, evaluated from instrument specifications and a priori considerations (the resolution of the geometric measurements, the fluid density, the sensor placement, and the temporal resolution associated with the sampling frequency and fiducial-point detection).

Starting from the measurement model of Eq. (4.1), and treating the input quantities as mutually uncorrelated, the relative combined uncertainty of the Young's modulus is obtained through the standard propagation law. Since E depends on the input quantities through a power-law relation, the relative sensitivity coefficient of each quantity coincides with its exponent in Eq. (4.1), yielding:

$$\left(\frac{u_E}{E}\right)^2 = \left(\frac{u_r}{r}\right)^2 + \left(\frac{u_\rho}{\rho}\right)^2 + \left(\frac{u_h}{h}\right)^2 + 4\left(\frac{u_{\Delta s}}{\Delta s}\right)^2 + 4\left(\frac{u_{\Delta t}}{\Delta t}\right)^2 \tag{4.2}$$

where u_r, u_ρ, u_h, $u_{\Delta s}$ and $u_{\Delta t}$ denote the standard uncertainties of the inner radius, fluid density, wall thickness, inter-sensor distance and pulse transit time, respectively. The factors of four affecting the Δs and Δt terms follow from the fact that both quantities enter Eq. (4.1) squared, so that their relative contribution to the combined uncertainty is doubled. As a consequence, the pulse transit time is expected to be the dominant contributor to the overall uncertainty, which is fully consistent with the experimental behaviour reported above: at the shortest inter-sensor distance the small Δt inflates the relative time-delay uncertainty, accounting for the greater robustness of the tangent method under short-distance, reflection-rich conditions.

Applying Eq. (4.2) to the optimal configuration (Model 1 at 15 cm), the Type B contributions are dominated by the temporal term (relative contribution of about 3.0 %, accounting for the finite sampling period at 5 kHz and for fiducial-point jitter), followed by the wall-thickness term (about 2.2 %), while the radius, distance and density terms remain below 1 %. Combined with the Type A contribution derived from the beat-to-beat dispersion reported in Table 4.3 (about 2.5 %), this yields a relative combined standard uncertainty of approximately 4.6 %, corresponding to $u_E \approx 0.09$ MPa and to an expanded uncertainty $U \approx 0.19$ MPa at a coverage factor $k = 2$. The resulting estimate, $E = 2.04 \pm$

0.19 MPa, is in close agreement with the tensile-test reference (2.10 ± 0.19 MPa), confirming that the optical estimate and the mechanical reference are metrologically compatible for the optimal configuration.

Taken together, these results identify 15 cm as the optimal inter-sensor distance within the investigated range, providing the best compromise between the temporal resolution required for an accurate PTT estimation and the suppression of reflection-related artefacts. The findings are consistent with the analogous in vitro investigation by Fuiano et al. [207], where the variability of LVDT-based stiffness estimates increased with the tensioning state of the rubber tube, and with the in silico work of Hong et al. [208], which reported a progressive decline in the correlation between PPG-derived stiffness indices and aortic Young's modulus among older subjects. The convergence of these three independent lines of evidence (in vitro PPG, in vitro LVDT, and in silico modelling) supports the interpretation that the loss of accuracy at high stiffness levels is an intrinsic property of waveform-based stiffness estimators, rather than a methodological limitation specific to the present setup.

Several limitations of the present study should nevertheless be acknowledged before extrapolating its conclusions to the in vivo setting. The silicone phantoms used here, although chosen to span a clinically relevant range of E values, do not reproduce the viscoelastic, anisotropic and tethered behaviour of real arterial walls; their internal radii and wall thicknesses are larger than the anatomical counterparts; and the working fluid is distilled water, whose density (~1000 kg/m³ versus ~1050–1060 kg/m³) and viscosity (~0.7 versus ~3–4 mPa·s at 37 °C) are lower than those of blood, with potential consequences both on the propagation of the pulse wave and on the optical interaction with the PPG sensors. In a real in vivo measurement, additional confounders would arise from skin pigmentation and subcutaneous fat thickness, from motion-related artefacts, and from the contribution of vascular tone and endothelial activity to the apparent wall stiffness. Within this clearly delineated scope, the proposed methodology provides a robust and physically interpretable framework for the in vitro characterisation of arterial-like phantoms and constitutes the experimental foundation on which the in vivo investigations of the following chapters are built.

4.5 Application Extension: Non-Invasive Monitoring of Transcatheter Heart Valves

As anticipated in Section 3.2, the same in vitro PPG methodology developed in this chapter for arterial stiffness estimation has been extended, within the present doctoral project, to a complementary application: the non-invasive monitoring of transcatheter heart valve (THV) function. Although outside the main scope of this thesis, this line of work is briefly summarised here, as it shares with Sections 4.2–4.4 the same mock-loop architecture, the same PPG sensors and the same PTT/PWV estimation framework and represents a natural transposition of the methodology to a different clinical question. The clinical motivation lies in the limited durability of bioprosthetic leaflets and the lack of continuous, low-cost surveillance tools to complement intermittent imaging-based follow-up. The two studies below explored whether the same PPG configuration, placed proximally and distally to a transcatheter device, could capture a haemodynamic signature of valve performance and discriminate healthy from reduced leaflet motion.

In a first proof-of-concept study presented at the ADM 2024 conference [200], a fluid–structure interaction (FSI) analysis was used to virtually deploy a 23-mm SAPIEN 3 Ultra device in an idealised aortic vessel, and the resulting flow field was then used to derive an analytical estimate of PWV and PTT through a Bramwell–Hill formulation, as a function of the transvalvular pressure gradient. The numerical predictions were compared with experimental PPG measurements acquired on a 3D-printed flexible aortic phantom housing the same device, using the pair of PPG sensors described in Section 4.2 placed at a distance of 70 mm. The agreement between numerical and experimental data was relevant, with a relative error of 7.7% on PTT, supporting the placement of two PPG sensors for assessing the transvalvular pressure gradient.

Building on this preliminary evidence, a more comprehensive study was subsequently published in *Artificial Organs* [201]. A 23-mm self-expandable Evolut FX device (Medtronic) was deployed in a compliant aortic phantom within the mock loop, with two PPG sensors attached to the phantom surface in the ascending and descending aorta. Forty haemodynamic scenarios were generated through Latin Hypercube Sampling on the four flow variables (stroke volume, heart rate, systolic and diastolic pressure), and an endoscopic camera was used to measure the geometric orifice area (GOA) of the device at the systolic peak as the ground-truth indicator of valve performance. Representative PPG waveforms and corresponding GOA images for three hypotensive, normal and hypertensive scenarios are shown in Figures 4.8 and 4.9.

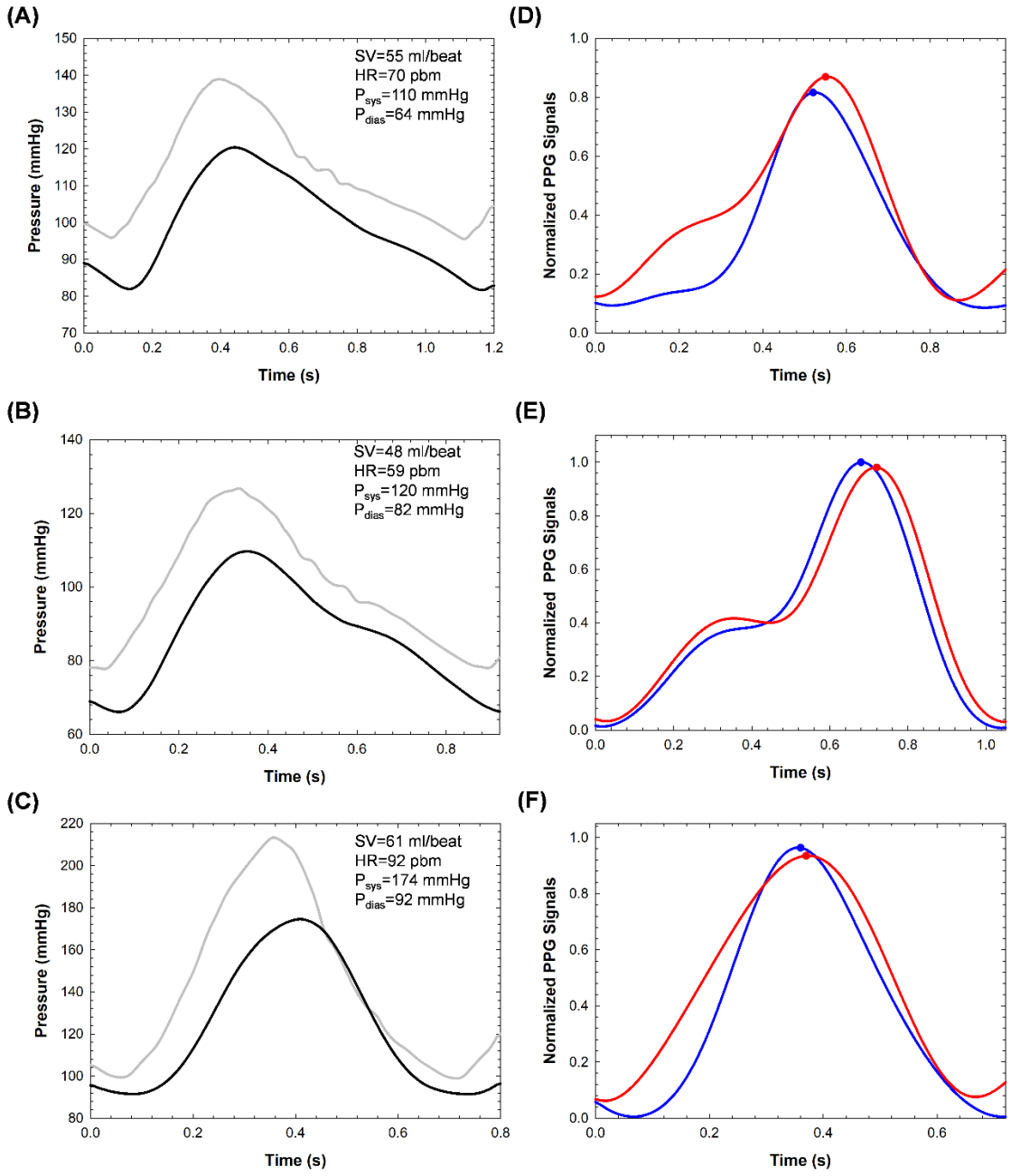

Figure 4.8 *Representative PPG waveforms acquired in the ascending (red) and descending (blue) aorta of the phantom housing the Evolut FX device, for three haemodynamic scenarios: hypotensive (top), normal (middle) and hypertensive (bottom).*

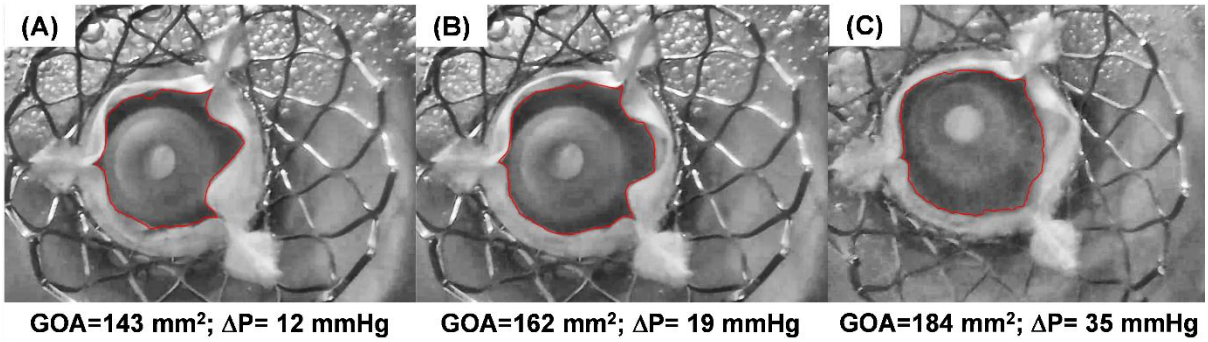

Figure 4.9 *Endoscopic images of the Evolut FX leaflet opening with the geometric orifice area (red contour) for the three corresponding scenarios: (A) hypotensive; (B) normal; (C) hypertensive.*

The PPG-derived metrics (PTT and PWV), together with the four flow variables, were used as input features to train a polynomial regression model for the prediction of GOA, and a threshold-based classifier for the discrimination between healthy (HLM) and reduced (RLM) leaflet motion conditions. The regression model achieved an R^2 of 0.83 (RMSE = 7.18 mm^2, MAE = 5.58 mm^2), and the classifier reached a 95% accuracy with a precision of 0.89 and a recall of 0.91, supporting the feasibility of an indirect, non-invasive estimation of leaflet performance through low-cost surface PPG sensors combined with machine-learning analysis.

Taken together, these two studies confirm that the in vitro PPG methodology developed in this chapter for the estimation of arterial stiffness can be coherently extended to the functional monitoring of transcatheter devices and represent a complementary application of PPG that opens promising research directions for the long-term, wearable-based surveillance of THV performance.

Chapter 5 — Analysis of the APG Signal as an Indicator of Vascular Aging

5.1 Introduction and Objectives

The in vitro work presented in Chapter 4 demonstrated that a pair of PPG sensors deployed along a vessel-like phantom can recover the Young's modulus of the wall material, providing a direct, physically interpretable estimate of arterial stiffness through the Moens–Korteweg equation. That method, however, requires the simultaneous acquisition of two PPG signals synchronized at a known distance between the sensors, as well as knowledge of the vessel's geometric and fluid dynamic parameters, conditions that are not easily met in a single-channel peripheral measurement taken at a single anatomical site.

The complementary methodological line developed within this thesis, and presented in this chapter, follows therefore the second major route to PPG-based vascular assessment reviewed in Chapter 3: the analysis of the second derivative of the PPG signal (APG), and in particular of the dimensionless ratios derived from its five characteristic deflections *a, b, c, d, e*, as introduced and formalised in Section 2.3.4. Among these ratios, the *d/a* index occupies a central position, being one of the most widely validated APG-derived markers of vascular aging and arterial stiffness in the clinical literature reviewed in Section 3.1.3, from the seminal work of Takazawa et al. [124] to the longitudinal evidence of Inoue et al. [134] on cardiovascular mortality.

Despite this consolidated background, the validation of the *d/a* ratio against the mechanical properties of the vessel wall has so far been addressed mainly in human cohorts, where wall stiffness is inferred indirectly. A complementary in vitro assessment, in which the underlying mechanical condition is fully controlled, can usefully reinforce the physiological interpretation of the parameter. This was the rationale of the present study, which combines an in vitro and an in vivo arm within a single methodological framework, providing the experimental foundation on which the subsequent investigations of Chapters 6 and 7 are built.

Within this framework, the study presented in this chapter, originally published as Diana et al., *Engineering Proceedings* 2025 [209], pursued three specific objectives:

(i) to evaluate, on the same in vitro mock circulatory loop adopted in Chapter 4, the relationship between the *d/a* ratio derived from a single PPG sensor and the mechanical

stiffness of two silicone phantom models with different Young's moduli, representative of physiological and pathologically stiffened vascular conditions;

(ii) to verify, on a small cohort of healthy volunteers spanning the adult age range, whether the same *d/a* ratio, computed at the index finger, exhibits the negative correlation with chronological age expected from the literature on arterial stiffness and vascular aging;

(iii) to compare the in vitro and in vivo trends within a unified analytical framework, in order to consolidate the role of the *d/a* ratio as a single-channel, low-cost surrogate of vascular health that can be deployed on wearable PPG devices.

Together, these three objectives define the dual experimental approach that distinguishes the present contribution from previous studies, in which the *d/a* ratio has been investigated either on phantom models or on humans, but not within an integrated mechanical–physiological design.

5.2 Methodology

Photoplethysmographic signals were acquired with a single PPG sensor (DFRobot, Beijing, China) operating at 520 nm, connected to an NI USB-6009 acquisition board (National Instruments, Austin, TX, USA) at a sampling rate of 5 kHz, and recorded through a dedicated LabVIEW (v2021) acquisition pipeline. The optical configuration is therefore identical to that adopted in Chapter 4, except for the use of a single sensor.

For the in vitro arm of the study, two flexible silicone phantom models of length 50 cm and inner radius 8 mm were used, characterised by Young's moduli of 2.7 MPa (Model 1) and 5.65 MPa (Model 2), respectively. The two models were chosen to represent a physiological vascular condition and a pathological condition with increased stiffness, consistently with the range introduced in Section 2.1.2 and adopted in Chapter 4. The PPG sensor was placed at the midpoint of each model. The phantom models were integrated within the same mock circulatory loop described in Section 4.2, configured to a flow rate of 5 L/min, a heart rate of 90 bpm, and a systemic pressure between 70 and 120 mmHg, with distilled water as the working fluid. For each model, five acquisitions of three minutes each were collected; the average *d/a* ratio was computed over one-minute intervals, yielding a total of 15 samples per model used in the subsequent statistical comparison.

For the in vivo arm of the study, nine healthy volunteers (six males and three females, age 42.1 ± 15.2 years, range 26–63 years) with no known cardiovascular disease were enrolled.

For each participant, three acquisitions of three minutes each were performed by placing the PPG sensor on the index finger; the average *d/a* ratio was similarly computed over one-minute intervals. In the absence of a direct measurement of arterial stiffness for each subject, the *d/a* ratio was related to the chronological age of the participants, on the basis of the well-established association between increasing age and increasing vascular stiffness already discussed in Section 2.1.3.

Data processing was performed in MATLAB (v2024b, The MathWorks Inc., Natick, MA, USA) and followed the same general scheme adopted throughout this thesis. The raw PPG signals were filtered with a fourth-order Butterworth bandpass IIR filter (passband 0.5–5 Hz) to remove baseline drift and high-frequency noise. The second derivative of the filtered signal was then computed and the five fiducial points *a, b, c, d, e* were automatically identified through MATLAB's *findpeaks* function applied within time windows consistent with the cardiac cycle, as discussed in Section 2.3.4. The *d/a* amplitude ratio was finally extracted and used as the index of arterial stiffness for both arms of the study. The use of repeated acquisitions and segment-wise averaging of the d/a ratio provided an implicit check on the repeatability of the APG fiducial-point extraction, whose systematic metrological characterisation is left to future developments.

5.3 Results and Discussion

The two arms of the study yielded internally consistent evidence of a strong negative correlation between the *d/a* ratio and the underlying vascular stiffness condition, as detailed in the following two sub-sections.

5.3.1 In Vitro Results

In the in vitro arm, the more compliant phantom (Model 1, E = 2.7 MPa) yielded a mean *d/a* ratio of 0.277 ± 0.036, while the stiffer phantom (Model 2, E = 5.65 MPa) yielded a mean value of 0.183 ± 0.036. Linear regression analysis returned a Pearson correlation coefficient of R = −0.81 between the model stiffness and the *d/a* ratio (Figure 5.1), confirming a strong negative correlation in line with the physiological interpretation of the parameter discussed in Section 3.1.3.

A first observation specific to the in vitro setting concerns the absolute sign of the *d/a* ratio: in both phantom conditions, the values remained positive, in apparent contrast with the negative range typically reported in human measurements. This behaviour can be ascribed to the simplified nature of the model, namely the absence of vascular tone,

branching and energy-dissipative mechanisms, which causes the reflected wave to arrive at a phase of the cycle in which the second derivative is still positive. In addition, the use of distilled water, whose viscosity is approximately one fifth of that of blood, reduces wave attenuation and preserves the relative amplitude of the *d* deflection. Consequently, the increase in stiffness from Model 1 to Model 2 produces a clearly detectable reduction of the *d/a* ratio, but does not bring it into the negative range observed in vivo. The relevance of this finding lies not in the absolute value but in the systematic, monotonic decrease of *d/a* with increasing wall stiffness, which establishes the mechanical interpretability of the index in a controlled environment.

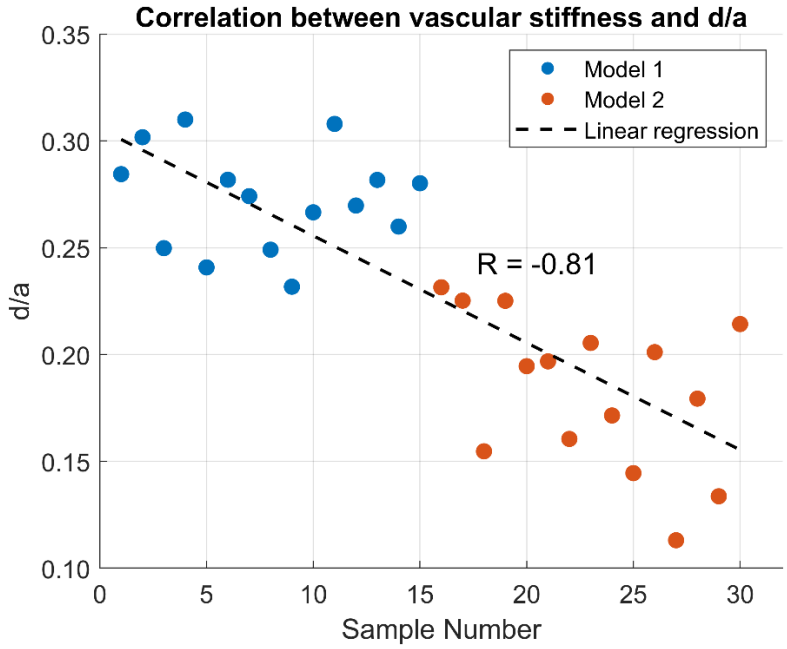

Figure 5.1 *Correlation between vascular stiffness and d/a ratio in the two silicone phantom models. Blue dots: physiological condition (Model 1, E = 2.7 MPa); orange dots: pathological condition (Model 2, E = 5.65 MPa). Dashed line: linear regression.*

5.3.2 In Vivo Results

In the in vivo arm, the *d/a* ratio of the nine healthy volunteers ranged from −0.120 to −0.410 across the 26–63-year age interval. Linear regression analysis (Figure 5.2) yielded a Pearson correlation coefficient of R = −0.90 between age and *d/a*, confirming a strong negative correlation: younger participants exhibited higher *d/a* values, while in older subjects the ratio was progressively reduced. This trend is consistent with the age-related increase in arterial stiffness widely documented in the literature [210,211], which modifies the propagation velocity and the reflection characteristics of the

pressure wave, and therefore the morphology of the PPG signal and of its second derivative.

The numerical values obtained in the present study are consistent with those reported in the literature on similar populations. Inoue et al. [134], in a long-term cohort of women aged 50–79 years, observed the same negative correlation between *d/a* and chronological age, with mean values closely overlapping those measured here in the upper age range. Takazawa et al. [124], in their seminal investigation on 39 patients (mean age 54 ± 11 years), reported the same trend, supporting the robustness of the inverse association between *d/a* and arterial stiffness.

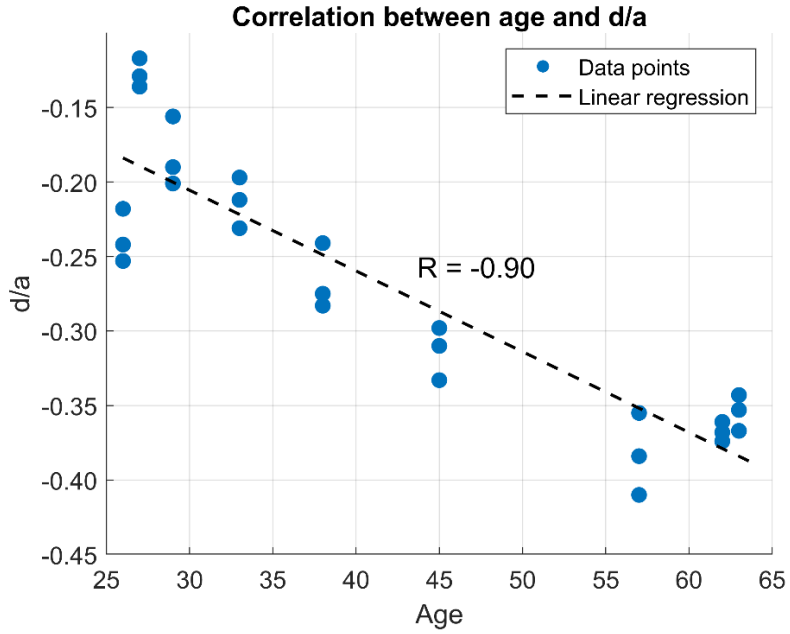

Figure 5.2 *Correlation between chronological age and d/a ratio in the nine healthy volunteers of the in vivo study. Dashed line: linear regression.*

Taken together, the in vitro and in vivo results converge on a coherent picture: the *d/a* ratio decreases monotonically with increasing wall stiffness in a controlled mechanical environment and decreases monotonically with chronological age in a human cohort spanning the third to seventh decade of life. This convergence consolidates the role of the *d/a* ratio as a low-cost, single-channel, single-site optical biomarker of vascular aging. As this APG-based approach had not yet been extensively validated against controlled mechanical conditions, the present study was conceived as a proof of concept on a small cohort, providing the experimental foundation for the broader investigations of Chapters 6 and 7.

5.4 Brief Note: Machine Learning for Vascular Age Classification from APG

The same nine-subject in vivo dataset described above was subsequently re-analysed within a dedicated machine-learning pipeline, in collaboration with the Biomedical and Mobile Health Technology Lab of ETH Zürich, where part of the present doctoral activity was carried out. The study, presented at the CIEES 2025 conference [212], explored whether classical and modern machine-learning models could leverage the five APG deflection peaks (*a, b, c, d, e*), the *b/a* and *d/a* ratios, or their combination, to discriminate younger from older participants in a binary classification task. On unseen subjects, the best-performing models reached a balanced accuracy of 0.89 and an AUC of 0.95 when the combined feature set was used (TabPFN), with the *d/a* ratio confirmed as one of the most informative features. These results are reported here only as a complementary methodological direction supporting the analytical framework of this chapter, and the reader is referred to the original publication for the full description of the dataset, the model selection procedure and the cross-validation strategies adopted.

Chapter 6 — Multi-Wavelength PPG Comparison for Vascular Aging Assessment

6.1 Introduction and Objectives

The investigation presented in Chapter 5 demonstrated, on a small in vivo cohort, that the *d/a* ratio extracted from a single fingertip PPG sensor at 520 nm exhibits a robust negative correlation with chronological age, in line with the validation framework reviewed in Section 3.1.3. That study was nevertheless deliberately limited in scope, both in terms of sample size (nine subjects) and in terms of optical configuration (a single green wavelength on a single anatomical site). Two methodological aspects, both of which are critical for the deployment of APG-based vascular aging assessment in real wearable devices, remained therefore open: the systematic comparison of different wavelengths and the systematic comparison of different anatomical measurement sites for APG analysis.

On the wavelength axis, the choice of the optical source determines the depth of light penetration in the tissue and, consequently, the vascular bed actually probed by the PPG sensor, as discussed in Section 2.2.4. Wavelengths in the green-blue range predominantly interrogate the arterioles of the superficial dermal vascular plexus, whereas the red and infrared ranges reach the subcutaneous level and a more heterogeneous mix of pulsatile and non-pulsatile contributions. Although this physical mechanism is well established, the literature on APG-derived vascular aging indices has been historically dominated by single-wavelength studies, mostly performed in the green or red range, and a systematic comparative assessment is still missing.

On the anatomical axis, the index finger is the traditional measurement site adopted in clinical research and in the foundational APG studies reviewed in Section 3.1.3, owing to its dense terminal vascular network and to the favourable signal-to-noise regime that it offers. The wrist, on the other hand, is the dominant site of consumer-grade wearable devices, including smartwatches, smartbands and smart rings, despite the deeper position of the radial and ulnar arteries beneath multiple tissue layers, which is known to attenuate the pulsatile component and to introduce greater morphological variability in the PPG waveform. Whether and to what extent the wrist can replace the finger as a viable acquisition site for APG-based vascular aging assessment is therefore a question of direct translational relevance for the wearable industry.

Within this framework, the study presented in this chapter, actually submitted as Diana et al., *IEEE Access* 2026, pursued three specific objectives:

(i) to design and develop a custom wearable multi-wavelength PPG prototype, capable of simultaneously acquiring PPG signals from the wrist and the index finger at four different wavelengths (blue, green, red, infrared);

(ii) to acquire and analyse, on a cohort of 44 healthy volunteers spanning the entire adult age range (22–94 years), the four APG-derived vascular aging indices that are robustly identifiable across wavelengths and sites, and to evaluate their correlation with chronological age;

(iii) to identify the optimal wavelength–site combination for non-invasive vascular aging assessment in wearable devices, balancing physiological interpretability, signal quality and applicability to real-world wrist-based monitoring.

Together, these objectives extend the analytical framework developed in Chapter 5 from a single-wavelength, single-site, single-derivative analysis to a comprehensive multi-wavelength, multi-site investigation, conducted on a substantially larger cohort and with a custom-built wearable platform purposely designed for the experimental campaign.

6.2 Development of the Multi-Wavelength Wearable Prototype

The experimental campaign required a hardware platform capable of simultaneously acquiring PPG signals at multiple wavelengths from two anatomical sites, with a temporal resolution sufficient to preserve the morphology of the second-derivative waveform. Since no commercial device meeting these requirements was available at the time of the study, a dedicated wearable prototype, named *Gianner*, was designed and built in collaboration with the Biomedical and Mobile Health Technology Lab of ETH Zürich, where the data acquisition was conducted. The general architecture of the device is shown schematically in Figure 6.1.

The system is articulated in two units. The wrist unit hosts the central microcontroller (ESP32-S3 Nano, Waveshare, Shenzhen, China) together with one PPG sensor and one NTC thermistor (B57703M0502G040, EPCOS/TDK Electronics, Munich, Germany) for skin temperature monitoring. The finger unit replicates the same optical and thermal architecture without the microcontroller.

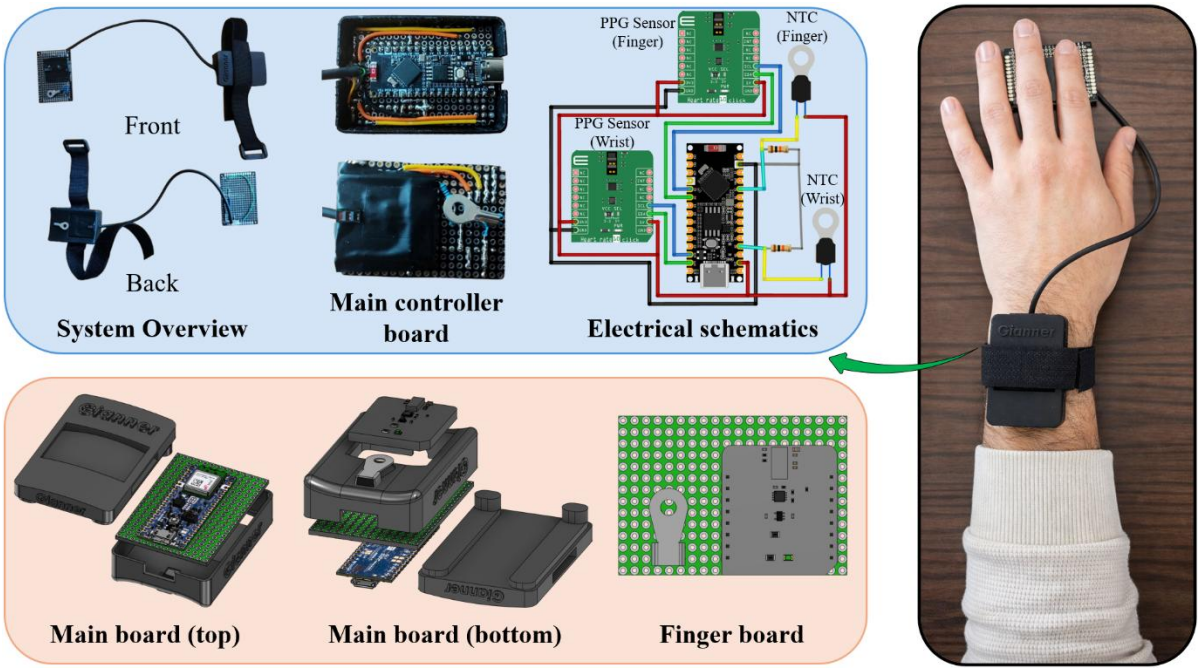

Figure 6.1 *Overview of the Gianner multi-wavelength PPG acquisition system. Top: views of the wearable system and electrical diagram of the dual-channel architecture; bottom: views of the 3D-printed custom enclosures for the main board and the finger sensor board.*

Both PPG sensors share an identical layout, based on the Heart Rate 10 Click optical sensor (MikroElektronika, Belgrade, Serbia), which integrates the MAX86916 optical front-end (Analog Devices, Wilmington, MA, USA) and features four LED sources at blue (455 nm), green (520 nm), red (655 nm) and infrared (930 nm), together with a single photodetector and integrated signal-conditioning electronics. The thermistors are connected to analogue inputs of the microcontroller through a 10 kΩ ± 5 % voltage divider; the entire system is supplied by a single 3.3 V rail with a common ground.

To preserve the temporal resolution required for the subsequent extraction of fiducial points on the second derivative of the PPG signal, the sampling frequency was set to 800 Hz. This is well above the values typically adopted in the wearable literature and was chosen as a deliberate methodological compromise, given the average wrist-to-fingertip distance of 19.4 ± 1.0 cm measured across the participants enrolled in the study and the fast morphological transitions characterising the APG waveform.

The electronic components were soldered onto two prototyping boards to ensure mechanical and electrical stability, and were then housed within two custom-designed enclosures, modelled in SolidWorks (Dassault Systèmes, Waltham, MA, USA) and printed using a Formlabs Form 4 system with BioMed Black resin (Formlabs Inc., Somerville, MA, USA), to guarantee biocompatibility for prolonged skin contact during the acquisitions.

6.3 Experimental Protocol

The experimental campaign was conducted at the Balgrist Campus of ETH Zürich (Switzerland), under a protocol approved by the ETH Zurich Ethics Committee (project 25 ETHICS-205, *Validation of a Multi-Wavelength Wearable PPG Device under Controlled Conditions*). All participants provided written informed consent prior to the start of the acquisitions. A total of 44 volunteers (29 men, 15 women), aged between 22 and 94 years (mean 43.5 ± 19.6 years), were enrolled. The cohort was deliberately designed to span the entire adult age range, in order to expose any age-dependent trend of the APG indices over a sufficiently wide temporal interval.

Acquisitions were performed under resting conditions in a temperature-controlled room maintained at approximately 20 °C. Each participant was seated with the left arm resting on a table; a five-minute acclimatisation period was observed before each session, during which the subject was asked to remain still and relaxed in order to ensure thermal and circulatory steady state. PPG signals were then acquired simultaneously from the wrist and from the index finger of the same hand for five continuous minutes, while the participant remained still and silent to minimise motion artefacts.

Signal processing followed the same pipeline established in Section 2.3.1. Each of the eight acquired channels (four wavelengths × two sites, per subject) was filtered with a fourth-order Chebyshev Type II bandpass filter, with a passband 0.5–8 Hz and a 20 dB stopband attenuation, chosen for its capability to preserve the morphological components of the PPG signal, including the dicrotic notch, while suppressing baseline drift and high-frequency electronic noise [91]. The acceleration plethysmogram (APG) was then computed by applying two successive numerical differentiations to the filtered signal, and the five characteristic deflections *a, b, c, d, e* were identified for each cardiac cycle.

A preliminary inspection of the dataset revealed that, across all wavelengths and at both measurement sites, the *a, b* and *e* waves were always clearly identifiable on the APG waveform, while the *c* and *d* waves did not exhibit prominent local maxima and minima between the *b* and *e* deflections. This morphological pattern corresponds to *Case I* of the multi-derivative classification proposed by Abdullah et al. [130]. Following the same authors, the *c* and *d* waves were therefore identified through the joint analysis of the first derivative (velocity plethysmogram, VPG) and the third derivative (jerk plethysmogram, JPG): wave *a* was located at the global maximum of the APG within each cycle, corresponding to the first zero-crossing of the JPG; wave *b* at the global minimum of the

APG and the second zero-crossing of the JPG; wave *c* at the global maximum of the JPG; wave *d* at the first local minimum of the VPG; and wave *e* at the second positive maximum of the APG and the third zero-crossing of the JPG (Figure 6.2).

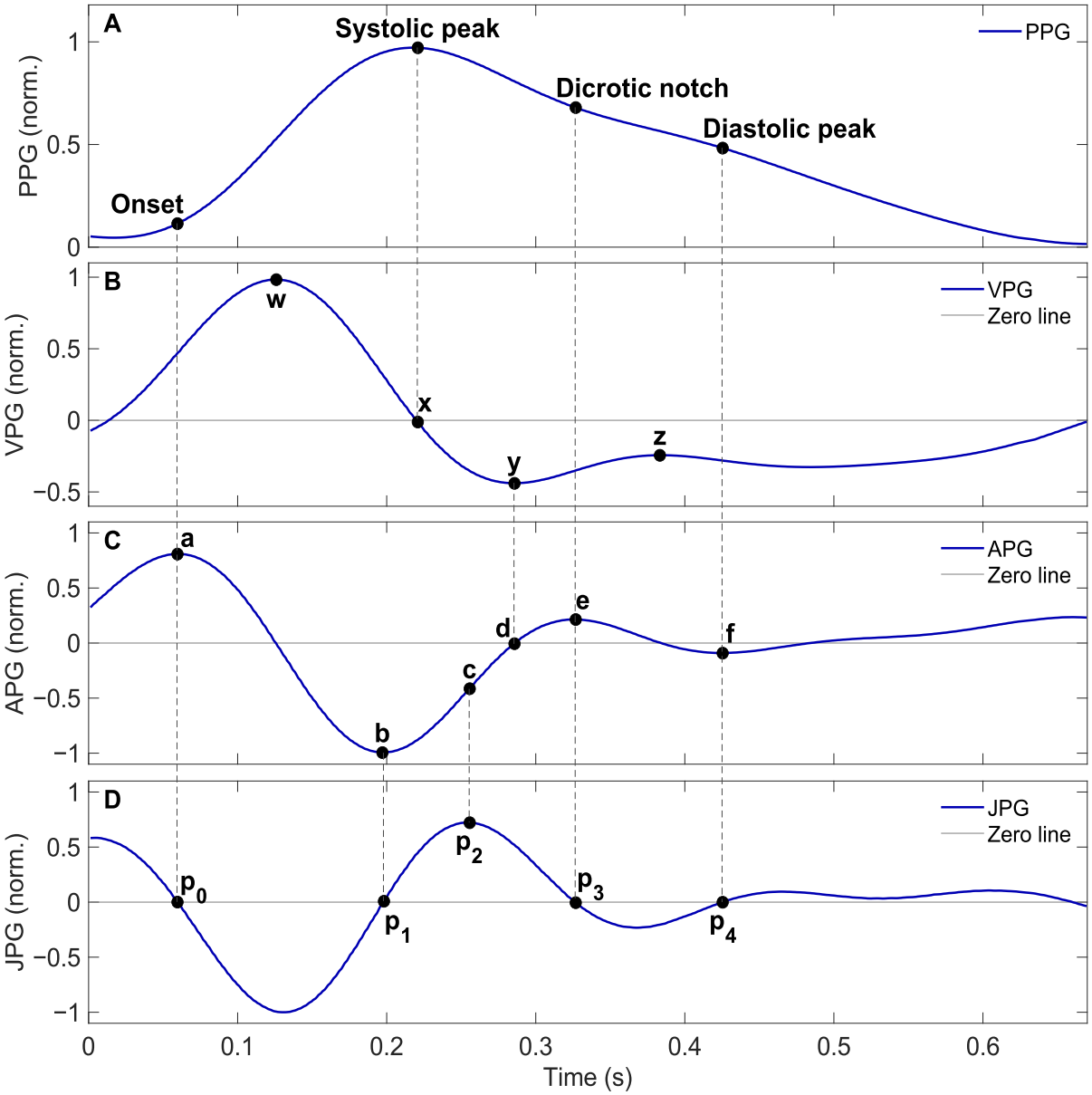

Figure 6.2 *Photoplethysmographic waveform and its successive time-derivatives. (A) PPG signal; (B) first derivative (VPG); (C) second derivative (APG); (D) third derivative (JPG).*

On the basis of these fiducial points, four amplitude ratios were computed for each cardiac cycle: the *b/a* ratio, the *c/a* ratio, the *e/a* ratio and the composite (*b*−*e*)/*a* index. The *d/a* ratio used in Chapter 5 was deliberately excluded from the present analysis, given the lack of a directly identifiable *d* deflection on the APG waveform of all 44 subjects.

For statistical analysis, each five-minute acquisition was divided into twenty non-overlapping 15-second segments. For each segment, the median of every APG index across all heartbeats was computed, and the subject-level representative value was obtained as the mean of the twenty segment medians. This double-aggregation procedure was adopted to mitigate the contribution of isolated artefacts while preserving the natural beat-to-beat variability of the indices. For each of the eight wavelength–site combinations, the relationship between APG indices and chronological age was assessed through Pearson's correlation coefficient, with statistical significance set at $\alpha = 0.05$. Least-squares linear regression lines were also computed to show how each index changes with age.

6.4 APG Analysis and Results

The analysis of the 44-subject cohort yielded a coherent picture in which both the wavelength of the optical source and the anatomical measurement site exert a measurable influence on the APG-derived indices and on their correlation with chronological age. Skin temperature was continuously recorded by the two NTC thermistors integrated into the prototype, yielding an average value of 29.2 ± 3.6 °C across the entire group, confirming the stability of thermal conditions throughout the entire experimental session.

6.4.1 Comparison Between Wavelengths

Figure 6.3 shows representative raw and filtered PPG waveforms, together with the corresponding APG signals and the five identified fiducial points, for each of the four wavelengths simultaneously acquired from the wrist and finger of one representative participant. A first qualitative observation, valid across all subjects of the cohort, is that the green and blue wavelengths consistently produced a more defined waveform morphology than red and infrared, with a narrower systolic peak, a clearly resolved dicrotic notch and a higher signal-to-noise ratio.

These qualitative differences were quantitatively confirmed by two complementary signal-quality metrics, namely the Perfusion Index (PI) and the spectral signal-to-noise ratio (SNR), computed as the power ratio between the cardiac band and the residual noise within 0.5–8 Hz. As reported in Table 6.1, the green and blue wavelengths systematically outperformed red and infrared at both sites: at the finger, green and blue reached PI values of 1.80 ± 0.78 % and 1.55 ± 0.57 % respectively, approximately 1.5–1.8 times the corresponding wrist values, indicating a substantially stronger pulsatile

component. Spectral SNR followed the same pattern, with the largest gap observed at the wrist (3.13–3.26 dB for green and blue versus 1.66–2.04 dB for red and infrared).

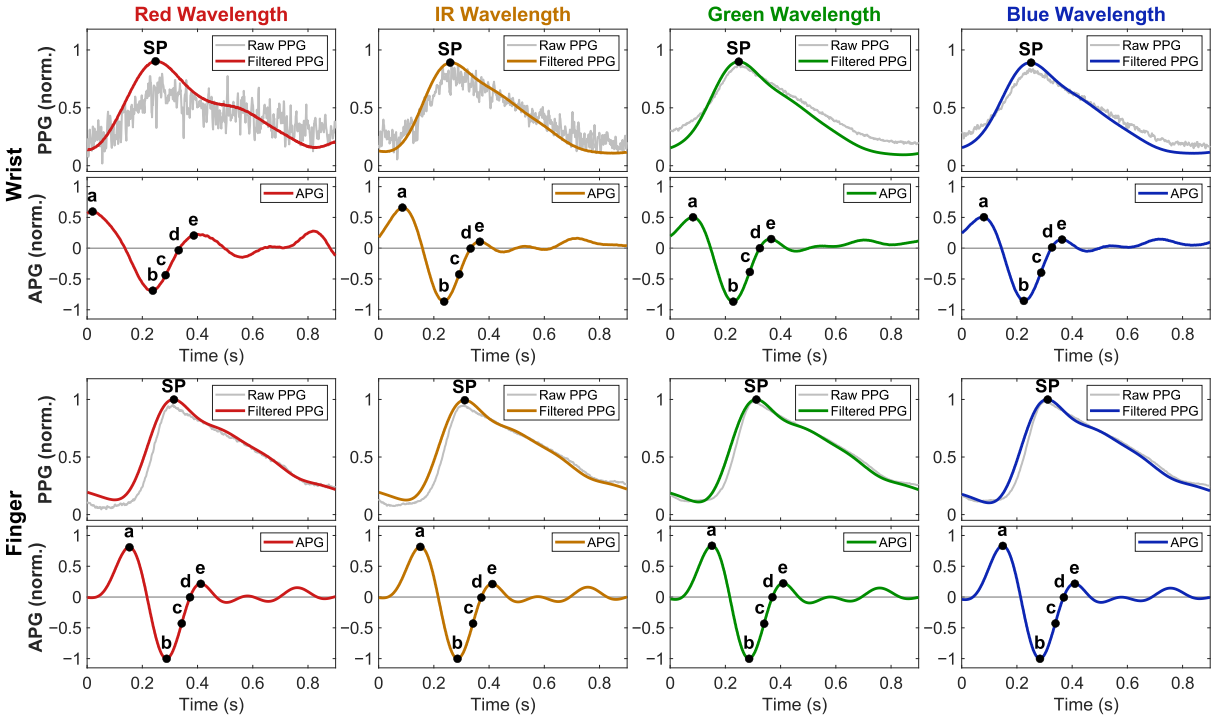

Figure 6.3 *PPG and APG waveforms for each wavelength and measurement site in a representative subject.*

Table 6.1 *— Signal-quality metrics computed on the filtered PPG signals for each wavelength–site combination (mean ± SD across the 44 subjects). PI = Perfusion Index; SNR = spectral signal-to-noise ratio in the cardiac band.*

Measurement site	Wavelength	PI (%)	SNR (dB)
Wrist	Red	1.01 ± 0.01	1.66 ± 1.01
	IR	1.01 ± 0.01	2.04 ± 1.03
	Green	1.03 ± 0.04	3.26 ± 0.83
	Blue	1.02 ± 0.03	3.13 ± 0.82
Finger	Red	1.03 ± 0.04	2.97 ± 1.14
	IR	1.09 ± 0.11	3.19 ± 0.97
	Green	1.80 ± 0.78	3.38 ± 0.94
	Blue	1.55 ± 0.57	3.35 ± 0.94

These signal-quality differences propagated coherently into the correlation between APG indices and chronological age, summarised in Figure 6.4 and Table 6.2.

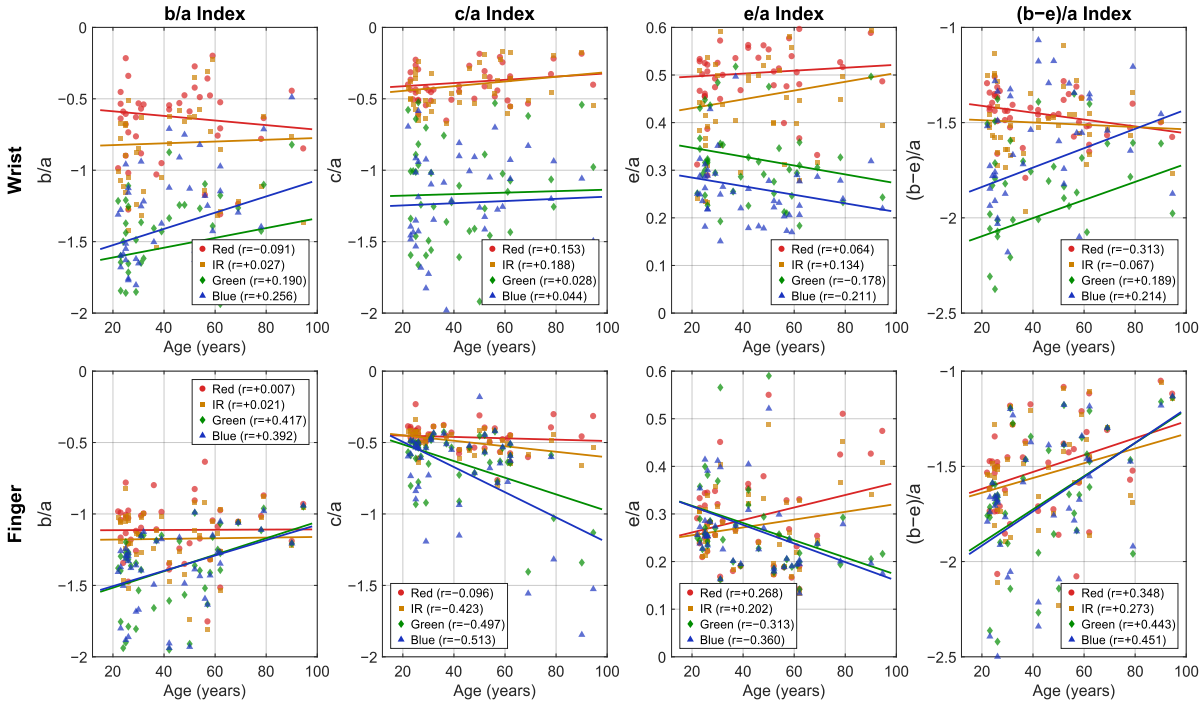

Figure 6.4 *Scatter plots of APG indices as a function of chronological age for each wavelength and measurement site, with linear regression lines and Pearson correlation coefficients.*

Table 6.2 — *Summary statistics of APG indices by measurement site and wavelength (mean ± SD across subjects), with Pearson's correlation coefficient with chronological age.*

Site	Wavelength	b/a index	c/a index	e/a index	(b − e)/a index
Wrist	Red	−0.625 ± 0.346 (r = −0.091)	−0.386 ± 0.144 (r = 0.153)	0.504 ± 0.094 (r = 0.064)	−1.454 ± 0.113 (r = −0.313)*
	IR	−0.809 ± 0.454 (r = 0.027)	−0.406 ± 0.171 (r = 0.188)	0.452 ± 0.135 (r = 0.134)	−1.501 ± 0.176 (r = −0.067)
	Green	−1.530 ± 0.353 (r = 0.190)	−1.166 ± 0.366 (r = 0.028)	0.325 ± 0.102 (r = −0.178)	−1.985 ± 0.493 (r = 0.189)
	Blue	−1.391 ± 0.433 (r = 0.256)	−1.228 ± 0.340 (r = 0.044)	0.263 ± 0.084 (r = −0.211)	−1.718 ± 0.464 (r = 0.214)
Finger	Red	−1.112 ± 0.210 (r = 0.007)	−0.462 ± 0.097 (r = −0.096)	0.292 ± 0.096 (r = 0.268)	−1.514 ± 0.249 (r = 0.348)*
	IR	−1.174 ± 0.216 (r = 0.021)	−0.494 ± 0.089 (r = −0.423)**	0.275 ± 0.079 (r = 0.202)	−1.548 ± 0.278 (r = 0.273)
	Green	−1.381 ± 0.271 (r = 0.417)**	−0.650 ± 0.229 (r = −0.497)***	0.275 ± 0.113 (r = −0.313)*	−1.696 ± 0.384 (r = 0.443)**
	Blue	−1.379 ± 0.268 (r = 0.392)**	−0.702 ± 0.336 (r = −0.513)***	0.270 ± 0.106 (r = −0.360)*	−1.705 ± 0.391 (r = 0.451)**

**p < 0.05, **p < 0.01, ***p < 0.001.*

At both anatomical sites, the red and infrared wavelengths produced generally weak and non-significant correlations with age ($|r| \leq 0.35$, $p > 0.05$ in 13 of 16 site–index combinations) and a markedly higher dispersion of the indices across the cohort. In contrast, the green and blue wavelengths produced significantly stronger correlations and physiologically consistent trends, with the *b/a* and (*b*−*e*)/*a* indices increasing with age and the *c/a* and *e/a* indices decreasing with age, as expected from the literature reviewed in Section 3.1.3.

6.4.2 Comparison Between Measurement Sites

The comparison between the two anatomical sites confirmed the finger as the location yielding the strongest and most consistent APG-derived correlations with age, while highlighting that the wrist still preserves usable trends for the green and blue wavelengths. At the finger, the four indices computed on the green and blue channels reached statistical significance with consistent and physiologically interpretable patterns: the *c/a* index showed the strongest correlations for blue ($r = -0.513$, $p < 0.001$) and green ($r = -0.497$, $p < 0.001$); the (*b*−*e*)/*a* composite index reached $r = +0.451$ ($p < 0.01$) for blue and $r = +0.443$ ($p < 0.01$) for green; the *b/a* index reached $r = +0.417$ ($p < 0.01$) for green and $r = +0.392$ ($p < 0.01$) for blue; and the *e/a* index reached $r = -0.360$ ($p < 0.05$) for blue and $r = -0.313$ ($p < 0.05$) for green.

At the wrist, the same wavelengths produced trends with the same direction and physiological interpretation, but with consistently lower absolute values of *r* and reduced statistical significance, in line with the lower signal quality reported in Section 6.4.1. The distribution of the APG indices, summarised by the box plots of Figure 6.5, further confirmed this pattern: at the finger, the interquartile ranges were 25–65 % narrower than at the wrist across all wavelengths and indices, indicating a more compact, reproducible extraction of features from the fingertip signal.

A complementary analysis was carried out on the intra-subject variability of the APG indices, computed as the beat-by-beat standard deviation within each subject and analysed as a function of chronological age (Figure 6.6 and Table 6.3). Two findings emerge from this analysis. First, the intra-subject variability is systematically lower at the finger than at the wrist for all wavelengths and indices, with mean SD values approximately two to three times smaller (e.g. for the *b/a* index, 0.15–0.24 at the finger versus 0.45–0.53 at the wrist), confirming the more reproducible feature extraction associated with the higher signal quality of the finger. Second, the intra-subject

variability of the green and blue indices remains substantially flat across the four decades of life covered by the cohort, with correlation coefficients between SD and age ranging from $r = -0.022$ to $r = +0.179$. In contrast, the red and infrared indices exhibit moderate-to-strong positive correlations between SD and age (red: $r = 0.34$ to 0.59; infrared: $r = 0.52$ to 0.60), indicating a substantial age-related degradation of the measurement consistency that is absent in the shorter-wavelength channels.

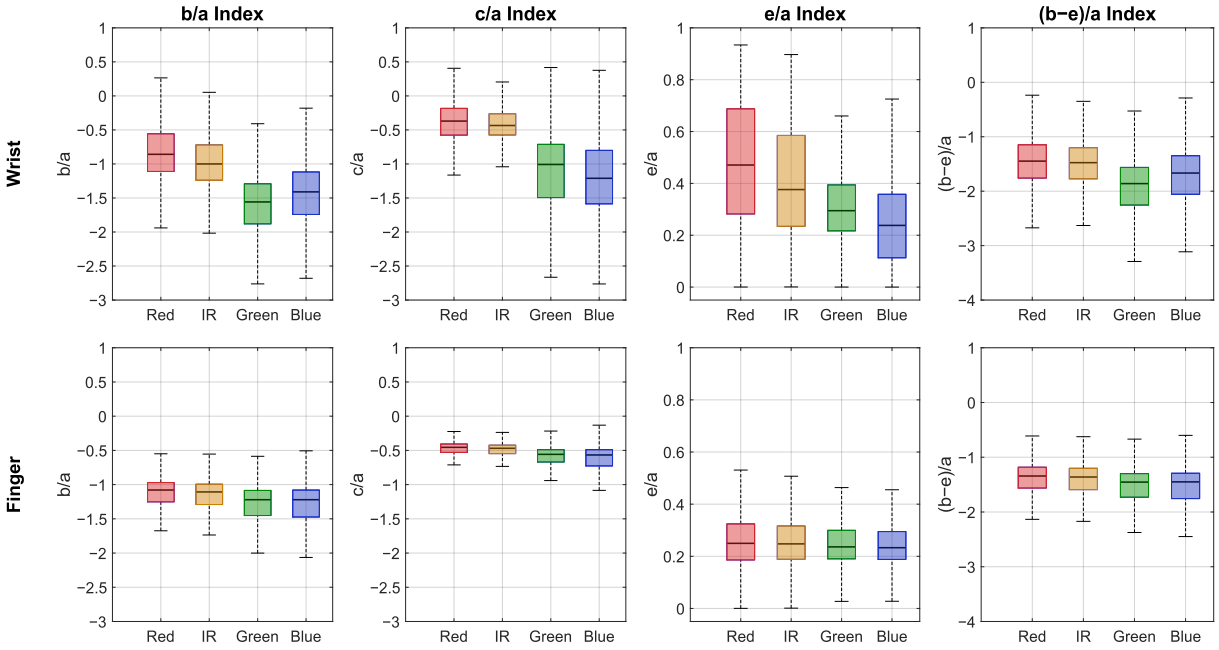

Figure 6.5 *Distribution of APG indices by wavelength and measurement site.*

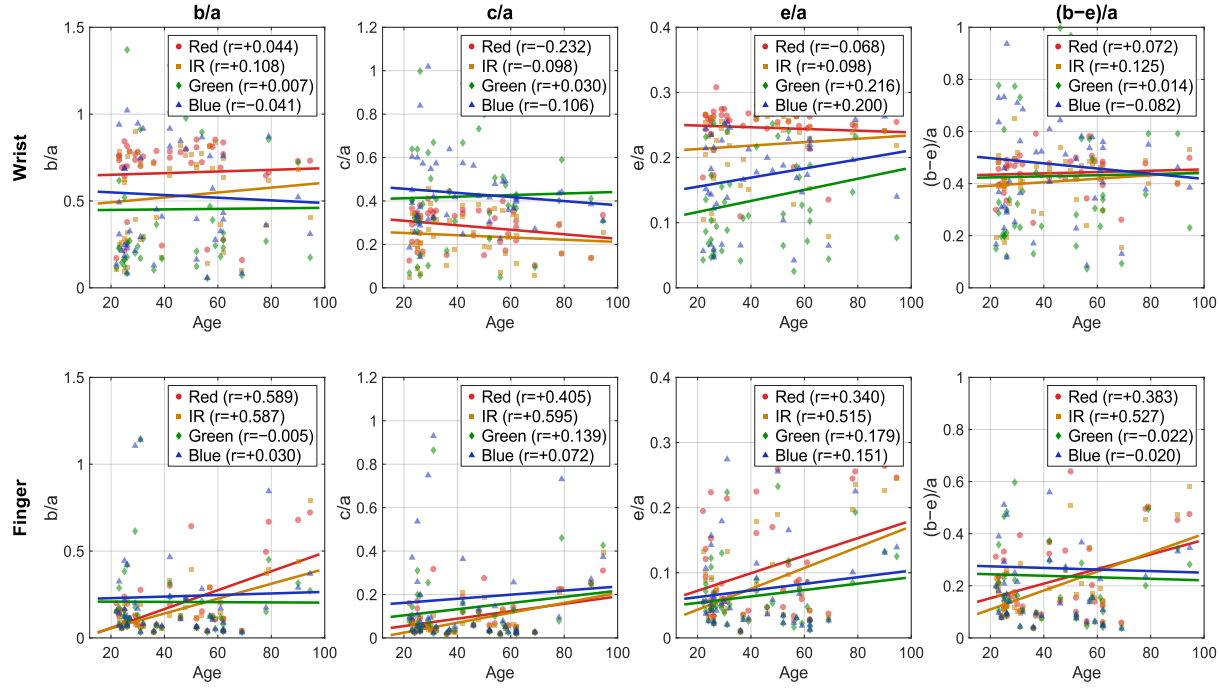

Figure 6.6 *Intra-subject standard deviation of the APG indices as a function of age for the four wavelengths, at the wrist (top row) and at the finger (bottom row).*

Table 6.3 *— Mean intra-subject SD of the APG indices and Pearson correlation between intra-subject SD and chronological age, by measurement site and wavelength.*

Measurement site	Wavelength	b/a index	c/a index	e/a index	(b − e)/a index
Wrist	Red	0.662 (r = 0.044)	0.284 (r = −0.232)	0.246 (r = −0.068)	0.440 (r = 0.072)
	IR	0.525 (r = 0.108)	0.240 (r = −0.098)	0.219 (r = 0.098)	0.408 (r = 0.125)
	Green	0.452 (r = 0.007)	0.421 (r = 0.030)	0.136 (r = 0.216)	0.429 (r = 0.014)
	Blue	0.532 (r = −0.041)	0.434 (r = −0.106)	0.172 (r = 0.200)	0.474 (r = −0.082)
Finger	Red	0.185 (r = 0.589)	0.095 (r = 0.405)	0.104 (r = 0.340)	0.218 (r = 0.383)
	IR	0.155 (r = 0.587)	0.078 (r = 0.595)	0.081 (r = 0.515)	0.195 (r = 0.527)
	Green	0.207 (r = −0.005)	0.137 (r = 0.139)	0.065 (r = 0.179)	0.237 (r = −0.022)
	Blue	0.239 (r = 0.030)	0.184 (r = 0.072)	0.075 (r = 0.151)	0.268 (r = −0.020)

6.5 Discussion

The identification of the optimal wavelength–site configuration was based on four explicit and complementary criteria: signal quality, strength of the correlation with chronological age, physiological interpretability of the observed trends, and compatibility with real-world wearable monitoring. The results converge on four corresponding observations. First, the green and blue wavelengths produce APG indices with significantly stronger correlations with chronological age and with trends that are more physiologically consistent with the literature than the red and infrared wavelengths. Second, the finger is confirmed as the most accurate measurement site for APG analysis, but consistent trends are also observed at the wrist for the green and blue channels. Third, the differences in correlation strength between sites and wavelengths are paralleled by underlying differences in signal quality, with green and blue yielding markedly higher Perfusion Index and spectral SNR at both sites. Fourth, the intra-subject variability of the green and blue indices remains essentially age-independent, while red- and infrared-derived indices become progressively less reproducible in older subjects.

The superior performance of the green and blue wavelengths is well supported by the established physics of light–tissue interaction recalled in Section 2.2.4. Wavelengths in the

475–580 nm range selectively probe the arterioles of the superficial dermal vascular plexus [213], while red and infrared wavelengths penetrate into the subcutaneous tissue and intercept a more heterogeneous blood volume that includes non-pulsatile venous and tissue contributions [214,215]. This depth-selective behaviour has a direct effect on the AC/DC ratio of the acquired signal [108,216] and, ultimately, on the morphological resolution of the APG waveform, as confirmed by the signal-quality metrics reported in Table 6.1.

In terms of comparison between sites, the superiority of the finger is consistent with the well-known anatomical differences between the two locations: the dense network of terminal arteries and arteriovenous anastomoses of the fingertip provides a strong pulsatile signal in a thin tissue layer [217], while at the wrist the radial and ulnar arteries lie deeper beneath several layers of tendons, connective and dermo-subcutaneous tissue [218,219], which attenuate the pulsatile component and introduce greater morphological variability into the PPG waveform [100,220]. The Perfusion Index values measured in our cohort (1.80 % and 1.55 % at the finger for green and blue, against 1.03 % and 1.02 % at the wrist) provide a direct quantitative correlate. The age-dependent behaviour of the APG indices on the green and blue channels at the finger is consistent with the trends originally documented by Takazawa et al. [124] on 600 subjects ($r = 0.75$ for b/a, $r = -0.67$ for c/a, $r = 0.80$ for AGI), and confirmed in subsequent cohorts [181,221].

A specific methodological consideration deserves attention. In all 44 subjects of the cohort, and at both measurement sites, the *c* and *d* waves were not directly identifiable as local extrema on the APG waveform, even in the youngest participants. This pattern, classified as *Case I* within the multi-derivative framework introduced in Section 2.3.4 [130], is documented in the literature as a possible consequence of vascular aging [222], but its universal occurrence in our cohort suggests an additional contribution from the optical front-end of the integrated MAX86916 sensor, whose internal digital filtering chain has been reported to alter the fine morphology of the PPG waveform [223]. Although the multi-derivative VPG–JPG strategy fully compensated for this limitation in the present study, it should be acknowledged as a factor that would deserve further investigation with analog front-ends in future development of the prototype.

Several other limitations should also be acknowledged. The cohort, although wider than in many comparable studies and spanning the entire adult age range, is exclusively composed of healthy volunteers; the inclusion of subjects with established cardiovascular risk factors would allow a more direct assessment of the diagnostic potential of the APG indices and

motivates the cardiometabolic-screening investigation presented in Chapter 7. Acquisitions were performed at rest and under controlled thermal conditions, and the generalisation of the findings to motion-rich and thermally variable scenarios would require dedicated investigations.

Within these limitations, the study consolidates the optimal wavelength–site combination for APG-based vascular aging assessment in wearable devices: green and blue wavelengths acquired at the finger represent the most accurate configuration, while green and blue wavelengths at the wrist preserve a usable, physiologically consistent signal that opens the way to large-scale, smartwatch-based cardiovascular screening. This second observation is particularly relevant given that the dominant form factor of consumer wearables, the smartwatch [90,224], is structurally constrained to wrist measurements, and that the inclusion of a green or blue channel in such devices is technologically straightforward and already widespread.

Chapter 7 — APG Indices as Digital Biomarkers of Cardiometabolic Health

7.1 Introduction and Objectives

The investigations presented in Chapters 5 and 6 progressively consolidated the role of the second derivative of the PPG signal as a non-invasive optical surrogate of vascular aging: Chapter 5 established the in vitro and in vivo robustness of the *d/a* ratio in a small cohort of nine healthy volunteers, and Chapter 6 extended the analysis to four wavelengths and two anatomical sites in 44 healthy participants spanning the full adult age range. In both studies, however, the populations were composed exclusively of healthy subjects, and the analytical question was confined to the relationship between APG indices and chronological age. The translational potential of these indices for *clinical* applications, that is, their ability to discriminate not only ageing but also the vascular alterations induced by established cardiovascular and metabolic disease, has remained therefore an open question.

This question is methodologically critical because the construct of vascular aging, as discussed in Section 2.1.3, embeds a fundamental distinction between chronological age and biological age: the former reflects the passage of time, while the latter integrates the cumulative damage produced by cardiovascular disease, such as hypertension, diabetes, dyslipidaemia, and other risk factors that accelerate the structural and functional deterioration of the arterial wall. A proper *digital biomarker* of vascular health is therefore expected not only to track chronological age in healthy populations, but also to detect and possibly stratify the early vascular signatures of common cardiometabolic disorders, ideally with a quantitative metric of clinical separability between groups.

Within this framework, the study presented in this chapter, actually submitted as Diana et al., *Measurement* 2026, pursued three specific objectives:

(i) to evaluate, on a substantially larger and clinically heterogeneous cohort than those analysed in Chapters 5 and 6, the four conventional APG indices (*b/a*, *c/a*, *d/a* and AGI) introduced in Section 2.3.4, in three clinically distinct groups: healthy normotensive subjects, hypertensive patients and diabetic patients;

(ii) to verify the within-group correlations of the APG indices with chronological age, in order to confirm whether the age dependence observed in healthy participants in Chapters 5 and 6 is preserved also in the presence of established cardiovascular disease;

(iii) to quantify the discriminative power of each APG index between clinical groups through a complementary statistical framework that combines null-hypothesis testing, effect-size analysis (Cohen's *d*) and a distribution-overlap metric (Hellinger distance), in order to assess whether and to what extent the APG indices behave as digital biomarkers of cardiometabolic health.

The present investigation was based on a publicly available clinical PPG database, which provides simultaneous PPG recordings, clinical labels and anthropometric data on a substantially larger and more heterogeneous population than the cohorts otherwise accessible within the doctoral project. This methodological choice allowed the analytical framework developed in the previous chapters to be evaluated on a clinically validated population, on which the literature has so far reported only partial and pathology-specific analyses.

7.2 Database and Study Population

The study was based on the PPG-BP (Photoplethysmography-Blood Pressure) public database developed by Liang and colleagues at Guilin People's Hospital, China [225], which contains 657 PPG segments acquired from 219 adult subjects and is associated with clinical labels for hypertension, diabetes mellitus and cerebrovascular disease, together with biometric and anthropometric variables. PPG signals were originally acquired at the fingertip with an infrared LED at $\lambda = 905$ nm, sampled at 1 kHz with a 12-bit ADC, after a 10-minute acclimatisation period and a synchronous brachial blood-pressure measurement performed with an Omron HEM-7201 sphygmomanometer.

Subjects were stratified into three clinical groups according to the labels available in the database: healthy normotensive subjects without diagnosed cardiovascular or metabolic disease; hypertensive patients (pre-hypertension, stage I or stage II) without diabetes; and diabetic patients, regardless of the concomitant presence of hypertension. Subjects with cerebrovascular disease were excluded from the analysis, given the structural rather than functional nature of the underlying vascular alteration. Signal-level quality control was performed on each PPG segment through the Skewness Signal Quality Index (SSQI), retaining only segments with SSQI ≥ 0.41, the threshold validated in the literature for reliable APG fiducial-point extraction [125]. The procedure removed 35 segments out of 399 (8.8 %) and led to the inclusion of 364 valid waveforms from 133 participants.

The demographic and clinical characteristics of the final cohort are summarised in Table 7.1. Forty-five subjects were classified as healthy (33.8 %), 68 as hypertensive (51.1 %) and 20 as diabetic (15.0 %). The mean age of the population was 57.4 ± 16.1 years (range 21–86); a clinically expected age imbalance was present across groups, with healthy participants on average younger (47.8 ± 17.2 years) than hypertensive (63.0 ± 13.2 years) and diabetic patients (60.0 ± 12.8 years). This imbalance reflects the well-known epidemiology of arterial hypertension and type-2 diabetes mellitus, but is also a methodological factor that has been explicitly addressed in the analyses presented below, where the within-group correlations between APG indices and chronological age were systematically computed and reported alongside the between-group comparisons.

Table 7.1 *— Demographic and clinical characteristics of the study population. Values are expressed as mean ± SD or n (%). SBP = systolic blood pressure; DBP = diastolic blood pressure; HR = heart rate; BMI = body mass index.*

	Variable	Healthy	Hypertensive	Diabetic	Total
Demographics	Age Range (yr)	21-85	25-86	38-84	21-86
	Mean and Std Age (yr)	47.8 ± 17.2	63.0 ± 13.2	60.0 ± 12.8	57.4 ± 16.1
	Male	17 (37.8%)	27 (39.7%)	10 (50.0%)	54 (40.6%)
	Female	28 (62.2%)	41 (60.3%)	10 (50.0%)	79 (59.4%)
Clinical Parameters	Height (cm)	160.1 ± 8.2	160.1 ± 8.3	161.3 ± 9.2	160.3 ± 8.3
	Weight (kg)	57.5 ± 10.5	60.9 ± 11.9	65.8 ± 12.3	60.5 ± 11.7
	BMI (kg/m²)	22.4 ± 3.9	23.7 ± 4.0	25.2 ± 3.9	23.5 ± 4.0
	SBP (mmHg)	106.7 ± 9.0	141.4 ± 14.5	131.7 ± 14.0	128.2 ± 20.3
	DBP (mmHg)	64.0 ± 6.3	76.4 ± 11.1	74.7 ± 10.9	72.0 ± 11.2
	HR (bpm)	70.3 ± 8.9	70.1 ± 8.9	66.8 ± 8.6	69.7 ± 8.9
BP Classification	Normotensive, n (%)	45 (100.0%)	-	3 (15.0%)	48 (36.2%)
	Pre-hypertension, n (%)	-	37 (54.4%)	12 (60.0%)	49 (36.8%)
	Stage 1, n (%)	-	22 (32.4%)	4 (20.0%)	26 (19.5%)
	Stage 2, n (%)	-	9 (13.2%)	1 (5.0%)	10 (7.5%)

7.3 Methodology

The signal-processing pipeline followed the same general scheme established in Section 2.3.1 and adopted in Chapter 6, with one specific adaptation related to the computation of the derivatives. Each PPG segment was first filtered with a fourth-order Chebyshev Type II bandpass filter (passband 0.5–8 Hz, stopband attenuation 20 dB) [91]. The filtered signal was then normalised to enable inter-subject comparisons of the APG fiducial-point amplitudes. The first and second derivatives of the PPG signal were obtained by applying a Savitzky-Golay filter with first-order differentiation, third-order polynomial and a 150 ms window to the filtered PPG signal and again to the VPG, yielding the acceleration plethysmogram. The APG signal was finally normalised to its maximum absolute value, yielding amplitudes in the range [−1, 1], which made the four APG indices directly comparable across all subjects and clinical groups.

The five fiducial points of the APG waveform were directly identified on each cardiac cycle (Figure 7.1). Wave *a* was identified as the global maximum of the APG, wave *b* as the global minimum, waves *c* and *d* as the first local positive maximum and the first local minimum following *b*, respectively, and wave *e* as the second positive local maximum following *b*. On this basis, the four analysed APG ratios, namely the *b/a*, *c/a* and *d/a* indices and the composite Aging Index AGI = $(b-c-d-e)/a$, were computed beat-by-beat for each segment and then averaged at subject level.

The statistical analysis was articulated in two complementary directions. First, the within-group relationship between each APG index and chronological age was assessed through Pearson's correlation coefficient (r) with the corresponding p-values. Second, between-group comparisons were performed through a structured pipeline of formal tests: normality was checked within each group with the Lilliefors test and homoscedasticity across groups with the Levene test (median-based version); when both assumptions were satisfied, a one-way ANOVA was performed, otherwise the non-parametric Kruskal–Wallis test was used. Significant omnibus differences ($p < 0.05$) were followed by post-hoc pairwise comparisons (Tukey HSD after ANOVA, Dunn with Bonferroni correction after Kruskal–Wallis), and for each pairwise comparison Cohen's d was computed as a measure of effect size, with the conventional thresholds $|d| < 0.2$ negligible, $0.2 \leq |d| < 0.5$ small, $0.5 \leq |d| < 0.8$ medium and $|d| \geq 0.8$ large. To complement the mean-based effect size with a distribution-aware metric, the Hellinger distance between the index distributions of each pair of groups was also computed, ranging from 0 (identical distributions) to 1 (no overlap).

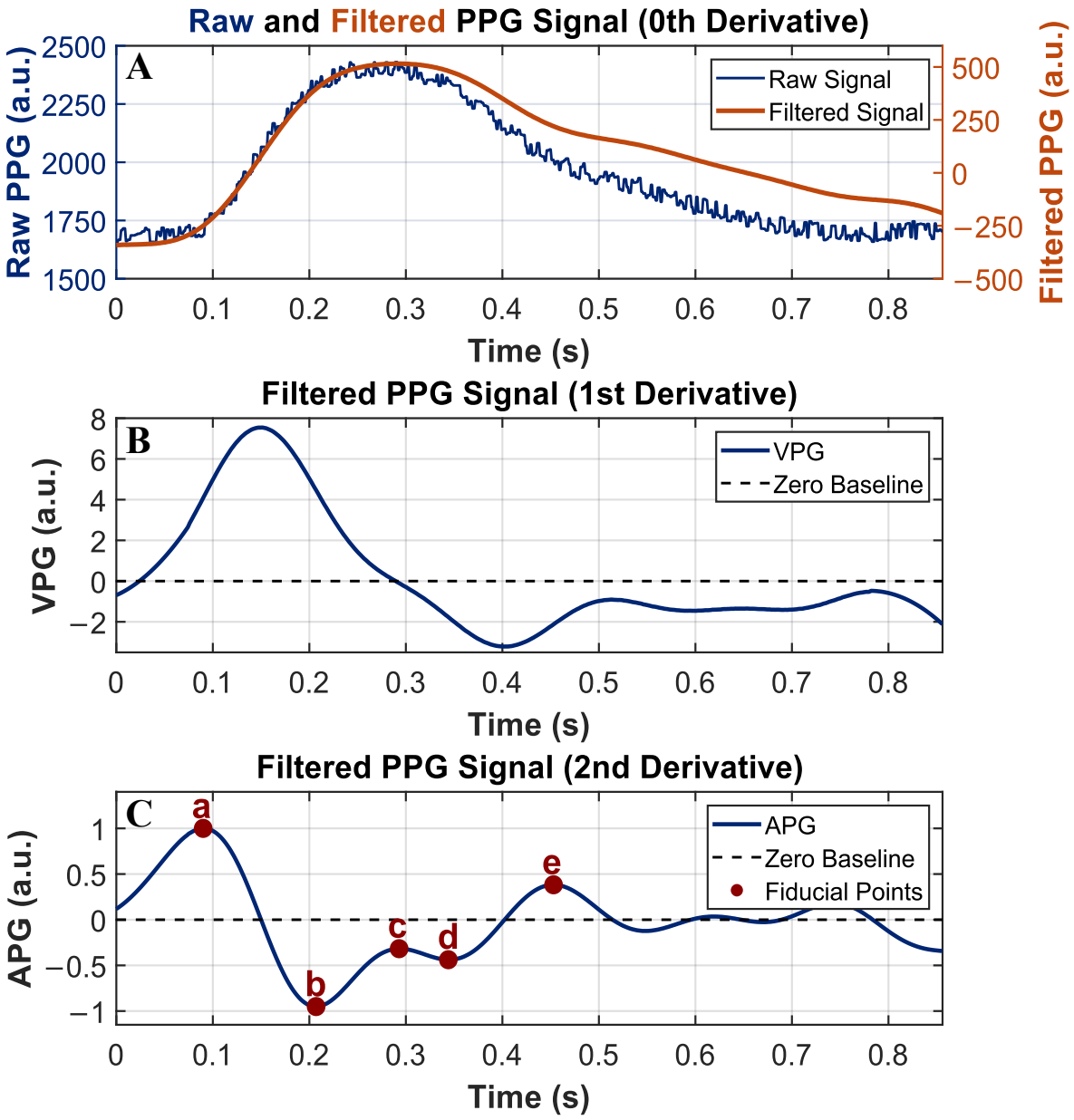

Figure 7.1 - *PPG signal processing and identification of APG fiducial points. (A) Raw (blue) and filtered (orange) PPG signals. (B) First derivative (VPG). (C) Second derivative (APG) with the five fiducial points (a, b, c, d, e).*

7.4 Results

Representative APG waveforms from each of the three clinical groups are reported in Figure 7.2. In the healthy group, a progressive flattening of the *c* and *d* deflections was observed with increasing age, while the youngest subjects retained a well-defined dicrotic notch and prominent fiducial points. In the hypertensive group, markedly altered APG patterns appeared even in younger subjects, and in the diabetic group, vascular alterations of comparable magnitude were observed in subjects aged 48 and 55 years, suggesting an accelerated vascular ageing relative to chronological age.

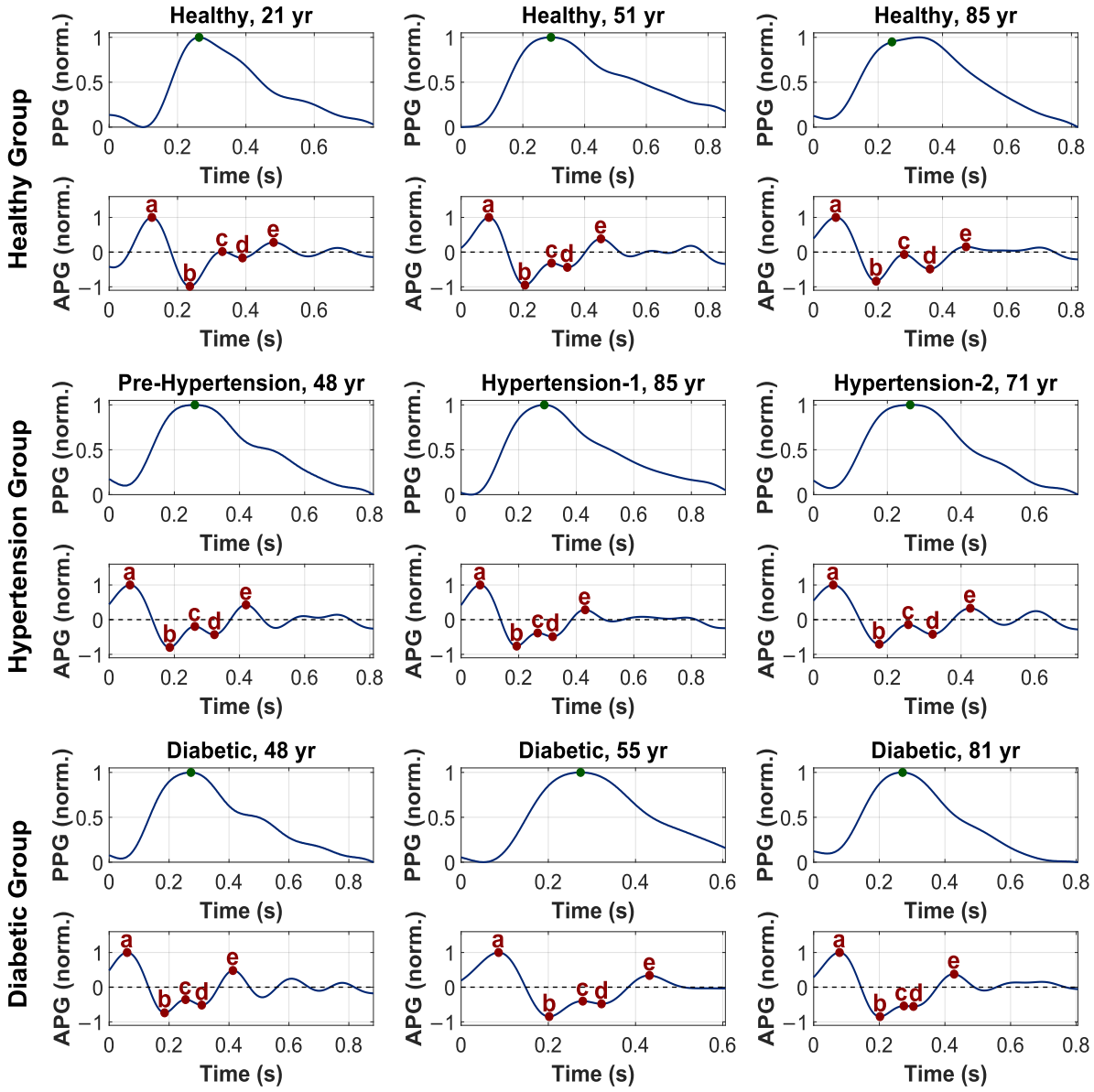

Figure 7.2 Representative PPG waveforms and corresponding APG waveforms for subjects from the three clinical groups at different ages.

7.4.1 Correlation with Chronological Age

All four APG indices exhibited statistically significant correlations with chronological age within each of the three clinical groups, confirming that the age-dependent behaviour observed in healthy participants in Chapters 5 and 6 is preserved also in the presence of cardiovascular disease (Figure 7.3 and Table 7.2). In the healthy group, *b/a* and AGI increased with age ($r = +0.446$ and $r = +0.437$, both $p < 0.001$), while *c/a* and *d/a* decreased ($r = -0.421$ and $r = -0.421$, $p < 0.001$), in full agreement with the direction of the trends documented in the literature on healthy populations.

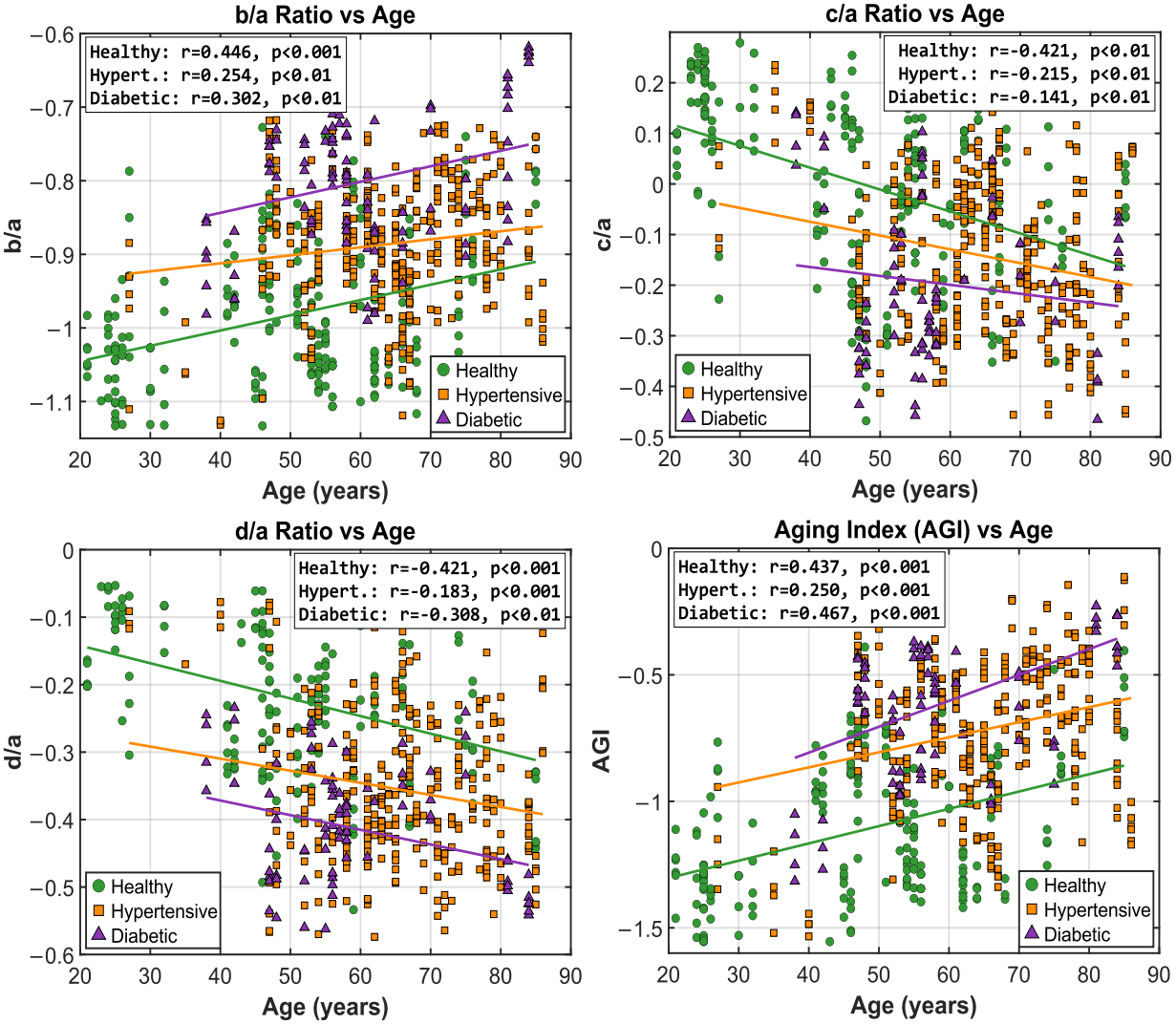

Figure 7.3 *Scatter plots of the four APG indices (AGI, b/a, c/a, d/a) as a function of chronological age, stratified by clinical group: healthy (green), hypertensive (orange) and diabetic (purple). Linear regression lines, Pearson correlation coefficients (r) and significance levels (p) are reported for each group.*

In the hypertensive group, the same trends were preserved with reduced absolute correlation strength ($|r|$ in the range 0.18–0.25, $p < 0.01$), while in the diabetic group the AGI and *d/a* reached intermediate values ($|r| = 0.467$ and 0.308 respectively). The lower correlations observed in the pathological groups are interpretable as the consequence of two concurrent mechanisms: a reduced age range within the disease cohorts (prevalently middle-aged to elderly), and the superposition of disease-driven vascular alterations on the age-driven baseline trend, which compresses the dynamic range of the indices within each pathological group.

Crucially, at any given chronological age, the APG indices of the pathological groups were systematically displaced with respect to the healthy regression lines: subjects with hypertension and diabetes exhibited consistently higher *b/a* and AGI values, and consistently more negative *c/a* and *d/a* values, than age-matched healthy participants. This translation of the regression lines is the key observation that motivates the between-group comparisons reported in Section 7.4.2, since it suggests that APG indices encode a vascular ageing component that is not fully reducible to chronological age and that may capture a clinically informative residual associated with the underlying disease state.

Table 7.2 *— APG index values (mean ± SD), Pearson correlation coefficients (r) with chronological age and significance levels (p) for healthy, hypertensive and diabetic subjects.*

Clinical group	Statistic	b/a	c/a	d/a	AGI
Healthy Subjects	Mean	-0.983	0.001	-0.222	-1.083
	Std. Dev.	0.095	0.170	0.108	0.279
	r-value	0.446	-0.421	-0.421	0.437
	p-value	<0.001	<0.01	<0.001	<0.001
Hypertensive Subjects	Mean	-0.886	-0.142	-0.355	-0.720
	Std. Dev.	0.085	0.151	0.110	0.279
	r-value	0.254	-0.215	-0.183	0.250
	p-value	<0.01	<0.01	<0.001	<0.001
Diabetic Subjects	Mean	-0.792	-0.197	-0.403	-0.647
	Std. Dev.	0.094	0.154	0.088	0.270
	r-value	0.302	-0.141	-0.308	0.467
	p-value	<0.01	<0.01	<0.01	<0.001

7.4.2 Comparison Between Clinical Groups

The verification of parametric assumptions (Lilliefors and Levene tests) confirmed normality and homoscedasticity for the *b/a* and *c/a* indices, justifying the use of one-way ANOVA, while the *d/a* and AGI indices required the non-parametric Kruskal–Wallis test due to deviations from normality in at least one group. The omnibus tests yielded statistically significant differences across the three clinical groups for all four APG indices ($p < 0.001$ in every case), motivating the post-hoc pairwise comparisons described below. The distribution of the four APG indices in the three clinical groups is illustrated by the box plots of Figure 7.4 and by the Gaussian-fit comparison of Figure 7.5. The box plots provide a non-parametric summary of the median, interquartile range and tails of each distribution, while the Gaussian fits, although not used in the formal statistical tests, offer a complementary visualisation of the relative position and dispersion of the means of the three groups. Both representations consistently show a progressive shift of the indices from healthy subjects, through hypertensive and diabetic patients, with a partial overlap of the distributions in the central regions and a systematic separation between the healthy and the pathological groups along all four indices.

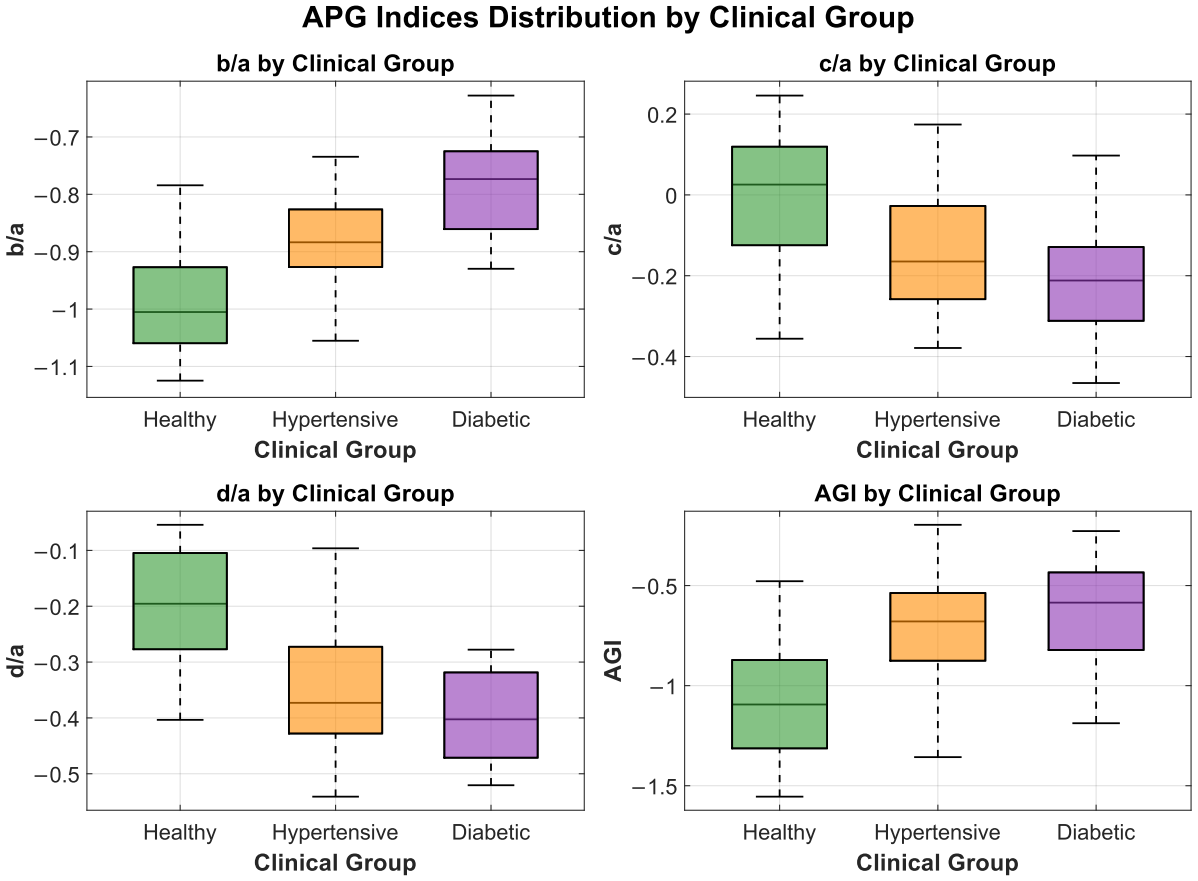

Figure 7.4 *Box plots showing the distribution of the four APG indices in the three clinical groups.*

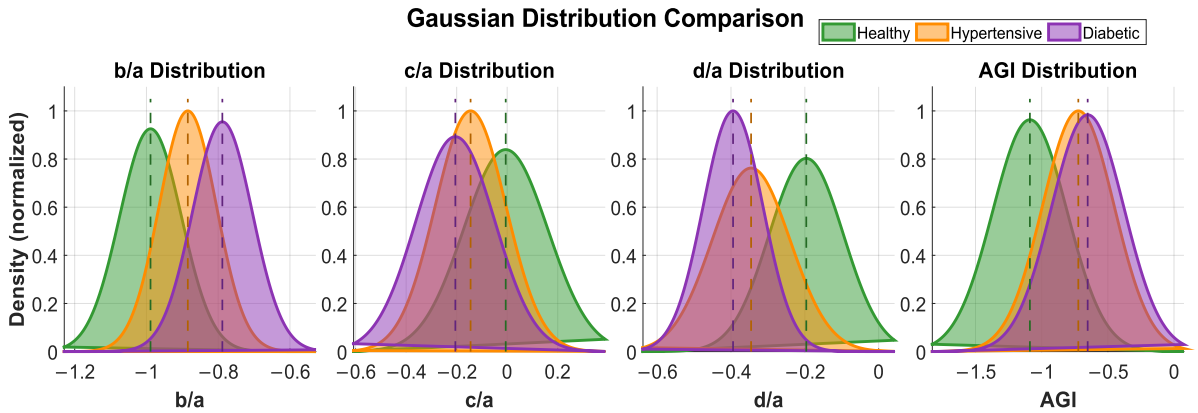

Figure 7.5 *Normalised Gaussian distributions of the four APG indices for the three clinical groups. The vertical dotted lines indicate the mean value of each group.*

Post-hoc pairwise comparisons were performed using the Tukey HSD test for *b/a* and *c/a*, and the Dunn test with Bonferroni correction for *d/a* and AGI. The corresponding effect sizes (Cohen's *d*) are summarised in Figure 7.6 and reported, together with the post-hoc *p*-values and the Hellinger distances between the index distributions, in Table 7.3. The comparison between healthy and hypertensive subjects yielded large effect sizes for all four indices ($|d|$ = 1.26 for *b/a*, 0.92 for *c/a*, 1.44 for *d/a*, 1.33 for AGI), with the *d/a* ratio emerging as the most discriminative parameter, in line with its established role as a marker of peripheral wave reflection and arterial stiffness. The Hellinger distances of this comparison ranged from 0.32 (*c/a*) to 0.48 (*d/a*), indicating large mean-based separability with persisting moderate distributional overlap, a pattern that is methodologically informative because it suggests that no single APG index, taken in isolation, is sufficient for individual-level classification, while the combination of multiple indices may achieve substantially higher diagnostic accuracy.

The comparison between healthy and diabetic subjects produced the largest effect sizes of the entire study: $|d|$ = 2.35 for *b/a*, 1.22 for *c/a*, 2.10 for *d/a* and 1.57 for AGI, all substantially exceeding the threshold for large effects ($|d| > 0.8$), with Hellinger distances reaching 0.71 for *b/a*, the highest separability observed across all the comparisons performed. This pattern is consistent with the well-documented impact of diabetes mellitus on the arterial wall, which combines metabolic dysfunction and accelerated stiffening, and aligns with the morphological observations of Figure 7.2, where diabetic subjects in their forties and fifties showed APG patterns comparable to those of much older hypertensive subjects.

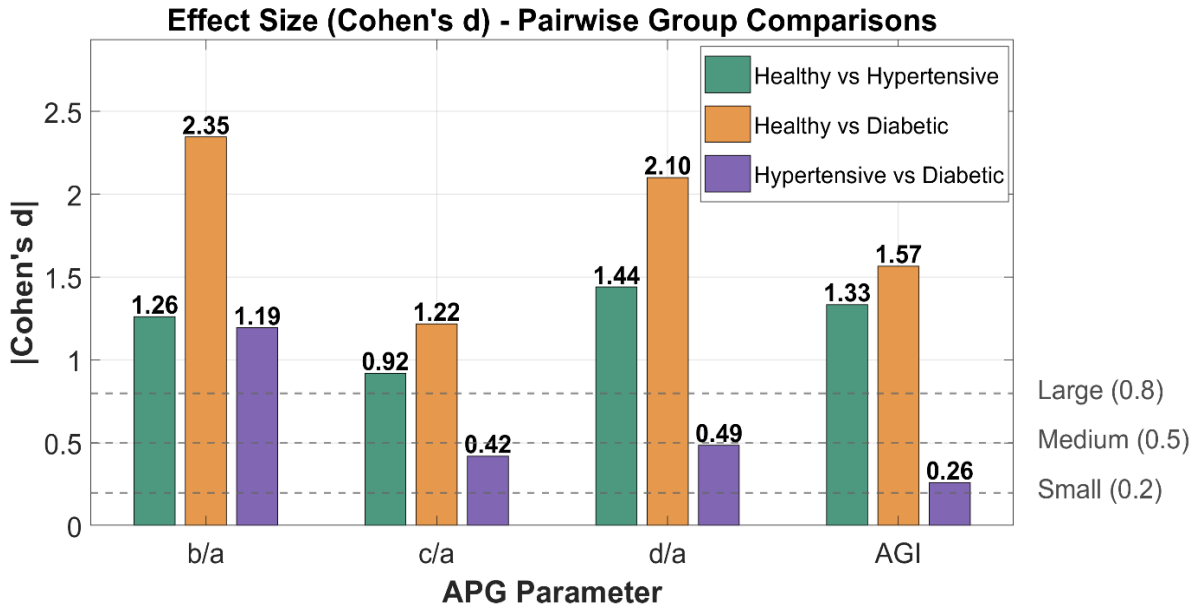

Figure 7.6 *Effect sizes (Cohen's d) for pairwise comparisons between the three clinical groups, computed for each of the four APG indices. Dashed horizontal lines indicate the conventional thresholds for small (0.2), medium (0.5) and large (0.8) effects.*

The most distinctive finding of the present analysis emerged from the direct comparison between hypertensive and diabetic subjects, whose vascular alterations have so far been treated separately in the APG literature. For *c/a*, *d/a* and AGI, this comparison yielded small or negligible effect sizes ($|d|$ = 0.42, 0.49 and 0.26 respectively), with Hellinger distances between 0.09 and 0.22, indicating an almost complete overlap of the distributions and suggesting that, once vascular damage is established, hypertension and diabetes converge towards similar APG signatures along these three indices. The *b/a* ratio, in contrast, retained a large effect size ($|d|$ = 1.19, $p < 0.001$) and a Hellinger distance of 0.40, identifying it as the only single APG index capable of discriminating, in this dataset, between hypertension and diabetes. From a pathophysiological perspective, this finding may reflect the fact that *b/a* is dominated by the early systolic deceleration of arterial flow, which is more sensitive to the structural alterations of the arterial wall induced by chronic hyperglycaemia (e.g. advanced glycation end-products, collagen cross-linking) than to the predominantly haemodynamic alterations associated with hypertension.

Table 7.3 *— Post-hoc pairwise comparisons between clinical groups for each APG index. Cohen's d (effect size), Hellinger distance (distributional overlap) and effect interpretation are reported.*

Index	Comparison	Post-hoc p	Cohen's d	Hellinger	Effect
b/a	Healthy vs Hypert.	< 0.001***	−1.26	0.42	Large
	Healthy vs Diabetic	< 0.001***	−2.35	0.71	Large
	Hypert. vs Diabetic	< 0.001***	−1.19	0.40	Large
c/a	Healthy vs Hypert.	< 0.001***	0.92	0.32	Large
	Healthy vs Diabetic	< 0.001***	1.22	0.42	Large
	Hypert. vs Diabetic	0.281	0.42	0.15	Small
d/a	Healthy vs Hypert.	< 0.001***	1.44	0.48	Large
	Healthy vs Diabetic	< 0.001***	2.10	0.67	Large
	Hypert. vs Diabetic	0.361	0.49	0.22	Small
AGI	Healthy vs Hypert.	< 0.001***	−1.33	0.45	Large
	Healthy vs Diabetic	< 0.001***	−1.57	0.52	Large
	Hypert. vs Diabetic	1.000	−0.26	0.09	Small

** $p < 0.05$; ** $p < 0.01$; *** $p < 0.001$.*

7.5 Discussion

The results presented in Section 7.4 converge on three main observations. First, the four canonical APG indices preserve a statistically significant correlation with chronological age in all three clinical groups, confirming the robustness of the age dependence already documented in healthy populations in Chapters 5 and 6 and consolidating the role of APG as an age-tracking optical biomarker. Second, the APG indices effectively discriminate between healthy and pathological populations, with consistently large effect sizes when healthy subjects are compared to either hypertensive or diabetic patients, the latter comparison reaching Cohen's *d* values up to 2.35 and Hellinger distances up to 0.71 for the *b/a* ratio. Third, when hypertensive and diabetic subjects are directly compared, only the *b/a* ratio retains a large effect size, suggesting a specific sensitivity of this index to the structural arterial alterations associated with diabetes mellitus.

The within-group correlations with age are quantitatively consistent with those reported by Takazawa et al. [124] in their seminal study on 600 subjects, where $r = 0.75$ was reported for *b/a* and $r = -0.72$ for *d/a* against chronological age. The lower absolute correlations obtained on the present cohort are explained by two concurrent factors: the systematic stratification of the sample by clinical condition, which compresses the within-group dynamic range, and the smaller and less age-balanced size of the individual clinical groups when compared to the systematic decade-by-decade sampling adopted in the original Takazawa investigation. The *d/a* trend observed here in the healthy group ($r = -0.421$) is also consistent with the in vivo evidence reported in Chapter 5 on the smaller cohort of nine healthy volunteers, where the same index reached $r = -0.90$ over a narrower age range.

From a translational perspective, the most relevant finding of the present chapter is the magnitude of the effect sizes observed when comparing healthy and pathological groups. Cohen's *d* values exceeding 1.0 for all four indices in the healthy-versus-hypertensive comparison and exceeding 2.0 for *b/a* and *d/a* in the healthy-versus-diabetic comparison are unusually large in clinical biomarker research and indicate that APG indices encode a vascular signature that goes substantially beyond chronological age. The Hellinger-distance analysis adds an important methodological caveat to this translational picture. Even when Cohen's *d* reaches large values, the distributions of the individual APG indices in the two compared groups still exhibit a moderate overlap, with Hellinger distances rarely exceeding 0.7. In practical terms, a Hellinger distance in the 0.5–0.7 range corresponds to distributions whose residual overlap still spans a substantial fraction of the two populations, so that any single-threshold decision on an individual index would entail a sensitivity–specificity trade-off too unfavourable for stand-alone diagnostic use, even where the separation of the group means is large. From a screening perspective, this means that no single APG index, taken in isolation, can be expected to provide a reliable individual-level classification, and that the operational value of these biomarkers is intrinsically multivariate.

The specific behaviour of the *b/a* ratio deserves a dedicated comment. The retention of a large effect size in the hypertensive-versus-diabetic comparison, in which the other three indices essentially collapse, is consistent with previous evidence indicating that *b/a* carries information on early-systolic arterial mechanics that may be specifically sensitive to the structural wall alterations of diabetic vasculopathy, including advanced glycation end-products and collagen cross-linking. Independent reports have similarly identified *b/a* as a distinctive marker for hypertension and diabetes detection through feature-selection

analysis [226,227], and a recent prospective study has shown that the *d/a* ratio independently predicts the future development of hypertension in normotensive middle-aged men [228], reinforcing the prognostic relevance of APG-derived parameters in the preclinical phase of cardiovascular disease.

Several limitations should be acknowledged. The diabetic group ($n = 20$) was substantially smaller than the healthy ($n = 45$) and hypertensive ($n = 68$) groups, which limits the statistical power of comparisons involving diabetic subjects and restricts the generalisability of the findings. Most diabetic subjects also exhibited some degree of hypertension, which does not allow the independent contribution of diabetes mellitus to the APG indices to be fully isolated from the haemodynamic burden of concomitant blood-pressure elevation. The PPG segments available in the database were short, with a limited number of analysable cardiac cycles per subject; longer recordings would improve the robustness of the fiducial-point estimation and reduce intra-subject variability.

Within these limitations, the present chapter consolidates the role of APG indices as non-invasive digital biomarkers of cardiometabolic health and represents the natural translational endpoint of the analytical framework progressively developed across Chapters 4 to 6. It should be emphasised, however, that the APG indices analysed here are to be regarded as promising screening biomarkers rather than standalone diagnostic tools: the residual overlap between the clinical-group distributions and the presence of possible confounding factors, including the age imbalance between groups, the frequent co-occurrence of hypertension and diabetes, and the limited size of the diabetic group, require that any clinical use of these indices be embedded in a multivariate framework and validated against reference measurements on larger, balanced cohorts. The combination of in vitro mechanical validation (Chapter 4), single-channel age-correlation analysis (Chapter 5), multi-wavelength multi-site optimisation (Chapter 6) and clinical-group discrimination (Chapter 7) defines a coherent methodological progression from physical interpretability to clinical utility, supporting the integration of APG-based analysis into the wearable cardiovascular-screening pipelines that consumer optical sensors already make technologically accessible at scale.

Chapter 8 — Conclusions and Future Developments

This doctoral project addressed the broader objective of advancing the use of photoplethysmographic sensors as a non-invasive, low-cost and clinically meaningful tool for vascular health assessment. The research followed an integrated path that progressively moved from a controlled in vitro environment to clinically heterogeneous populations, and from the physical characterisation of arterial stiffness to the morphological analysis of the PPG signal through its second derivative.

The in vitro study employed PPG sensors to estimate arterial wall stiffness on silicone phantom models designed to reproduce the mechanical behaviour of blood vessels under different physiological and pathological conditions, within a mock circulatory loop that simulated realistic haemodynamic settings. These results confirmed the feasibility of non-invasive stiffness estimation through pulse transit time and pulse wave velocity measurements and provided a solid experimental foundation for subsequent investigations. The same in vitro platform was also adapted, as a complementary line of work, to the non-invasive monitoring of transcatheter heart valves, showing that PPG-derived signals combined with machine learning can reconstruct valve performance parameters with promising accuracy.

The transition to in vivo analysis introduced the acceleration plethysmogram as a practical approach to assess vascular aging from a single measurement site. The combined in vitro–in vivo design confirmed that APG-derived morphological indices correlate strongly with both material stiffness and chronological age, consolidating their potential as non-invasive surrogates of vascular health.

Building on this evidence, the development of a custom multi-wavelength wearable prototype enabled a systematic comparison across four wavelengths and two anatomical sites. The green and blue wavelengths at the finger emerged as the optimal configuration, but the same wavelengths also preserved physiologically consistent trends at the wrist, demonstrating that the proposed analytical pipeline is compatible with the dominant smartwatch form factor. This is a key finding from a translational perspective: the green channel already present in most commercial heart-rate sensors could be sufficient to enable APG-based vascular monitoring without hardware modifications.

The final study extended the analysis to a clinically heterogeneous cohort including healthy, hypertensive and diabetic subjects. The APG indices proved capable of distinguishing healthy

from pathological vascular states and revealed a vascular aging component that goes beyond chronological age, suggesting a specific sensitivity to the structural alterations associated with different cardiometabolic conditions.

Looking beyond this work, several research directions emerge naturally. A first priority is the in vivo validation of the in vitro framework against the clinical gold standard, carotid–femoral pulse wave velocity, on cohorts that include both healthy subjects and patients with established cardiovascular disease. Complementary to this clinical validation, a dedicated metrological validation of the proposed measurement framework is envisaged, comprising the formal propagation of measurement uncertainty on the derived quantities, the systematic characterisation of repeatability and reproducibility of the fiducial-point extraction and of the derived indices, and an inter-device comparison between the developed prototype and commercial optical front-ends, in order to establish the transferability of the results across different hardware platforms.

A second direction concerns the integration of the APG analysis into existing consumer wearable devices. Since the green channel already used by commercial smartwatches preserves a usable APG signal at the wrist, the proposed pipeline could be deployed without modifications to the optical front-end, enabling large-scale, longitudinal vascular aging screening in real-world conditions. A natural extension would be the estimation of pulse transit time between wrist and finger sensors, which could open the way to continuous, cuff-less blood pressure monitoring.

Finally, a third area of development involves expanding the clinical validation to larger and more balanced cohorts, in which the individual contributions of hypertension, diabetes and other risk factors to the APG indices can be better isolated. The combination of APG indices with additional PPG-derived features within a machine learning framework represents a promising step to improve the discriminative power observed with single indices.

Within these perspectives, this thesis is intended as a methodological foundation rather than a final answer: by combining in vitro mechanical validation, morphological signal analysis, multi-wavelength optimisation and clinical-group discrimination, it provides a structured framework on which future investigations can build to bring PPG-based vascular monitoring closer to its full translational potential.

List of Publications

Peer-reviewed Articles

- **G. Diana**, F. Scardulla, S. Puleo, S. Pasta, and L. D'Acquisto, "Non-Invasive Estimation of Arterial Stiffness Using Photoplethysmography Sensors: An In Vitro Approach," *Sensors*, vol. 25, no. 11, p. 3301, 2025, doi: 10.3390/s25113301.
- F. Scardulla, G. Cosoli, C. Gnoffo, L. Antognoli, F. Bongiorno, **G. Diana**, L. Scalise, L. D'Acquisto, and M. Arnesano, "Experimental Analysis on the Effect of Contact Pressure and Activity Level as Influencing Factors in PPG Sensor Performance," *Sensors*, vol. 25, no. 14, p. 4477, 2025, doi: 10.3390/s25144477.
- S. Puleo, **G. Diana**, C. Livolsi, L. Nioi, N. Cuscino, F. Scardulla, S. Pasta, and L. D'Acquisto, "Non-Invasive Monitoring of Transcatheter Heart Valve Using Photoplethysmography and Machine Learning," *Artificial Organs*, vol. 50, no. 4, pp. 543–549, 2026, doi: 10.1111/aor.70069.
- **G. Diana**, C. Otesteanu, G. Longo, F. Scardulla, S. Puleo, L. D'Acquisto, and C. Menon, "Comparison of Multi-Wavelength PPG at Wrist and Finger for Non-Invasive Vascular Aging Assessment Using APG Analysis," *Submitted*.
- **G. Diana**, C. Otesteanu, F. Scardulla, S. Pasta, L. D'Acquisto, and C. Menon, "Photoplethysmography Acceleration Indices as Digital Biomarkers of Cardiometabolic Health," *Submitted***.**
- **G. Diana**, G. Longo, R. Liguori, A. Rubino, F. Scardulla, and L. D'Acquisto, "The Role of the Acceleration Plethysmography (APG) Signal for Vascular Aging Analysis with a Modular High-Sampling-Rate Wristband," *IEEE Sensors Letters*, *Submitted*.

Conference Papers and Proceedings

- F. Scardulla, C. Riggi, **G. Diana**, and L. D'Acquisto, "Preliminary Analysis on the Effect of Skin Temperature on Photoplethysmographic Signal," in *Proc. 2024 IEEE Int. Workshop on Metrology for Living Environment (MetroLivEnv)*, Chania, Greece, 2024, pp. 6–10, doi: 10.1109/MetroLivEnv60384.2024.10615655.
- **G. Diana**, F. Scardulla, S. Puleo, S. Pasta, and L. D'Acquisto, "A Preliminary Study on Arterial Stiffness Assessment Using Photoplethysmographic Sensors," *Engineering Proceedings*, vol. 82, no. 1, p. 80, 2024, doi: 10.3390/ecsa-11-20455.

- S. Puleo, **G. Diana**, S. Pasta, F. Scardulla, and L. D'Acquisto, "Sensor-Based Bioprosthetic Valve Monitoring: Numerical Simulation and Experimental Design," in *Design Tools and Methods in Industrial Engineering IV (ADM 2024)*, P. Di Stefano, F. Gherardini, V. Nigrelli, C. Rizzi, G. Sequenzia, and D. Tumino, Eds., Lecture Notes in Mechanical Engineering. Cham, Switzerland: Springer, 2025, doi: 10.1007/978-3-031-76594-0_6.
- F. Scardulla, G. Cosoli, L. Antognoli, C. Gnoffo, **G. Diana**, L. Scalise, L. D'Acquisto, and M. Arnesano, "Experimental Analysis on the Effect of Contact Pressure, Activity Level, and Skin Tone as Influencing Factors in PPG Sensors Performance," in *Proc. 2025 IEEE Int. Workshop on Metrology for Living Environment (MetroLivEnv)*, Venezia, Italy, 2025, pp. 1–5, doi: 10.1109/MetroLivEnv64961.2025.11106958.
- **G. Diana**, F. Scardulla, S. Pasta, and L. D'Acquisto, "Analysis of the Second Derivative of the PPG Signal as Indicator of Vascular Aging," *Engineering Proceedings*, vol. 118, no. 1, p. 72, 2025, doi: 10.3390/ECSA-12-26557.
- C. Otesteanu, **G. Diana**, F. Scardulla, S. Puleo, S. Pasta, L. D'Acquisto, and C. Menon, "Machine Learning for Classifying Vascular Age Using the Second Derivative of the PPG Signal," in *Proc. 2025 6th Int. Conf. on Communications, Information, Electronic and Energy Systems (CIEES)*, Ruse, Bulgaria, 2025, pp. 1–4, doi: 10.1109/CIEES66347.2025.11300216.

Bibliography

1. Toro, E.F. The Cardiovascular System. *Computational Bodily Fluid Dynamics* **2025**, 3–38, doi:10.1007/978-3-031-92598-6_1.
2. Buckberg, G.D.; Nanda, N.C.; Nguyen, C.; Kocica, M.J. What Is the Heart? Anatomy, Function, Pathophysiology, and Misconceptions. *Journal of Cardiovascular Development and Disease 2018, Vol. 5, Page 33* **2018**, *5*, 33, doi:10.3390/JCDD5020033.
3. Olshansky, B.; Ricci, F.; Fedorowski, A. Importance of Resting Heart Rate. *Trends Cardiovasc. Med.* **2023**, *33*, 502–515, doi:10.1016/J.TCM.2022.05.006.
4. How the Heart Works - What the Heart Looks Like | NHLBI, NIH Available online: https://www.nhlbi.nih.gov/health/heart/anatomy (accessed on 3 April 2026).
5. Sánchez-Molina, D.; García-Vilana, S.; Llumà, J.; Galtés, I.; Velázquez-Ameijide, J.; Rebollo-Soria, M.C.; Arregui-Dalmases, C. Mechanical Behavior of Blood Vessels: Elastic and Viscoelastic Contributions. *Biology 2021, Vol. 10, Page 831* **2021**, *10*, 831, doi:10.3390/BIOLOGY10090831.
6. Nwokoye, P.N.; Abilez, O.J. Blood Vessels in a Dish: The Evolution, Challenges, and Potential of Vascularized Tissues and Organoids. *Front. Cardiovasc. Med.* **2024**, *11*, 1336910, doi:10.3389/FCVM.2024.1336910/FULL.
7. Mei, C.C.; Zhang, J.; Jing, H.X. Fluid Mechanics of Windkessel Effect. *Medical & Biological Engineering & Computing 2018 56:8* **2018**, *56*, 1357–1366, doi:10.1007/S11517-017-1775-Y.
8. Camasão, D.B.; Mantovani, D. The Mechanical Characterization of Blood Vessels and Their Substitutes in the Continuous Quest for Physiological-Relevant Performances. A Critical Review. *Mater. Today Bio* **2021**, *10*, 100106, doi:10.1016/J.MTBIO.2021.100106.
9. Kesava Reddy, G. AGE-Related Cross-Linking of Collagen Is Associated with Aortic Wall Matrix Stiffness in the Pathogenesis of Drug-Induced Diabetes in Rats. *Microvasc. Res.* **2004**, *68*, 132–142, doi:10.1016/J.MVR.2004.04.002.
10. Ebrahimi, A.P. Mechanical Properties of Normal and Diseased Cerebrovascular System. *J. Vasc. Interv. Neurol.* **2009**, *2*, 155.
11. Kamml, J.; Acevedo, C.; Kammer, D.S. Advanced-Glycation Endproducts: How Cross-Linking Properties Affect the Collagen Fibril Behavior. *J. Mech. Behav. Biomed. Mater.* **2023**, *148*, 106198, doi:10.1016/J.JMBBM.2023.106198.

12. Ciavarella, C.; Motta, I.; Capri, M.; Gargiulo, M.; Pasquinelli, G. Heterogeneity and Differentiation of the Human Arterial Tree: Focus on MicroRNA Expression in Vascular Disease. *Biomolecules 2024, Vol. 14, Page 343* **2024**, *14*, 343, doi:10.3390/BIOM14030343.
13. Cocciolone, A.J.; Hawes, J.Z.; Staiculescu, M.C.; Johnson, E.O.; Murshed, M.; Wagenseil, J.E. Elastin, Arterial Mechanics, and Cardiovascular Disease. *https://doi.org/10.1152/ajpheart.00087.2018* **2018**, *315*, H189–H205, doi:10.1152/AJPHEART.00087.2018.
14. Herzog, M.J.; Müller, P.; Lechner, K.; Stiebler, M.; Arndt, P.; Kunz, M.; Ahrens, D.; Schmeißer, A.; Schreiber, S.; Braun-Dullaeus, R.C. Arterial Stiffness and Vascular Aging: Mechanisms, Prevention, and Therapy. *Signal Transduction and Targeted Therapy 2025 10:1* **2025**, *10*, 282-, doi:10.1038/s41392-025-02346-0.
15. Xuereb, R.A.; Magri, C.J.; Xuereb, R.G. Arterial Stiffness and Its Impact on Cardiovascular Health. *Curr. Cardiol. Rep.* **2023**, *25*, 1337–1349, doi:10.1007/S11886-023-01951-1/FIGURES/3.
16. Kim, H.L. Arterial Stiffness and Hypertension. *Clinical Hypertension 2023 29:1* **2023**, *29*, 31-, doi:10.1186/S40885-023-00258-1.
17. Cecelja, M.; Chowienczyk, P. Role of Arterial Stiffness in Cardiovascular Disease. *JRSM Cardiovasc. Dis.* **2012**, *1*, cvd.2012.012016, doi:10.1258/CVD.2012.012016.
18. Nichols, W.W.; Denardo, S.J.; Wilkinson, I.B.; McEniery, C.M.; Cockcroft, J.; O'Rourke, M.F. Effects of Arterial Stiffness, Pulse Wave Velocity, and Wave Reflections on the Central Aortic Pressure Waveform. *J. Clin. Hypertens.* **2008**, *10*, 295–303, doi:10.1111/J.1751-7176.2008.04746.X;WGROUP:STRING:PUBLICATION.
19. Yuen, C.; Devlin, A.M.; Bernatchez, P. Exploring Pulse Wave Velocity as a Vascular Hemodynamic Stress Marker: More than Just Arterial Stiffening? *https://doi.org/10.1152/ajpheart.00638.2025* **2026**, *330*, H243–H252, doi:10.1152/AJPHEART.00638.2025.
20. Staef, M.; Ott, C.; Kannenkeril, D.; Striepe, K.; Schiffer, M.; Schmieder, R.E.; Bosch, A. Determinants of Arterial Stiffness in Patients with Type 2 Diabetes Mellitus: A Cross Sectional Analysis. *Scientific Reports 2023 13:1* **2023**, *13*, 8944-, doi:10.1038/s41598-023-35589-4.
21. Zuo, J.; Hu, Y.; Chang, G.; Chu, S. li; Tan, I.; Butlin, M.; Avolio, A. Relationship between Arterial Stiffness and Chronic Kidney Disease in Patients with Primary

Hypertension. *Journal of Human Hypertension 2019 34:8* **2019**, *34*, 577–585, doi:10.1038/s41371-019-0275-y.

22. Sakuragi, S.; Abhayaratna, W.P. Arterial Stiffness: Methods of Measurement, Physiologic Determinants and Prediction of Cardiovascular Outcomes. *Int. J. Cardiol.* **2010**, *138*, 112–118, doi:10.1016/j.ijcard.2009.04.027.
23. Pilz, N.; Heinz, V.; Ax, T.; Fesseler, L.; Patzak, A.; Bothe, T.L. Pulse Wave Velocity: Methodology, Clinical Applications, and Interplay with Heart Rate Variability. *Rev. Cardiovasc. Med.* **2024**, *25*, 266, doi:10.31083/J.RCM2507266.
24. Sequí-Domínguez, I.; Cavero-Redondo, I.; Álvarez-Bueno, C.; Pozuelo-Carrascosa, D.P.; de Arenas-Arroyo, S.N.; Martínez-Vizcaíno, V. Accuracy of Pulse Wave Velocity Predicting Cardiovascular and All-Cause Mortality. A Systematic Review and Meta-Analysis. *Journal of Clinical Medicine 2020, Vol. 9, Page 2080* **2020**, *9*, 2080, doi:10.3390/JCM9072080.
25. Xu, L.; Zhou, S.; Wang, L.; Yao, Y.; Hao, L.; Qi, L.; Yao, Y.; Han, H.; Mukkamala, R.; Greenwald, S.E. Improving the Accuracy and Robustness of Carotid-Femoral Pulse Wave Velocity Measurement Using a Simplified Tube-Load Model. *Scientific Reports 2022 12:1* **2022**, *12*, 5147-, doi:10.1038/s41598-022-09256-z.
26. Pavey, H.; Wood, A.; Mceniery, C.M.; AlGhatrif, M.; Arshi, B.; Brunner, E.; Chen, C.H.; Cheng, H.M.; Hansen, T.W.; Ikram, M.K.; et al. Association between Carotid-Femoral Pulse Wave Velocity and Cardiovascular Disease in Individuals with Moderate Blood Pressure: A Systematic Review and Individual Participant Meta-Analysis. *BMJ Open* **2025**, *15*, e101368, doi:10.1136/BMJOPEN-2025-101368.
27. Salvi, P.; Valbusa, F.; Kearney-Schwartz, A.; Labat, C.; Grillo, A.; Parati, G.; Benetos, A. Non-Invasive Assessment of Arterial Stiffness: Pulse Wave Velocity, Pulse Wave Analysis and Carotid Cross-Sectional Distensibility: Comparison between Methods. *Journal of Clinical Medicine 2022, Vol. 11, Page 2225* **2022**, *11*, 2225, doi:10.3390/JCM11082225.
28. Fiori, G.; Fuiano, F.; Scorza, A.; Conforto, S.; Sciuto, S.A. Non-Invasive Methods for PWV Measurement in Blood Vessel Stiffness Assessment. *IEEE Rev. Biomed. Eng.* **2022**, *15*, 169–183, doi:10.1109/RBME.2021.3092208.
29. Xiao, H.; Butlin, M.; Tan, I.; Avolio, A. Effects of Cardiac Timing and Peripheral Resistance on Measurement of Pulse Wave Velocity for Assessment of Arterial Stiffness. *Sci. Rep.* **2017**, *7*, doi:10.1038/S41598-017-05807-X.

30. Ma, Y.; Choi, J.; Hourlier-Fargette, A.; Xue, Y.; Chung, H.U.; Lee, J.Y.; Wang, X.; Xie, Z.; Kang, D.; Wang, H.; et al. Relation between Blood Pressure and Pulse Wave Velocity for Human Arteries. *Proc. Natl. Acad. Sci. U. S. A.* **2018**, *115*, 11144–11149, doi:10.1073/PNAS.1814392115;WGROUP:STRING:PUBLICATION.
31. Mynard, J.P.; Kondiboyina, A.; Kowalski, R.; Cheung, M.M.H.; Smolich, J.J. Measurement, Analysis and Interpretation of Pressure/Flow Waves in Blood Vessels. *Front. Physiol.* **2020**, *11*, 564252, doi:10.3389/FPHYS.2020.01085/FULL.
32. Newman, D.L.; Greenwald, S.E. Validity of the Moens-Korteweg Equation. *The Arterial System* **1978**, 109–115, doi:10.1007/978-3-642-67020-6_10.
33. Brennan, E.G.; O'Hare, N.J.; Walsh, M.J. Transventricular Pressure-Velocity Wave Propagation in Diastole: Adherence to the Moens-Korteweg Equation. *Physiol. Meas.* **1998**, *19*, 117, doi:10.1088/0967-3334/19/1/011.
34. Ogden, R.W. Anisotropy and Nonlinear Elasticity in Arterial Wall Mechanics. *CISM International Centre for Mechanical Sciences, Courses and Lectures* **2009**, *508*, 179–258, doi:10.1007/978-3-211-95875-9_3.
35. Mesin, L.; Floris, L.; Policastro, P.; Albani, S.; Scacciatella, P.; Pugliese, N.; Masi, S.; Grillo, A.; Fabris, B.; Antonini-Canterin, F. Estimation of Aortic Stiffness with Bramwell–Hill Equation: A Comparative Analysis with Carotid–Femoral Pulse Wave Velocity. *Bioengineering 2022, Vol. 9, Page 265* **2022**, *9*, 265, doi:10.3390/BIOENGINEERING9070265.
36. Westenberg, J.J.M.; Van Poelgeest, E.P.; Steendijk, P.; Grotenhuis, H.B.; Jukema, J.W.; De Roos, A. Bramwell-Hill Modeling for Local Aortic Pulse Wave Velocity Estimation: A Validation Study with Velocity-Encoded Cardiovascular Magnetic Resonance and Invasive Pressure Assessment. *Journal of Cardiovascular Magnetic Resonance* **2012**, *14*, 2-, doi:10.1186/1532-429X-14-2.
37. van Hout, M.J.; Dekkers, I.A.; Westenberg, J.J.; Schalij, M.J.; Widya, R.L.; de Mutsert, R.; Rosendaal, F.R.; de Roos, A.; Jukema, J.W.; Scholte, A.J.; et al. Normal and Reference Values for Cardiovascular Magnetic Resonance-Based Pulse Wave Velocity in the Middle-Aged General Population. *Journal of Cardiovascular Magnetic Resonance* **2021**, *23*, 46, doi:10.1186/S12968-021-00739-Y.
38. Voges, I.; Jerosch-Herold, M.; Hedderich, J.; Pardun, E.; Hart, C.; Gabbert, D.D.; Hansen, J.H.; Petko, C.; Kramer, H.H.; Rickers, C. Normal Values of Aortic Dimensions, Distensibility, and Pulse Wave Velocity in Children and Young Adults: A

Cross-Sectional Study. *Journal of Cardiovascular Magnetic Resonance* **2012**, *14*, 41, doi:10.1186/1532-429X-14-77.

39. Jarvis, K.; Scott, M.B.; Soulat, G.; Elbaz, M.S.M.; Barker, A.J.; Carr, J.C.; Markl, M.; Ragin, A. Aortic Pulse Wave Velocity Evaluated by 4D Flow MRI across the Adult Lifespan. *J. Magn. Reson. Imaging* **2022**, *56*, 464, doi:10.1002/JMRI.28045.
40. McCarthy, C.P.; Bruno, R.M.; Brouwers, S.; Canavan, M.D.; Ceconi, C.; Christodorescu, R.M.; Daskalopoulou, S.S.; Ferro, C.J.; Gerdts, E.; Hanssen, H.; et al. 2024 ESC Guidelines for the Management of Elevated Blood Pressure and Hypertension: Developed by the Task Force on the Management of Elevated Blood Pressure and Hypertension of the European Society of Cardiology (ESC) and Endorsed by the European Society…. *Eur. Heart J.* **2024**, *45*, 3912–4018, doi:10.1093/EURHEARTJ/EHAE178.
41. Hofmann, B.; Riemer, M.; Erbs, C.; Plehn, A.; Navarrete Santos, A.; Wienke, A.; Silber, R.E.; Simm, A. Carotid to Femoral Pulse Wave Velocity Reflects the Extent of Coronary Artery Disease. *The Journal of Clinical Hypertension* **2014**, *16*, 629, doi:10.1111/JCH.12382.
42. Cheng, H.M.; Chen, C.H. Measuring Arterial Stiffness in Clinical Practice: Moving One Step Forward. *J. Clin. Hypertens.* **2020**, *22*, 1824–1826, doi:10.1111/JCH.13965;PAGEGROUP:STRING:PUBLICATION.
43. Badhwar, S.; Marais, L.; Khettab, H.; Poli, F.; Li, Y.; Segers, P.; Aasmul, S.; De Melis, M.; Baets, R.; Greenwald, S.; et al. Clinical Validation of Carotid-Femoral Pulse Wave Velocity Measurement Using a Multi-Beam Laser Vibrometer: The CARDIS Study. *Hypertension* **2024**, *81*, 1986, doi:10.1161/HYPERTENSIONAHA.124.22729.
44. Niwińska, M.M.; Chlabicz, S. Evaluation of Arterial Stiffness Parameters Measurement With Noninvasive Methods—A Systematic Review. *Cardiol. Res. Pract.* **2024**, *2024*, 4944517, doi:10.1155/CRP/4944517.
45. Hertzman, A.B. Photoelectric Plethysmography of the Fingers and Toes in Man. *Proceedings of the Society for Experimental Biology and Medicine* **1937**, *37*, 529–534, doi:10.3181/00379727-37-9630.
46. Hertzman, A.B.; Dillon, J.B. Applications of Photoelectric Plethysmography in Peripheral Vascular Disease. *Am. Heart J.* **1940**, *20*, 750–761, doi:10.1016/S0002-8703(40)90534-8.

47. Kyriacou, P.A. Introduction to Photoplethysmography. *Photoplethysmography: Technology, Signal Analysis and Applications* **2022**, 1–16, doi:10.1016/B978-0-12-823374-0.00001-3.
48. Severinghaus, J.W. Takuo Aoyagi: Discovery of Pulse Oximetry. *Anesth. Analg.* **2007**, *105*, S1, doi:10.1213/01.ANE.0000269514.31660.09.
49. Hertzman, A.B.; Randall, W.C.; Jochim, K.E. The Estimation of the Cutaneous Blood Flow with the Photoelectric Plethysmograph. *https://doi.org/10.1152/ajplegacy.1946.145.5.716* **1946**, *145*, 716–726, doi:10.1152/AJPLEGACY.1946.145.5.716.
50. Miyasaka, K.; Shelley, K.; Takahashi, S.; Kubota, H.; Ito, K.; Yoshiya, I.; Yamanishi, A.; Cooper, J.B.; Steward, D.J.; Nishida, H.; et al. Tribute to Dr. Takuo Aoyagi, Inventor of Pulse Oximetry. *Journal of Anesthesia 2021 35:5* **2021**, *35*, 671–709, doi:10.1007/S00540-021-02967-Z.
51. Cecil, W.T.; Thorpe, K.J.; Fibuch, E.E.; Tuohy, G.F. A Clinical Evaluation of the Accuracy of the Nellcor N-100 and Ohmeda 3700 Pulse Oximeters. *J. Clin. Monit.* **1988**, *4*, 31–36, doi:10.1007/BF01618105/METRICS.
52. Khanna, A.K.; Banga, A.; Rigdon, J.; White, B.N.; Cuvillier, C.; Ferraz, J.; Olsen, F.; Hackett, L.; Bansal, V.; Kaw, R. Role of Continuous Pulse Oximetry and Capnography Monitoring in the Prevention of Postoperative Respiratory Failure, Postoperative Opioid-Induced Respiratory Depression and Adverse Outcomes on Hospital Wards: A Systematic Review and Meta-Analysis. *J. Clin. Anesth.* **2024**, *94*, 111374, doi:10.1016/J.JCLINANE.2024.111374.
53. Charlton, P.H.; Allen, J.; Bailón, R.; Baker, S.; Behar, J.A.; Chen, F.; Clifford, G.D.; Clifton, D.A.; Davies, H.J.; Ding, C.; et al. The 2023 Wearable Photoplethysmography Roadmap. *Physiol. Meas.* **2023**, *44*, 111001, doi:10.1088/1361-6579/ACEAD2.
54. Park, J.; Seok, H.S.; Kim, S.S.; Shin, H. Photoplethysmogram Analysis and Applications: An Integrative Review. *Front. Physiol.* **2022**, *12*, 808451, doi:10.3389/FPHYS.2021.808451/FULL.
55. Ebrahimi, Z.; Gosselin, B. Ultralow-Power Photoplethysmography (PPG) Sensors: A Methodological Review. *IEEE Sens. J.* **2023**, *23*, 16467–16480, doi:10.1109/JSEN.2023.3284818.
56. Ray, D.; Collins, T.; Woolley, S.; Ponnapalli, P. A Review of Wearable Multi-Wavelength Photoplethysmography. *IEEE Rev. Biomed. Eng.* **2023**, *16*, 136–151, doi:10.1109/RBME.2021.3121476.

57. Lee, J.; Kim, M.; Park, H.K.; Kim, I.Y. Motion Artifact Reduction in Wearable Photoplethysmography Based on Multi-Channel Sensors with Multiple Wavelengths. *Sensors 2020, Vol. 20, Page 1493* **2020**, *20*, 1493, doi:10.3390/S20051493.
58. Marouf, H.; Abdel-Salam, N.; El-Rabaie, E.S.M.; Rashed, A.N.Z.; ElKhamisy, K.M. A Comprehensive Review Of Photodetectors: Materials, Enhancement Techniques, Perspectives, and Recent Directions. *Journal of Optics 2025* **2025**, 1–23, doi:10.1007/S12596-025-02779-4.
59. Mohan, N.; Awwad, F.; Albastaki, N.; Atef, M. A Low-Power High-Sensitivity Photocurrent Sensory Circuit with Capacitive Feedback Transimpedance for Photoplethysmography Sensing. *Sensors 2024, Vol. 24, Page 4097* **2024**, *24*, 4097, doi:10.3390/S24134097.
60. Jeong, I.; Jun, S.; Um, D.; Oh, J.; Yoon, H. Non-Invasive Estimation of Systolic Blood Pressure and Diastolic Blood Pressure Using Photoplethysmograph Components. *Yonsei Med. J.* **2010**, *51*, 345–353, doi:10.3349/YMJ.2010.51.3.345.
61. Sukesh Rao, M.; Hegde, R.B.; Bangera, S.C. A Comparative Analysis of Reflective and Transmissive PPG Sensor in Pulse Acquisition System. *2023 International Conference on Computer, Electronics and Electrical Engineering and their Applications, IC2E3 2023* **2023**, doi:10.1109/IC2E357697.2023.10262473.
62. Saritas, T.; Greber, R.; Venema, B.; Puelles, V.G.; Ernst, S.; Blazek, V.; Floege, J.; Leonhardt, S.; Schlieper, G. Non-Invasive Evaluation of Coronary Heart Disease in Patients with Chronic Kidney Disease Using Photoplethysmography. *Clin. Kidney J.* **2019**, *12*, 538–545, doi:10.1093/CKJ/SFY135.
63. Lin, Q.; Sijbers, W.; Avidikou, C.; Van Hoof, C.; Tavernier, F.; Van Helleputte, N. Photoplethysmography (PPG) Sensor Circuit Design Techniques. *Proceedings of the Custom Integrated Circuits Conference* **2022**, *2022-April*, doi:10.1109/CICC53496.2022.9772851.
64. Guan, Y.; Zhang, H.; Chen, B. Design of Smart Watch Based on STM32. *Proceedings - 2024 10th International Conference on Systems and Informatics, ICSAI 2024* **2024**, doi:10.1109/ICSAI65059.2024.10893813.
65. Chettri, N.; Aprile, A.; Bonizzoni, E.; Malcovati, P. Advances in PPG Sensors Data Acquisition with Light-to-Digital Converters: A Review. *IEEE Sens. J.* **2024**, *24*, 25261–25274, doi:10.1109/JSEN.2024.3420170.
66. Kiteto, M.K.; Mecha, C.A. Insight into the Bouguer-Beer-Lambert Law: A Review. *Sustainable Chemical Engineering* **2024**, 567–587, doi:10.37256/SCE.5220245325.

67. Mayerhöfer, T.G.; Pahlow, S.; Popp, J. The Bouguer-Beer-Lambert Law: Shining Light on the Obscure. *Chemphyschem* **2020**, *21*, 2029–2046, doi:10.1002/CPHC.202000464;WEBSITE:WEBSITE:CHEMISTRY-EUROPE;WGROUP:STRING:PUBLICATION.
68. Oshina, I.; Spigulis, J. Beer–Lambert Law for Optical Tissue Diagnostics: Current State of the Art and the Main Limitations. *J. Biomed. Opt.* **2021**, *26*, 100901, doi:10.1117/1.JBO.26.10.100901.
69. Mayerhöfer, T.G.; Pipa, A. V.; Popp, J. Beer's Law-Why Integrated Absorbance Depends Linearly on Concentration. *Chemphyschem* **2019**, *20*, 2748, doi:10.1002/CPHC.201900787.
70. Leppänen, T.; Kainulainen, S.; Korkalainen, H.; Sillanmäki, S.; Kulkas, A.; Töyräs, J.; Nikkonen, S. Pulse Oximetry: The Working Principle, Signal Formation, and Applications. *Adv. Exp. Med. Biol.* **2022**, *1384*, 205–218, doi:10.1007/978-3-031-06413-5_12/TABLES/1.
71. Kyriacou, P.; Budidha, K.; Abay, T.Y. Optical Techniques for Blood and Tissue Oxygenation. *Encyclopedia of Biomedical Engineering* **2019**, *1–3*, 461–472, doi:10.1016/B978-0-12-801238-3.10886-4.
72. Douplik, A.; Saiko, G.; Schelkanova, I.; Tuchin, V. V. The Response of Tissue to Laser Light. *Lasers for Medical Applications: Diagnostics, Therapy and Surgery* **2013**, 47–109, doi:10.1533/9780857097545.1.47.
73. Liu, P.; Zhu, Z.; Zeng, C.; Nie, G. Specific Absorption Spectra of Hemoglobin at Different PO2 Levels: Potential Noninvasive Method to Detect PO2 in Tissues. *J. Biomed. Opt.* **2012**, *17*, 125002, doi:10.1117/1.JBO.17.12.125002.
74. Nolte, D.D. Coherent Light Scattering from Cellular Dynamics in Living Tissues. *Reports on Progress in Physics* **2024**, *87*, 036601, doi:10.1088/1361-6633/AD2229.
75. Ash, C.; Dubec, M.; Donne, K.; Bashford, T. Effect of Wavelength and Beam Width on Penetration in Light-Tissue Interaction Using Computational Methods. *Lasers in Medical Science 2017 32:8* **2017**, *32*, 1909–1918, doi:10.1007/S10103-017-2317-4.
76. Mejía-Mejía, E.; Allen, J.; Budidha, K.; El-Hajj, C.; Kyriacou, P.A.; Charlton, P.H. Photoplethysmography Signal Processing and Synthesis. *Photoplethysmography: Technology, Signal Analysis and Applications* **2022**, 69–146, doi:10.1016/B978-0-12-823374-0.00015-3.
77. Hess, D.R. Pulse Oximetry: 2023 Year in Review. *Respir. Care* **2024**, *69*, 1033, doi:10.4187/RESPCARE.12023.

78. Coste, A.; Millour, G.; Hausswirth, C. A Comparative Study Between ECG- and PPG-Based Heart Rate Sensors for Heart Rate Variability Measurements: Influence of Body Position, Duration, Sex, and Age. *Sensors 2025, Vol. 25, Page 5745* **2025**, *25*, 5745, doi:10.3390/S25185745.
79. Pankaj; Maan, P.; Kumar, M.; Kumar, A.; Komaragiri, R. Cuffless Monitoring of Blood Pressure Using Photoplethysmography Signal: A Comprehensive Review of Artificial Intelligence and Edge Computing Solutions. *Archives of Computational Methods in Engineering 2025 33:3* **2025**, *33*, 3837–3866, doi:10.1007/S11831-025-10415-4.
80. El-Hajj, C.; Kyriacou, P.A. Cuffless Blood Pressure Estimation from PPG Signals and Its Derivatives Using Deep Learning Models. *Biomed. Signal Process. Control* **2021**, *70*, 102984, doi:10.1016/J.BSPC.2021.102984.
81. Chen, G.; Zou, L.; Ji, Z. A Review: Blood Pressure Monitoring Based on PPG and Circadian Rhythm. *APL Bioeng.* **2024**, *8*, 31501, doi:10.1063/5.0206980/3304394.
82. Allen, J. Photoplethysmography for the Assessment of Peripheral Vascular Disease. *Photoplethysmography: Technology, Signal Analysis and Applications* **2022**, 189–235, doi:10.1016/B978-0-12-823374-0.00005-0.
83. Shabani Varaki, E.; Gargiulo, G.D.; Penkala, S.; Breen, P.P. Peripheral Vascular Disease Assessment in the Lower Limb: A Review of Current and Emerging Non-Invasive Diagnostic Methods. *Biomed. Eng. Online* **2018**, *17*, 61, doi:10.1186/S12938-018-0494-4.
84. Ferizoli, R.; Karimpour, P.; May, J.M.; Kyriacou, P.A. Arterial Stiffness Assessment Using PPG Feature Extraction and Significance Testing in an in Vitro Cardiovascular System. *Scientific Reports 2024 14:1* **2024**, *14*, 2024-, doi:10.1038/s41598-024-51395-y.
85. Karimpour, P.; May, J.M.; Kyriacou, P.A. Photoplethysmography for the Assessment of Arterial Stiffness. *Sensors 2023, Vol. 23, Page 9882* **2023**, *23*, 9882, doi:10.3390/S23249882.
86. Karimpour, P.; Ferizoli, R.; May, J.M.; Kyriacou, P.A. Multimodal Assessment of Arterial Stiffness Using Photoplethysmography and Laser Doppler Flowmetry. *npj Cardiovascular Health 2026 3:1* **2026**, *3*, 19-, doi:10.1038/s44325-026-00115-8.
87. Hellqvist, H.; Rietz, H.; Grote, L.; Hedner, J.; Sommermeyer, D.; Kahan, T.; Spaak, J. Overnight Stiffness Index from Finger Photoplethysmography in Relation to Markers

of Cardiovascular Risk and Vascular Ageing. *Heart and Vessels 2025 40:10* **2025**, *40*, 895–904, doi:10.1007/S00380-025-02537-3.

88. Iqbal, T.; Elahi, A.; Ganly, S.; Wijns, W.; Shahzad, A. Photoplethysmography-Based Respiratory Rate Estimation Algorithm for Health Monitoring Applications. *Journal of Medical and Biological Engineering 2022 42:2* **2022**, *42*, 242–252, doi:10.1007/S40846-022-00700-Z.
89. Sharma, N.K.; Shahid, S.; Kumar, S.; Sharma, S.; Gupta, T.; Gupta, R.K.; Kumar, N. Assessing Depth of Anesthesia Using PPG Signals. *Lecture Notes in Networks and Systems* **2025**, *5588 LNNS*, 423–435, doi:10.1007/978-981-96-1918-4_29/FIGURES/2.
90. Kim, K.B.; Baek, H.J. Photoplethysmography in Wearable Devices: A Comprehensive Review of Technological Advances, Current Challenges, and Future Directions. *Electronics 2023, Vol. 12, Page 2923* **2023**, *12*, 2923, doi:10.3390/ELECTRONICS12132923.
91. Lapitan, D.G.; Rogatkin, D.A.; Molchanova, E.A.; Tarasov, A.P. Estimation of Phase Distortions of the Photoplethysmographic Signal in Digital IIR Filtering. *Scientific Reports 2024 14:1* **2024**, *14*, 6546-, doi:10.1038/s41598-024-57297-3.
92. Liang, Y.; Elgendi, M.; Chen, Z.; Ward, R. Analysis: An Optimal Filter for Short Photoplethysmogram Signals. *Sci. Data* **2018**, *5*, 180076-, doi:10.1038/SDATA.2018.76;SUBJMETA.
93. Mejía-Mejía, E.; Kyriacou, P.A. Effects of Noise and Filtering Strategies on the Extraction of Pulse Rate Variability from Photoplethysmograms. *Biomed. Signal Process. Control* **2023**, *80*, 104291, doi:10.1016/J.BSPC.2022.104291.
94. Liao, S.; Liu, H.; Lin, W.H.; Zheng, D.; Chen, F. Filtering-Induced Changes of Pulse Transmit Time across Different Ages: A Neglected Concern in Photoplethysmography-Based Cuffless Blood Pressure Measurement. *Front. Physiol.* **2023**, *14*, 1172150, doi:10.3389/FPHYS.2023.1172150/TEXT.
95. Allen, J. Photoplethysmography and Its Application in Clinical Physiological Measurement. *Physiol. Meas.* **2007**, *28*, doi:10.1088/0967-3334/28/3/R01.
96. Abdrasulova, N.; Aleksanyan, M.; Kim, M.J.; Ahn, J.M. Butterworth Filtering at 500 Hz Optimizes PPG-Based Heart Rate Variability Analysis for Wearable Devices: A Comparative Study. *Sensors 2025, Vol. 25, Page 7091* **2025**, *25*, 7091, doi:10.3390/S25227091.

97. Han, D.; Bashar, S.K.; Lázaro, J.; Mohagheghian, F.; Peitzsch, A.; Nishita, N.; Ding, E.; Dickson, E.L.; Dimezza, D.; Scott, J.; et al. A Real-Time PPG Peak Detection Method for Accurate Determination of Heart Rate during Sinus Rhythm and Cardiac Arrhythmia. *Biosensors 2022, Vol. 12, Page 82* **2022**, *12*, 82, doi:10.3390/BIOS12020082.
98. Chakraborty, A.; Sadhukhan, D.; Mitra, M. Efficient and Lightweight Detection of PPG Onset and Systolic Peaks Using Implementable Time-Domain Strategies. *Measurement* **2022**, *200*, 111628, doi:10.1016/J.MEASUREMENT.2022.111628.
99. Kazemi, K.; Laitala, J.; Azimi, I.; Liljeberg, P.; Rahmani, A.M. Robust PPG Peak Detection Using Dilated Convolutional Neural Networks. *Sensors 2022, Vol. 22, Page 6054* **2022**, *22*, 6054, doi:10.3390/S22166054.
100. Charlton, P.H.; Marozas, V.; Mejía-Mejía, E.; Kyriacou, P.A.; Mant, J. Determinants of Photoplethysmography Signal Quality at the Wrist. *PLOS Digital Health* **2025**, *4*, e0000585, doi:10.1371/JOURNAL.PDIG.0000585.
101. Scardulla, F.; Cosoli, G.; Gnoffo, C.; Antognoli, L.; Bongiorno, F.; Diana, G.; Scalise, L.; D'Acquisto, L.; Arnesano, M. Experimental Analysis on the Effect of Contact Pressure and Activity Level as Influencing Factors in PPG Sensor Performance. *Sensors 2025, Vol. 25, Page 4477* **2025**, *25*, 4477, doi:10.3390/S25144477.
102. Scardulla, F.; Cosoli, G.; Antognoli, L.; Gnoffo, C.; Diana, G.; Bongiorno, F.; Scalise, L.; D'Acquisto, L.; Arnesano, M. Experimental Analysis on the Effect of Contact Pressure, Activity Level, and Skin Tone as Influencing Factors in PPG Sensors Performance. *2025 IEEE International Workshop on Metrology for Living Environment, MetroLivEnv 2025 - Proceedings* **2025**, 183–187, doi:10.1109/METROLIVENV64961.2025.11106958.
103. Scardulla, F.; Riggi, C.; Diana, G.; D'Acquisto, L. Preliminary Analisys on the Effect of Skin Temperature on Photoplethysmographic Signal. *2024 IEEE International Workshop on Metrology for Living Environment, MetroLivEnv 2024 - Proceedings* **2024**, 6–10, doi:10.1109/METROLIVENV60384.2024.10615655.
104. Liu, H.; Chen, F.; Hartmann, V.; Khalid, S.G.; Hughes, S.; Zheng, D. Comparison of Different Modulations of Photoplethysmography in Extracting Respiratory Rate: From a Physiological Perspective. *Physiol. Meas.* **2020**, *41*, 094001, doi:10.1088/1361-6579/ABAAF0.
105. Zhang, C.; Wei, S.; Dong, G.; Zeng, Y.; Zhu, G.; Zhou, X.; Liu, F. Respiratory Rate Estimation from Photoplethysmogram Baseline Wandering by Harmonic Analysis and

Sequential Fusion. *Biomed. Signal Process. Control* **2025**, *100*, 107006, doi:10.1016/J.BSPC.2024.107006.

106. Abushouk, A.; Kansara, T.; Abdelfattah, O.; Badwan, O.; Hariri, E.; Chaudhury, P.; Kapadia, S.R. The Dicrotic Notch: Mechanisms, Characteristics, and Clinical Correlations. *Curr. Cardiol. Rep.* **2023**, *25*, 807–816, doi:10.1007/S11886-023-01901-X/TABLES/3.
107. Al-Halawani, R.; Charlton, P.H.; Qassem, M.; Kyriacou, P.A. A Review of the Effect of Skin Pigmentation on Pulse Oximeter Accuracy. *Physiol. Meas.* **2023**, *44*, 05TR01, doi:10.1088/1361-6579/ACD51A.
108. Fallow, B.A.; Tarumi, T.; Tanaka, H. Influence of Skin Type and Wavelength on Light Wave Reflectance. *Journal of Clinical Monitoring and Computing 2013 27:3* **2013**, *27*, 313–317, doi:10.1007/S10877-013-9436-7.
109. Teng, X.F.; Zhang, Y.T. The Effect of Contacting Force on Photoplethysmographic Signals. *Physiol. Meas.* **2004**, *25*, 1323, doi:10.1088/0967-3334/25/5/020.
110. Grabovskis, A.; Marcinkevics, Z.; Rubins, U.; Kviesis-Kipge, E. Effect of Probe Contact Pressure on the Photoplethysmographic Assessment of Conduit Artery Stiffness. *J. Biomed. Opt.* **2013**, *18*, 027004, doi:10.1117/1.JBO.18.2.027004.
111. Hartmann, V.; Liu, H.; Chen, F.; Qiu, Q.; Hughes, S.; Zheng, D. Quantitative Comparison of Photoplethysmographic Waveform Characteristics: Effect of Measurement Site. *Front. Physiol.* **2019**, *10*, 431697, doi:10.3389/FPHYS.2019.00198/TEXT.
112. Pham, H.M.; Ho, M.Y.; Zhang, Y.; Spathis, D.; Saeed, A.; Ma, D. Reliable Wrist PPG Monitoring by Mitigating Poor Skin Sensor Contact. *Scientific Reports 2025 15:1* **2025**, *15*, 45046-, doi:10.1038/s41598-025-31883-5.
113. Orphanidou, C. Signal Quality Assessment in Physiological Monitoring. **2018**, doi:10.1007/978-3-319-68415-4.
114. Pollreisz, D.; TaheriNejad, N. Detection and Removal of Motion Artifacts in PPG Signals. *Mobile Networks and Applications 2019 27:2* **2019**, *27*, 728–738, doi:10.1007/S11036-019-01323-6.
115. Jarchi, D.; Casson, A.J. Description of a Database Containing Wrist PPG Signals Recorded during Physical Exercise with Both Accelerometer and Gyroscope Measures of Motion. *Data 2017, Vol. 2, Page 1* **2016**, *2*, 1, doi:10.3390/DATA2010001.

116. Casson, A.J.; Vazquez Galvez, A.; Jarchi, D. Gyroscope vs. Accelerometer Measurements of Motion from Wrist PPG during Physical Exercise. *ICT Express* **2016**, *2*, 175–179, doi:10.1016/J.ICTE.2016.11.003.
117. Maity, A.K.; Veeraraghavan, A.; Sabharwal, A. PPGMotion: Model-Based Detection of Motion Artifacts in Photoplethysmography Signals. *Biomed. Signal Process. Control* **2022**, *75*, 103632, doi:10.1016/J.BSPC.2022.103632.
118. Pandey, R.K.; Chao, P.C.P. External Temperature Sensor Assisted a New Low Power Photoplethysmography Readout System for Accurate Measurement of the Bio-Signs. *Microsystem Technologies 2020 27:6* **2020**, *27*, 2315–2343, doi:10.1007/S00542-020-05106-Y.
119. Jeong, I.C.; Yoon, H.; Kang, H.; Yeom, H. Effects of Skin Surface Temperature on Photoplethysmograph. *J. Healthc. Eng.* **2014**, *5*, 429–438, doi:10.1260/2040-2295.5.4.429;JOURNAL:JOURNAL:7158;ISSUE:ISSUE:DOI.
120. Cubas, P.; Prado, S. Design of a PPG Signal Acquisition Platform Robust to Ambient Light. *Smart Innovation, Systems and Technologies* **2024**, *402 SIST*, 206–216, doi:10.1007/978-3-031-66961-3_19/FIGURES/8.
121. Elgendi, M.; Liang, Y.; Ward, R. Toward Generating More Diagnostic Features from Photoplethysmogram Waveforms. *Diseases 2018, Vol. 6, Page 20* **2018**, *6*, 20, doi:10.3390/DISEASES6010020.
122. He, Z.; Zhang, H.; Chen, X.; Shi, J.; Bai, L.; Fang, Z.; Wang, R. Hemorrhagic Risk Prediction in Coronary Artery Disease Patients Based on Photoplethysmography and Machine Learning. *Scientific Reports 2022 12:1* **2022**, *12*, 19190-, doi:10.1038/s41598-022-22719-7.
123. Liu, B.; Zhang, Z.; Di, X.; Wang, X.; Xie, L.; Xie, W.; Zhang, J. The Assessment of Autonomic Nervous System Activity Based on Photoplethysmography in Healthy Young Men. *Front. Physiol.* **2021**, *12*, 733264, doi:10.3389/FPHYS.2021.733264/TEXT.
124. Takazawa, K.; Tanaka, N.; Fujita, M.; Matsuoka, O.; Saiki, T.; Aikawa, M.; Tamura, S.; Ibukiyama, C. Assessment of Vasoactive Agents and Vascular Aging by the Second Derivative of Photoplethysmogram Waveform. *Hypertension* **1998**, *32*, 365–370, doi:10.1161/01.HYP.32.2.365;ISSUE:ISSUE:DOI.
125. Abdullah, S.; Hafid, A.; Folke, M.; Lindén, M.; Kristoffersson, A. PPGFeat: A Novel MATLAB Toolbox for Extracting PPG Fiducial Points. *Front. Bioeng. Biotechnol.* **2023**, *11*, 1199604, doi:10.3389/FBIOE.2023.1199604/TEXT.

126. Filippi, F.; Fiori, G.; Bocchetta, G.; Sciuto, S.A.; Scorza, A. A Preliminary Comparison of Three Methods for the Assessment of Pulse Wave Transit Time in an Arterial Simulator. *26th IMEKO TC4 International Symposium and 24th International Workshop on ADC/DAC Modelling and Testing* **2023**, 186–189, doi:10.21014/TC4-2023.43.
127. Elgendi, M. Standard Terminologies for Photoplethysmogram Signals. *Curr. Cardiol. Rev.* **2012**, *8*, 215–219, doi:10.2174/157340312803217184.
128. Elgendi, M. On the Analysis of Fingertip Photoplethysmogram Signals. *Curr. Cardiol. Rev.* **2012**, *8*, 14–25, doi:10.2174/157340312801215782.
129. Suboh, M.Z.; Jaafar, R.; Nayan, N.A.; Harun, N.H.; Mohamad, M.S.F. Analysis on Four Derivative Waveforms of Photoplethysmogram (PPG) for Fiducial Point Detection. *Front. Public Health* **2022**, *10*, doi:10.3389/FPUBH.2022.920946.
130. Abdullah, S.; Hafid, A.; Folke, M.; Lindén, M.; Kristoffersson, A. A Novel Fiducial Point Extraction Algorithm to Detect C and D Points from the Acceleration Photoplethysmogram (CnD). *Electronics 2023, Vol. 12, Page 1174* **2023**, *12*, 1174, doi:10.3390/ELECTRONICS12051174.
131. Aguet, C.; Jorge, J.; Van Zaen, J.; Proença, M.; Bonnier, G.; Frossard, P.; Lemay, M. Blood Pressure Monitoring during Anesthesia Induction Using PPG Morphology Features and Machine Learning. *PLoS One* **2023**, *18*, e0279419, doi:10.1371/JOURNAL.PONE.0279419.
132. Elgendi, M.; Jost, E.; Alian, A.; Fletcher, R.R.; Bomberg, H.; Eichenberger, U.; Menon, C. Photoplethysmography Features Correlated with Blood Pressure Changes. *Diagnostics 2024, Vol. 14, Page 2309* **2024**, *14*, 2309, doi:10.3390/DIAGNOSTICS14202309.
133. Otsuka, T.; Kawada, T.; Katsumata, M.; Ibuki, C. Utility of Second Derivative of the Finger Photoplethysmogram for the Estimation of the Risk of Coronary Heart Disease in the General Population. *Circulation Journal* **2006**, *70*, 304–310, doi:10.1253/CIRCJ.70.304.
134. Inoue, N.; Kawakami, H.; Yamamoto, H.; Ito, C.; Fujiwara, S.; Sasaki, H.; Kihara, Y. Second Derivative of the Finger Photoplethysmogram and Cardiovascular Mortality in Middle-Aged and Elderly Japanese Women. *Hypertension Research 2017 40:2* **2016**, *40*, 207–211, doi:10.1038/hr.2016.123.
135. Tabara, Y.; Igase, M.; Okada, Y.; Nagai, T.; Miki, T.; Ohyagi, Y.; Matsuda, F.; Kohara, K. Usefulness of the Second Derivative of the Finger Photoplethysmogram for

Assessment of End-Organ Damage: The J-SHIPP Study. *Hypertension Research 2016 39:7* **2016**, *39*, 552–556, doi:10.1038/hr.2016.18.

136. Laurent, S.; Cockcroft, J.; Van Bortel, L.; Boutouyrie, P.; Giannattasio, C.; Hayoz, D.; Pannier, B.; Vlachopoulos, C.; Wilkinson, I.; Struijker-Boudier, H. Expert Consensus Document on Arterial Stiffness: Methodological Issues and Clinical Applications. *Eur. Heart J.* **2006**, *27*, 2588–2605, doi:10.1093/EURHEARTJ/EHL254.
137. Van Bortel, L.M.; Laurent, S.; Boutouyrie, P.; Chowienczyk, P.; Cruickshank, J.K.; De Backer, T.; Filipovsky, J.; Huybrechts, S.; Mattace-Raso, F.U.S.; Protogerou, A.D.; et al. Expert Consensus Document on the Measurement of Aortic Stiffness in Daily Practice Using Carotid-Femoral Pulse Wave Velocity. *J. Hypertens.* **2012**, *30*, 445–448, doi:10.1097/HJH.0B013E32834FA8B0.
138. Townsend, R.R.; Wilkinson, I.B.; Schiffrin, E.L.; Avolio, A.P.; Chirinos, J.A.; Cockcroft, J.R.; Heffernan, K.S.; Lakatta, E.G.; McEniery, C.M.; Mitchell, G.F.; et al. Recommendations for Improving and Standardizing Vascular Research on Arterial Stiffness: A Scientific Statement from the American Heart Association. *Hypertension* **2015**, *66*, 698–722, doi:10.1161/HYP.0000000000000033;WGROUP:STRING:PUBLICATION.
139. Williams, B.; Mancia, G.; Spiering, W.; Agabiti Rosei, E.; Azizi, M.; Burnier, M.; Clement, D.L.; Coca, A.; de Simone, G.; Dominiczak, A.; et al. 2018 ESC/ESH Guidelines for the Management of Arterial Hypertension: The Task Force for the Management of Arterial Hypertension of the European Society of Cardiology (ESC) and the European Society of Hypertension (ESH). *Eur. Heart J.* **2018**, *39*, 3021–3104, doi:10.1093/EURHEARTJ/EHY339.
140. Spronck, B.; Terentes-Printzios, D.; Avolio, A.P.; Boutouyrie, P.; Guala, A.; Jerončić, A.; Laurent, S.; Barbosa, E.C.D.; Baulmann, J.; Chen, C.H.; et al. 2024 Recommendations for Validation of Noninvasive Arterial Pulse Wave Velocity Measurement Devices. *Hypertension* **2024**, *81*, 183–192, doi:10.1161/HYPERTENSIONAHA.123.21618;WGROUP:STRING:PUBLICATION.
141. Valerio, A.; Buraioli, I.; Sanginario, A.; Mingrone, G.; Leone, D.; Milan, A.; Demarchi, D. A Region-Based Cross-Correlation Approach for Tonometric Carotid–Femoral Pulse Wave Velocity Assessment. *Biomed. Signal Process. Control* **2024**, *93*, 106161, doi:10.1016/J.BSPC.2024.106161.

142. Mattace-Raso, F.U.S.; Hofman, A.; Verwoert, G.C.; Wittemana, J.C.M.; Wilkinson, I.; Cockcroft, J.; McEniery, C.; Yasmina; Laurent, S.; Boutouyrie, P.; et al. Determinants of Pulse Wave Velocity in Healthy People and in the Presence of Cardiovascular Risk Factors: 'Establishing Normal and Reference Values.' *Eur. Heart J.* **2010**, *31*, 2338–2350, doi:10.1093/EURHEARTJ/EHQ165.

143. Butlin, M.; Qasem, A. Large Artery Stiffness Assessment Using SphygmoCor Technology. *Pulse* **2016**, *4*, 180, doi:10.1159/000452448.

144. Hwang, M.H.; Yoo, J.K.; Kim, H.K.; Hwang, C.L.; Mackay, K.; Hemstreet, O.; Nichols, W.W.; Christou, D.D. Validity and Reliability of Aortic Pulse Wave Velocity and Augmentation Index Determined by the New Cuff-Based SphygmoCor Xcel. *Journal of Human Hypertension 2014 28:8* **2014**, *28*, 475–481, doi:10.1038/jhh.2013.144.

145. Salvi, P.; Lio, G.; Labat, C.; Ricci, E.; Pannier, B.; Benetos, A. Validation of a New Non-Invasive Portable Tonometer for Determining Arterial Pressure Wave and Pulse Wave Velocity: The PulsePen Device. *J. Hypertens.* **2004**, *22*, 2285–2293, doi:10.1097/00004872-200412000-00010.

146. Torres, W.; Lee, E.; Laitinen, E.; Barker, A.R.; Jalanko, P.; Nurmi, T.; Bond, B.; Gao, Y.; Fernandes, R.A.; Haapala, E.A. Reproducibility and Agreement of Pulse Wave Velocity and Augmentation Index over Repeated Assessments Using Two Different Devices in Adolescents. *Clin. Physiol. Funct. Imaging* **2026**, *46*, e70049, doi:10.1111/CPF.70049.

147. Stea, F.; Bozec, E.; Millasseau, S.; Khettab, H.; Boutouyrie, P.; Laurent, S. Comparison of the Complior Analyse Device with Sphygmocor and Complior SP for Pulse Wave Velocity and Central Pressure Assessment. *J. Hypertens.* **2014**, *32*, 873–880, doi:10.1097/HJH.0000000000000091.

148. Papaioannou, T.G.; Thymis, J.; Benas, D.; Triantafyllidi, H.; Kostelli, G.; Pavlidis, G.; Kousathana, F.; Katogiannis, K.; Vlastos, D.; Lambadiari, V.; et al. Measurement of Central Augmentation Index by Three Different Methods and Techniques: Agreement among Arteriograph, Complior, and Mobil-O-Graph Devices. *The Journal of Clinical Hypertension* **2019**, *21*, 1386–1392, doi:10.1111/JCH.13654.

149. Benas, D.; Kornelakis, M.; Triantafyllidi, H.; Kostelli, G.; Pavlidis, G.; Varoudi, M.; Vlastos, D.; Lambadiari, V.; Parissis, J.; Ikonomidis, I. Pulse Wave Analysis Using the Mobil-O-Graph, Arteriograph and Complior Device: A Comparative Study. *Blood Press.* **2019**, *28*, 107–113, doi:10.1080/08037051.2018.1564236.

150. Alivon, M.; Phuong, T.V.D.; Vignon, V.; Bozec, E.; Khettab, H.; Hanon, O.; Briet, M.; Halimi, J.M.; Hallab, M.; Plichart, M.; et al. A Novel Device for Measuring Arterial Stiffness Using Finger-Toe Pulse Wave Velocity: Validation Study of the POpmètre®. *Arch. Cardiovasc. Dis.* **2015**, *108*, 227–234, doi:10.1016/J.ACVD.2014.12.003.

151. Tomiyama, H.; Shiina, K. State of the Art Review: Brachial-Ankle PWV. *J. Atheroscler. Thromb.* **2020**, *27*, 621, doi:10.5551/JAT.RV17041.

152. Stone, K.; Veerasingam, D.; Meyer, M.L.; Heffernan, K.S.; Higgins, S.; Maria Bruno, R.; Bueno, C.A.; Döerr, M.; Schmidt-Trucksäss, A.; Terentes-Printzios, D.; et al. Reimagining the Value of Brachial-Ankle Pulse Wave Velocity as a Biomarker of Cardiovascular Disease Risk - A Call to Action on Behalf of VascAgeNet. *Hypertension* **2023**, *80*, 1980–1992, doi:10.1161/HYPERTENSIONAHA.123.21314;JOURNAL:JOURNAL:HYP;PAGEGROUP:STRING:PUBLICATION.

153. Rico Martín, S.; Vassilenko, V.; De Nicolás Jiménez, J.M.; Rey Sánchez, P.; Serrano, A.; Martínez Alvarez, M.; Calderón García, J.F.; Sánchez Muñoz-Torrero, J.F. Cardio-Ankle Vascular Index (CAVI) Measured by a New Device: Protocol for a Validation Study. *BMJ Open* **2020**, *10*, e038581, doi:10.1136/BMJOPEN-2020-038581.

154. Bäck, M.; Topouchian, J.; Labat, C.; Gautier, S.; Blacher, J.; Cwynar, M.; de la Sierra, A.; Pall, D.; Duarte, K.; Fantin, F.; et al. Cardio-Ankle Vascular Index for Predicting Cardiovascular Morbimortality and Determinants for Its Progression in the Prospective Advanced Approach to Arterial Stiffness (TRIPLE-A-Stiffness) Study. *EBioMedicine* **2024**, *103*, 105107, doi:10.1016/j.ebiom.2024.105107.

155. Tavolinejad, H.; Erten, O.; Maynard, H.; Chirinos, J.A. Prognostic Value of Cardio-Ankle Vascular Index for Cardiovascular and Kidney Outcomes: Systematic Review and Meta-Analysis. *JACC: Advances* **2024**, *3*, doi:10.1016/J.JACADV.2024.101019;WEBSITE:WEBSITE:ACCPUBS;ISSUE:ISSUE:DOI.

156. Spronck, B.; Obeid, M.J.; Paravathaneni, M.; Gadela, N.V.; Singh, G.; Magro, C.A.; Kulkarni, V.; Kondaveety, S.; Gade, K.C.; Bhuva, R.; et al. Predictive Ability of Pressure-Corrected Arterial Stiffness Indices: Comparison of Pulse Wave Velocity, Cardio-Ankle Vascular Index (CAVI), and CAVI0. *Am. J. Hypertens.* **2022**, *35*, 272–280, doi:10.1093/AJH/HPAB168.

157. Uejima, T.; Dunstan, F.D.; Arbustini, E.; Łoboz-Grudzień, K.; Hughes, A.D.; Carerj, S.; Favalli, V.; Antonini-Canterin, F.; Vriz, O.; Vinereanu, D.; et al. Age-Specific Reference Values for Carotid Arterial Stiffness Estimated by Ultrasonic Wall Tracking. *J. Hum. Hypertens.* **2019**, *34*, 214, doi:10.1038/S41371-019-0228-5.

158. Wang, B.; Sun, A.; Li, H.; Chen, Z.; Cao, R.; Li, H.; Chu, Y.H.; Jin, N.; Wang, H. Highly Accelerated Aortic 4D Flow MRI: Implications for Pulse Wave Velocity Measurements. *Journal of Magnetic Resonance Imaging* **2026**, *63*, 549–560, doi:10.1002/JMRI.70153;SUBPAGE:STRING:FULL.

159. Omboni, S.; Arystan, A.; Benczur, B. Ambulatory Monitoring of Central Arterial Pressure, Wave Reflections, and Arterial Stiffness in Patients at Cardiovascular Risk. *Journal of Human Hypertension 2021 36:4* **2021**, *36*, 352–363, doi:10.1038/s41371-021-00606-4.

160. Millasseau, S.C.; Kelly, R.P.; Ritter, J.M.; Chowienczyk, P.J. Determination of Age-Related Increases in Large Artery Stiffness by Digital Pulse Contour Analysis. *Clin. Sci.* **2002**, *103*, 371–377, doi:10.1042/CS1030371.

161. Chiarelli, A.M.; Bianco, F.; Perpetuini, D.; -, al; Wu, M.-T.; Liu, I.-F.; Tzeng, Y.-H.; Wang, L. Modified Photoplethysmography Signal Processing and Analysis Procedure for Obtaining Reliable Stiffness Index Reflecting Arteriosclerosis Severity. *Physiol. Meas.* **2022**, *43*, 085001, doi:10.1088/1361-6579/AC7D91.

162. Salvi, P.; Magnani, E.; Valbusa, F.; Agnoletti, D.; Alecu, C.; Joly, L.; Benetos, A. Comparative Study of Methodologies for Pulse Wave Velocity Estimation. *Journal of Human Hypertension 2008 22:10* **2008**, *22*, 669–677, doi:10.1038/jhh.2008.42.

163. Yilmaz, G.; Ong, J.L.; Ling, L.H.; Chee, M.W.L. Insights into Vascular Physiology from Sleep Photoplethysmography. *Sleep* **2023**, *46*, 1–11, doi:10.1093/SLEEP/ZSAD172.

164. Chowienczyk, P.J.; Kelly, R.P.; MacCallum, H.; Millasseau, S.C.; Andersson, T.L.G.; Gosling, R.G.; Ritter, J.M.; Änggård, E.E. Photoplethysmographic Assessment of Pulse Wave Reflection: Blunted Response to Endothelium-Dependent Beta2-Adrenergic Vasodilation in Type II Diabetes Mellitus. *J. Am. Coll. Cardiol.* **1999**, *34*, 2007–2014, doi:10.1016/S0735-1097(99)00441-6.

165. Abdullah Said, M.; Eppinga, R.N.; Lipsic, E.; Verweij, N.; van der Harst, P. Relationship of Arterial Stiffness Index and Pulse Pressure With Cardiovascular Disease and Mortality. *Journal of the American Heart Association: Cardiovascular and Cerebrovascular Disease* **2018**, *7*, e007621, doi:10.1161/JAHA.117.007621.

166. Mukkamala, R.; Hahn, J.O.; Inan, O.T.; Mestha, L.K.; Kim, C.S.; Toreyin, H.; Kyal, S. Toward Ubiquitous Blood Pressure Monitoring via Pulse Transit Time: Theory and Practice. *IEEE Trans. Biomed. Eng.* **2015**, *62*, 1879–1901, doi:10.1109/TBME.2015.2441951.

167. Lee, J.; Yang, S.; Lee, S.; Kim, H.C. Analysis of Pulse Arrival Time as an Indicator of Blood Pressure in a Large Surgical Biosignal Database: Recommendations for Developing Ubiquitous Blood Pressure Monitoring Methods. *Journal of Clinical Medicine 2019, Vol. 8, Page 1773* **2019**, *8*, 1773, doi:10.3390/JCM8111773.

168. Chan, G.; Cooper, R.; Hosanee, M.; Welykholowa, K.; Kyriacou, P.A.; Zheng, D.; Allen, J.; Abbott, D.; Lovell, N.H.; Fletcher, R.; et al. Multi-Site Photoplethysmography Technology for Blood Pressure Assessment: Challenges and Recommendations. *Journal of Clinical Medicine 2019, Vol. 8, Page 1827* **2019**, *8*, 1827, doi:10.3390/JCM8111827.

169. Peltokangas, M.; Vehkaoja, A.; Huotari, M.; Verho, J.; Mattila, V.M.; Röning, J.; Romsi, P.; Lekkala, J.; Oksala, N. Combining Finger and Toe Photoplethysmograms for the Detection of Atherosclerosis. *Physiol. Meas.* **2017**, *38*, 139, doi:10.1088/1361-6579/AA4EB0.

170. Sondej, T.; Jannasz, I.; Sieczkowski, K.; Dobrowolski, A.; Obiała, K.; Targowski, T.; Olszewski, R. Validation of a New Device for Photoplethysmographic Measurement of Multi-Site Arterial Pulse Wave Velocity. *Biocybern. Biomed. Eng.* **2021**, *41*, 1664–1684, doi:10.1016/J.BBE.2021.11.001.

171. Lazim, M.R.M.L.M.; Aminuddin, A.; Chellappan, K.; Ugusman, A.; Hamid, A.A.; Ahmad, W.A.N.W.; Mohamad, M.S.F. Is Heart Rate a Confounding Factor for Photoplethysmography Markers? A Systematic Review. *International Journal of Environmental Research and Public Health 2020, Vol. 17, Page 2591* **2020**, *17*, 2591, doi:10.3390/IJERPH17072591.

172. Li, P.; Laleg-Kirati, T.M. Central Blood Pressure Estimation from Distal PPG Measurement Using Semiclassical Signal Analysis Features. *IEEE Access* **2021**, *9*, 44963–44973, doi:10.1109/ACCESS.2021.3065576.

173. Mok Ahn, J. New Aging Index Using Signal Features of Both Photoplethysmograms and Acceleration Plethysmograms. *Healthc. Inform. Res.* **2017**, *23*, 53–59, doi:10.4258/HIR.2017.23.1.53.

174. Xing, X.; Dong, W.F.; Xiao, R.; Song, M.; Jiang, C. Analysis of the Chaotic Component of Photoplethysmography and Its Association with Hemodynamic Parameters. *Entropy* **2023**, *25*, 1582, doi:10.3390/E25121582/S1.

175. Xing, X.; Hong, J.; Alastruey, J.; Long, X.; Liu, H.; Dong, W.F. Robust Arterial Compliance Estimation with Katz's Fractal Dimension of Photoplethysmography. *Front. Physiol.* **2024**, *15*, 1398904, doi:10.3389/FPHYS.2024.1398904/TEXT.

176. Hellqvist, H.; Karlsson, M.; Hoffman, J.; Kahan, T.; Spaak, J. Estimation of Aortic Stiffness by Finger Photoplethysmography Using Enhanced Pulse Wave Analysis and Machine Learning. *Front. Cardiovasc. Med.* **2024**, *11*, 1350726, doi:10.3389/FCVM.2024.1350726/TEXT.

177. Shin, H.; Noh, G.; Choi, B.M. Photoplethysmogram Based Vascular Aging Assessment Using the Deep Convolutional Neural Network. *Scientific Reports 2022 12:1* **2022**, *12*, 11377-, doi:10.1038/s41598-022-15240-4.

178. Mitchell, G.F.; Rong, J.; Larson, M.G.; Korzinski, T.J.; Xanthakis, V.; Sigurdsson, S.; Gudnason, V.; Launer, L.J.; Aspelund, T.; Hamburg, N.M.; et al. Vascular Age Assessed From an Uncalibrated, Noninvasive Pressure Waveform by Using a Deep Learning Approach: The AI-VascularAge Model. *Hypertension* **2024**, *81*, 193–201, doi:10.1161/HYPERTENSIONAHA.123.21638.

179. Castellano Ontiveros, R.; Elgendi, M.; Menon, C. A Machine Learning-Based Approach for Constructing Remote Photoplethysmogram Signals from Video Cameras. *Communications Medicine 2024 4:1* **2024**, *4*, 109-, doi:10.1038/s43856-024-00519-6.

180. Elgendi, M.; Martinelli, I.; Menon, C. Optimal Signal Quality Index for Remote Photoplethysmogram Sensing. *npj Biosensing 2024 1:1* **2024**, *1*, 5-, doi:10.1038/s44328-024-00002-1.

181. Choi, J.; Park, M.G. Variations in the Second Derivative of a Photoplethysmogram with Age in Healthy Korean Adults. *Int. J. Environ. Res. Public Health* **2023**, *20*, 236, doi:10.3390/IJERPH20010236/S1.

182. Iketani, Y.; Iketani, T.; Takazawa, K.; Murata, M. Second Derivative of Photoplethysmogram in Children and Young People. *Jpn. Circ. J.* **2000**, *64*, 110–116, doi:10.1253/JCJ.64.110.

183. Imanaga, I.; Hara, H.; Koyanagi, S.; Tanaka, K. Correlation between Wave Components of the Second Derivative of Plethysmogram and Arterial Distensibility. *Jpn. Heart J.* **1998**, *39*, 775–784, doi:10.1536/IHJ.39.775.

184. Otsuka, T.; Kawada, T.; Katsumata, M.; Ibuki, C.; Kusama, Y. Independent Determinants of Second Derivative of the Finger Photoplethysmogram among Various Cardiovascular Risk Factors in Middle-Aged Men. *Hypertension Research 2007 30:12* **2007**, *30*, 1211–1218, doi:10.1291/hypres.30.1211.

185. Hyun, J.B.; Jung, S.K.; Yun, S.K.; Haet, B.L.; Kwang, S.P. Second Derivative of Photoplethysmography for Estimating Vascular Aging. *Proceedings of the IEEE/EMBS Region 8 International Conference on Information Technology Applications in Biomedicine, ITAB* **2007**, 70–72, doi:10.1109/ITAB.2007.4407346.

186. Bortolotto, L.A.; Blacher, J.; Kondo, T.; Takazawa, K.; Safar, M.E. Assessment of Vascular Aging and Atherosclerosis in Hypertensive Subjects: Second Derivative of Photoplethysmogram versus Pulse Wave Velocity. *Am. J. Hypertens.* **2000**, *13*, 165–171, doi:10.1016/S0895-7061(99)00192-2.

187. Hashimoto, J.; Watabe, D.; Kimura, A.; Takahashi, H.; Ohkubo, T.; Totsune, K.; Imai, Y. Determinants of the Second Derivative of the Finger Photoplethysmogram and Brachial-Ankle Pulse-Wave Velocity: The Ohasama Study. *Am. J. Hypertens.* **2005**, *18*, 477–485, doi:10.1016/J.AMJHYPER.2004.11.009.

188. Elgendi, M.; Norton, I.; Brearley, M.; Abbott, D.; Schuurmans, D. Detection of a and b Waves in the Acceleration Photoplethysmogram. *BioMedical Engineering OnLine 2014 13:1* **2014**, *13*, 139-, doi:10.1186/1475-925X-13-139.

189. Dall'Olio, L.; Curti, N.; Remondini, D.; Safi Harb, Y.; Asselbergs, F.W.; Castellani, G.; Uh, H.W. Prediction of Vascular Aging Based on Smartphone Acquired PPG Signals. *Scientific Reports 2020 10:1* **2020**, *10*, 19756-, doi:10.1038/s41598-020-76816-6.

190. Mohammadi, H.; Tarvirdizadeh, B.; Alipour, K.; Ghamari, M. Cuff-Less Blood Pressure Monitoring via PPG Signals Using a Hybrid CNN-BiLSTM Deep Learning Model with Attention Mechanism. *Scientific Reports 2025 15:1* **2025**, *15*, 22229-, doi:10.1038/s41598-025-07087-2.

191. Abdelhamid, K.; Reissenberger, P.; Piper, D.; Koenig, N.; Hoelz, B.; Schlaepfer, J.; Gysler, S.; McCullough, H.; Ramin-Wright, S.; Gabathuler, A.L.; et al. Fully Automated Photoplethysmography-Based Wearable Atrial Fibrillation Screening in a Hospital Setting. *Diagnostics* **2025**, *15*, 1233, doi:10.3390/DIAGNOSTICS15101233/S1.

192. Rantula, O.A.; Lipponen, J.A.; Halonen, J.; Jäntti, H.; Rissanen, T.T.; Naukkarinen, N.S.; Väliaho, E.S.; Santala, O.E.; Sedha, J.; Martikainen, T.J.; et al.

Photoplethysmography in Recent-Onset Atrial Fibrillation: Automatic Detection of Rhythm Change and Burden. *European Heart Journal - Digital Health* **2025**, *6*, 723–732, doi:10.1093/EHJDH/ZTAF055.

193. Mohagheghian, F.; Han, D.; Ghetia, O.; Chen, D.; Peitzsch, A.; Nishita, N.; Ding, E.Y.; Mensah Otabil, E.; Noorishirazi, K.; Hamel, A.; et al. Atrial Fibrillation Detection on Reconstructed Photoplethysmography Signals Collected from a Smartwatch Using a Denoising Autoencoder. *Expert Syst. Appl.* **2024**, *237*, 121611, doi:10.1016/J.ESWA.2023.121611.
194. Ding, X.; Zhang, Y.T. Pulse Transit Time Technique for Cuffless Unobtrusive Blood Pressure Measurement: From Theory to Algorithm. *Biomed. Eng. Lett.* **2019**, *9*, 37, doi:10.1007/S13534-019-00096-X.
195. Figini, V.; Galici, S.; Russo, D.; Centonze, I.; Visintin, M.; Pagana, G. Improving Cuff-Less Continuous Blood Pressure Estimation with Linear Regression Analysis. *Electronics 2022, Vol. 11, Page 1442* **2022**, *11*, 1442, doi:10.3390/ELECTRONICS11091442.
196. Yu, S.G.; Kim, S.E.; Kim, N.H.; Suh, K.H.; Lee, E.C. Pulse Rate Variability Analysis Using Remote Photoplethysmography Signals. *Sensors 2021, Vol. 21, Page 6241* **2021**, *21*, 6241, doi:10.3390/S21186241.
197. Ding, Z.; Hu, Y.; Li, Z.; Mao, Y.; Li, H.; Zhou, D.; Chu, X.; Yu, L.; Liu, Z.; Wu, F.; et al. AI Modeling Photoplethysmography to Electrocardiography Useful for Predicting Cardiovascular Disease. *npj Digital Medicine 2025 9:1* **2025**, *9*, 61-, doi:10.1038/s41746-025-02228-3.
198. Fuadah, Y.N.; Lim, K.M. Advances in Cardiovascular Signal Analysis with Future Directions: A Review of Machine Learning and Deep Learning Models for Cardiovascular Disease Classification Based on ECG, PCG, and PPG Signals. *Biomedical Engineering Letters 2025 15:4* **2025**, *15*, 619–660, doi:10.1007/S13534-025-00473-9.
199. Elbasha, K.; Kaur, J.; Abdelghani, M.; Landt, M.; Alotaibi, S.; Abdelaziz, A.; Abdel-Wahab, M.; Toelg, R.; Geist, V.; Richardt, G.; et al. Ten-Year Durability, Hemodynamic Performance, and Clinical Outcomes after Transcatheter Aortic Valve Implantation Using a Self-Expanding Device. *Cardiology and Therapy 2024 13:3* **2024**, *13*, 529–540, doi:10.1007/S40119-024-00369-2.
200. Puleo, S.; Diana, G.; Pasta, S.; Scardulla, F.; D'Acquisto, L. Sensor-Based Bioprosthetic Valve Monitoring: Numerical Simulation and Experimental Design.

Lecture Notes in Mechanical Engineering **2025**, 44–51, doi:10.1007/978-3-031-76594-0_6/FIGURES/4.

201. Puleo, S.; Diana, G.; Livolsi, C.; Nioi, L.; Cuscino, N.; Scardulla, F.; Pasta, S.; D'Acquisto, L. Non-Invasive Monitoring of Transcatheter Heart Valve Using Photoplethysmography and Machine Learning. *Artif. Organs* **2026**, *50*, doi:10.1111/AOR.70069.
202. Fuiano, F.; Fiori, G.; Vurchio, F.; Scorza, A.; Sciuto, S.A. Transit Time Measurement of a Pressure Wave through an Elastic Tube Based on LVDT Sensors.
203. Njoum, H.; Kyriacou, P.A. In Vitro Validation of Measurement of Volume Elastic Modulus Using Photoplethysmography. *Med. Eng. Phys.* **2017**, *52*, 10, doi:10.1016/J.MEDENGPHY.2017.11.011.
204. Diana, G.; Scardulla, F.; Puleo, S.; Pasta, S.; D'Acquisto, L. Non-Invasive Estimation of Arterial Stiffness Using Photoplethysmography Sensors: An In Vitro Approach. *Sensors 2025, Vol. 25, Page 3301* **2025**, *25*, 3301, doi:10.3390/S25113301.
205. Diana, G.; Scardulla, F.; Puleo, S.; Pasta, S.; D'Acquisto, L. A Preliminary Study on Arterial Stiffness Assessment Using Photoplethysmographic Sensors. *Engineering Proceedings 2024, Vol. 82, Page 80* **2024**, *82*, 80, doi:10.3390/ECSA-11-20455.
206. Pasta, S.; Catalano, C.; Crascì, F.; Scuoppo, R. A Custom-Built Planar Biaxial System for Soft Tissue Material Testing. *HardwareX* **2023**, *16*, e00475, doi:10.1016/J.OHX.2023.E00475.
207. Fuiano, F.; Fiori, G.; Scorza, A.; Sciuto, S.A. A Novel Experimental Set-up for Young Modulus Assessment through Transit Time Measurements in Biomedical Applications. *2021 IEEE International Workshop on Metrology for Industry 4.0 and IoT, MetroInd 4.0 and IoT 2021 - Proceedings* **2021**, 117–121, doi:10.1109/METROIND4.0IOT51437.2021.9488460.
208. Hong, J.; Nandi, M.; Charlton, P.H.; Alastruey, J. Noninvasive Hemodynamic Indices of Vascular Aging: An in Silico Assessment. *Am. J. Physiol. Heart Circ. Physiol.* **2023**, *325*, H1290–H1303, doi:10.1152/AJPHEART.00454.2023.
209. Diana, G.; Scardulla, F.; Pasta, S.; Acquisto, L.D.' Analysis of the Second Derivative of the PPG Signal as Indicator of Vascular Aging. *Engineering Proceedings 2025, Vol. 118, Page 72* **2025**, *118*, 72, doi:10.3390/ECSA-12-26557.
210. YT, G.; E, Y.; WT, W.; P, K.; N, S.; AG, S.; MD, B. Vascular Aging: Implications for Cardiovascular Disease and Therapy. *Transl. Med. (Sunnyvale)* **2016**, *6*, doi:10.4172/2161-1025.1000183.

211. Ahmed, B.; Rahman, A.A.; Lee, S.; Malhotra, R. The Implications of Aging on Vascular Health. *Int. J. Mol. Sci.* **2024**, *25*, doi:10.3390/IJMS252011188.
212. Otesteanu, C.; Diana, G.; Scardulla, F.; Puleo, S.; Pasta, S.; D'Acquisto, L.; Menon, C. Machine Learning for Classifying Vascular Age Using the Second Derivative of the PPG Signal. **2025**, 1–4, doi:10.1109/CIEES66347.2025.11300216.
213. Moço, A. V.; Stuijk, S.; De Haan, G. New Insights into the Origin of Remote PPG Signals in Visible Light and Infrared. *Scientific Reports 2018 8:1* **2018**, *8*, 8501-, doi:10.1038/s41598-018-26068-2.
214. Avci, P.; Gupta, A.; Sadasivam, M.; Vecchio, D.; Pam, Z.; Pam, N.; Hamblin, M.R. Low-Level Laser (Light) Therapy (LLLT) in Skin: Stimulating, Healing, Restoring. *Semin. Cutan. Med. Surg.* **2013**, *32*, 41.
215. Al-Halawani, R.; Qassem, M.; Kyriacou, P.A. Monte Carlo Simulation of the Effect of Melanin Concentration on Light-Tissue Interactions in Transmittance and Reflectance Finger Photoplethysmography. *Sci. Rep.* **2024**, *14*, 8145, doi:10.1038/S41598-024-58435-7.
216. Maeda, Y.; Sekine, M.; Tamura, T. The Advantages of Wearable Green Reflected Photoplethysmography. *Journal of Medical Systems 2010 35:5* **2010**, *35*, 829–834, doi:10.1007/S10916-010-9506-Z.
217. Shores, J.T. Anatomy and Physiology of the Fingertip. *Fingertip Injuries: Diagnosis, Management and Reconstruction* **2015**, 1–9, doi:10.1007/978-3-319-13227-3_1/SAVE-RESEARCH.
218. Alsousou, J.; Bhalaik, V. Anatomy and Approaches of the Wrist. *Orthop. Trauma* **2025**, *39*, 248–255, doi:10.1016/J.MPORTH.2025.06.005.
219. Eschweiler, J.; Li, J.; Quack, V.; Rath, B.; Baroncini, A.; Hildebrand, F.; Migliorini, F. Anatomy, Biomechanics, and Loads of the Wrist Joint. *Life 2022, Vol. 12, Page 188* **2022**, *12*, 188, doi:10.3390/LIFE12020188.
220. Moscato, S.; Giudice, S. Lo; Massaro, G.; Chiari, L. Wrist Photoplethysmography Signal Quality Assessment for Reliable Heart Rate Estimate and Morphological Analysis. *Sensors* **2022**, *22*, 5831, doi:10.3390/S22155831/S1.
221. Šimek, J.; Wichterle, D.; Melenovský, V.; Malík, J.; Svačina, Š.; Widimský, J. Second Derivative of the Finger Arterial Pressure Waveform: An Insight into Dynamics of the Peripheral Arterial Pressure Pulse. *Physiol. Res.* **2005**, *54*, 505–513, doi:10.33549/PHYSIOLRES.930683.

222. Elgendi, M. Detection of c, d, and e Waves in the Acceleration Photoplethysmogram. *Comput. Methods Programs Biomed.* **2014**, *117*, 125–136, doi:10.1016/J.CMPB.2014.08.001.

223. Solé Morillo, Á.; Lambert Cause, J.; Baciu, V.E.; da Silva, B.; Garcia-Naranjo, J.C.; Stiens, J. PPG EduKit: An Adjustable Photoplethysmography Evaluation System for Educational Activities. *Sensors 2022, Vol. 22, Page 1389* **2022**, *22*, 1389, doi:10.3390/S22041389.

224. Cri¸san, C.; Nechita, E.; Pavaloaia, V.-D.; Zou, Y.; Kapogianni, N.-A.; Sideraki, A.; Anagnostopoulos, C.-N. Using Smartwatches in Stress Management, Mental Health, and Well-Being: A Systematic Review. *Algorithms 2025, Vol. 18, Page 419* **2025**, *18*, 419, doi:10.3390/A18070419.

225. Liang, Y.; Chen, Z.; Liu, G.; Elgendi, M. A New, Short-Recorded Photoplethysmogram Dataset for Blood Pressure Monitoring in China. *Sci. Data* **2018**, *5*, 180020-, doi:10.1038/SDATA.2018.20;SUBJMETA.

226. Liang, Y.; Chen, Z.; Ward, R.; Elgendi, M. Hypertension Assessment Using Photoplethysmography: A Risk Stratification Approach. *Journal of Clinical Medicine 2019, Vol. 8, Page 12* **2018**, *8*, 12, doi:10.3390/JCM8010012.

227. Yao, L.P.; Liu, W.Z. Hypertension Assessment Based on Feature Extraction Using a Photoplethysmography Signal and Its Derivatives. *Physiol. Meas.* **2021**, *42*, 065001, doi:10.1088/1361-6579/ABA537.

228. Otsuka, T.; Nishiyama, Y.; Kato, K.; Kodani, E.; Kawada, T. Second Derivative of the Finger Photoplethysmogram Predicts the Risk of Developing Hypertension in Middle-Aged Men. *J. Atheroscler. Thromb.* **2025**, *32*, 188–197, doi:10.5551/JAT.65123.